Vol. 6 No. II Tahun 2023

P-ISSN : 2621-0215
E-ISSN : 2621-489X

Al-Fiziya

Journal of Materials Science, Geophysics, Instrumentation and Theoretical Physics

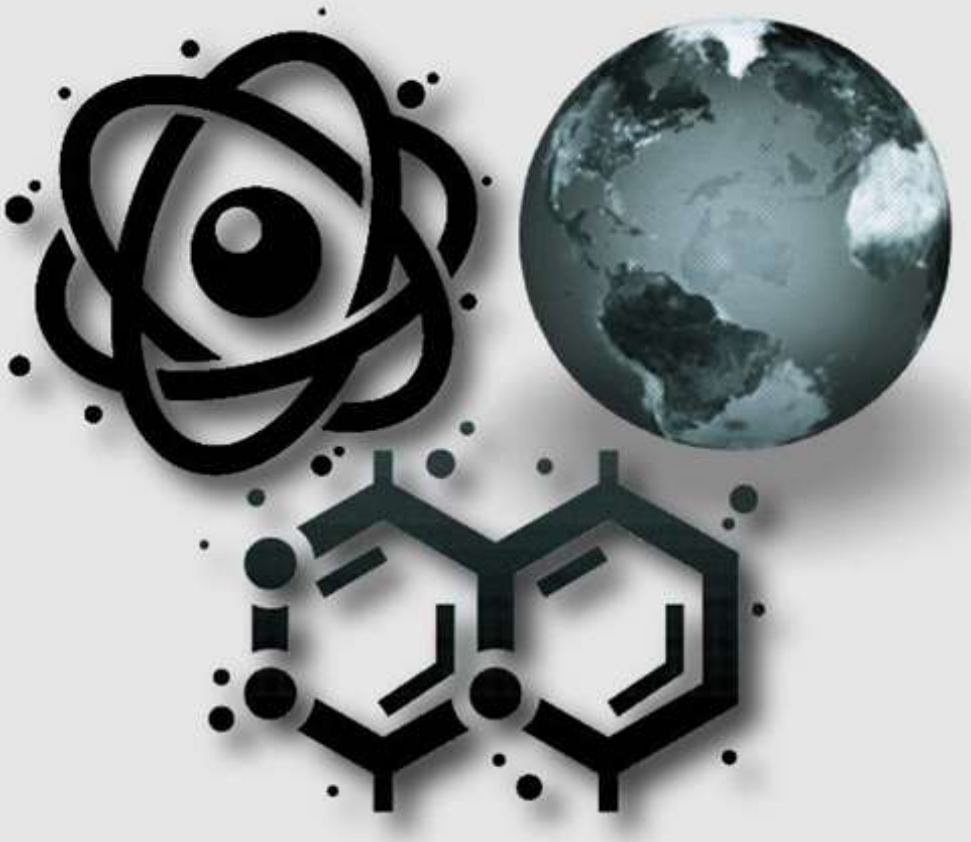

Published by
Program Studi Fisika
Fakultas Sains dan Teknologi
Universitas Islam Negeri Syarif Hidayatullah Jakarta

AL-FIZIYA:
Journal of Materials Science, Geophysics, Instrumentation, and Theoretical Physics

Vol. 6, No. II, Tahun 2023

Alamat Redaksi
Gedung Fakultas Sains dan Teknologi Lt. 3
Jl. Ir. H Juanda No.95 Ciputat 15412 Tangerang
Telp. (6221)743731, (6221)7493315
Email: al-fiziya@uinjkt.ac.id

Published by
Program Studi Fisika, Fakultas Sains dan Teknologi
Universitas Islam Negeri Syarif Hidayatullah Jakarta

PENGANTAR REDAKSI

Assalamu'alaikum, Wr. Wb.

Puji Syukur kita panjatkan kehadirat Allah SWT, dengan terbitnya Al-Fiziya: Journal of Materials Science, Geophysics, Instrumentation, and Theoretical Physics Vol 6, No. II, Tahun 2023 dengan nomor ISSN: 2621-0215 dan E-ISSN: 2621-489X sebagai jurnal penelitian dan pengembangan ilmu fisika yang diterbitkan oleh Program Studi Fisika Fakultas Sains dan Teknologi UIN Syarif Hidayatullah Jakarta. Jurnal ini menyajikan artikel-artikel penelitian dan pengembangan terkini baik dalam Bahasa Indonesia maupun Bahasa Inggris di bidang fisika murni dan terapan, antara lain bidang fisika material, geofisika, fisika instrumentasi, dan fisika teori. Jurnal ini merupakan sarana publikasi bagi dosen dan para peneliti yang bergerak di bidang penelitian dan pengembangan ilmu fisika. Dengan demikian, melalui penerbitan jurnal ini kami memberikan kesempatan seluas-luasnya bagi siapapun yang ingi berpartisipasi dalam menyampaikan buah pikirannya melalui tulisan atau artikel yang akan kami muat pada edisi berikutnya.

Artikel yang masuk akan melalui proses seleksi oleh dewan editor dan *review* yang melibatkan mitra bestari baik dari para dosen ahli dibidangnya berdasarkan kesesuaian isi dan bobot karya ilmiah. Untuk informasi lengkap submit dan tata cara penulisan dalam Al-Fiziya: *Journal of Material Science, Geophysics, Instrumentation, and heoretical Physics* dapat dilihat pada pedoman penulisan artikel di halaman akhir penerbitan atau dapat mengakses website kami di http://journal.uinjkt.ac.id/index.php/al-fiziya. Atas nama dewan redaksi, kami mengucapkan terimakasih atas dukungan dan partisipasi dari semua pihak hingga terbitnya Al-Fiziya: *Journal of Materials Science, Geophysics, Instrumentation, and Theoretical Physics.*

Editorial in chief
SITTI AHMIATRI SAPTARI

Daftar Isi

Vol. 6, No. II Tahun 2023

Available online at:
Al-Fiziya: Journal of Materials Science, Geophysics, Instrumentation and Theoretical Physics
Website: http://journal.uinjkt.ac.id/index.php/al-fiziya
Vol.6 No. II 2023, 1-13

Ammonia (NH3) Gas Control System in Chicken Coops Using Fuzzy Logic Based Internet of Things (IoT) Method

Khasbianta Supriadi[1], Ambran Hartono[2,*], Salsabila Tahta Hirani Putri[3], Hanif Fakhrurraja[4]

[1,2]Physics Study Program, Faculty of Sciences and Technology, State Islamic University Syarif Hidayatullah Jakarta, Indonesia.
[3]Department of Information System, Faculty of Science and Technology UIN Syarif Hidayatullah Jakarta, Indonesia
[4]Research Center for Smart Mechatronics National Research and Innovation Agency of Indonesia Bandung, Indonesia

[*]ambran.hartono@uinjkt.ac.id

Submitted: ... ; Revised: ... ; Approved: .... ; Available Online:

Abstract. Chicken productivity increases every year, resulting in air pollution in the form of NH3 generated by chicken waste, which is felt by the residents living around the chicken coop. The purpose of this research is to design an ammonia gas control system using Matlab, with the ammonia gas sensor MQ-135 and the humidity sensor DHT11 as parameters, to minimize the ammonia gas levels. This system operates by transmitting information about the condition of ammonia gas levels using a fuzzy logic control system as the technical decision-making mechanism for driving the exhaust fan based on data from the DHT11 and MQ-135 sensors. In this research, the fuzzy logic method was employed to determine the membership functions for the DHT11 sensor (dry, moist, wet) and MQ-135 sensor (normal, moderate, high), resulting in decisions of safe, moderate, and dangerous levels. The data is monitored on a platform through the Blynk app and Thingspeak, thus connecting the Internet of Things (IoT) to the internet network using the NodeMCU ESP8266 as the microcontroller. This research yields an ammonia gas control system that effectively manages air quality affected by chicken waste, with sensor accuracy levels exceeding 97%.

Keywords: *Control System, Fuzzy Logic, Internet of Things (IoT), Thingspeak, Blynk*.
DOI : 10.15408/fiziya.v6i2.34757

INTRODUCTION

In the context of food availability, livestock products play a crucial role as one of the sub-sectors of agriculture that significantly contribute to meeting food needs. Animal products, in particular, serve as the primary source of human nutrition and animal protein [1, 2, 3, and 4]. According to data from the Ministry of Agriculture of the Republic of Indonesia in 2020, the population of meat-type chickens reached an impressive figure of 2,970,494,000 individuals, with meat production totaling 3,275,326,000 tons [5].

The population size and production of broiler chickens must be balanced with an increase in farmer awareness to maintain cleanliness in the poultry houses and the farm environment to prevent pollution from chicken waste [6, 7, 8, 9, and 10]. Government Regulation of the Republic of Indonesia No. 28 of 2004 on the safety, quality, and nutrition of food reflects the importance of maintaining cleanliness in poultry houses as a step to reduce chicken waste pollution. Pollution is often caused by a lack of awareness among farmers in maintaining cleanliness and the environment within the poultry houses [11, 12, 13, 14, and 15]. Accumulated chicken waste leads to an increase in daily waste production, which, when multiplied by the chicken population, can significantly elevate the levels of chicken waste pollution. This results in the release of harmful gases such as ammonia and methane. Complaints from the surrounding community about the odor from the poultry houses are also a negative consequence of improper poultry house management [16, 17, 18, 19, and 20], which occurs due to sudden changes in feed that make the poultry house wet and emit a strong odor.

The primary sources of ammonia gas (NH3) include the chemical industry, oil refineries, coal furnaces, livestock barns, and fuel combustion [21, 22, 23, 24, and 25]. Ammonia in the atmosphere originates from various sources, including the decomposition of waste, fertilizer manufacturing industries, and fertilizer usage. From these sources, ammonia is founds in the air, soil, and water. Ammonia exists as a gas near industrial waste sites, in water solution in ponds or bodies of water near waste sites, and can also be found adhered to soil particles in waste disposal areas [26, 27, 28, 29, 30, and 31].

Ammonia (NH3) is a colour less gas with a boiling point of -33°C. Ammonia gas is lighter than air, with a density of approximately 0.6 times that of air at the same temperature. The sharp od or of ammonia can be detected at low concentrations of 1-5 ppm [32, 33, 34, 35, 36, 37, 38, 39, and 40]. One of the health impacts of high ammonia levels, above 50 ppm, is irritation of the eyes and nose, throat irritation, coughing, chest pain, and even shortness of breath [26].

Factors contributing to the presence of this chemical compound include the accumulation of chicken waste, temperature, and room humidity. Temperature and room conditions can influence the concentration of the formation of harmful gases that occur during the decomposition of chicken waste. This can result in health problems such as reduced appetite in animals, decreased chicken productivity, and respiratory disturbances in people near chicken coops [41, 42, 43, 44, 45, 46, and 47]. Inhaling ammonia gas can cause respiratory problems, irritation of the eyes, nose, and throat, and in severe cases, when it reaches a concentration measured in PPM (Parts Per Million), it can lead to death.

Farmers have been making significant efforts to reduce the pollution levels in chicken coops. These efforts encompass regular cleaning of the chicken coops, providing natural feed additives such as palm fruit for enhanced chicken performance [39, 41, and 43], converting waste into fertilizer, and attempting to control ammonia gas levels in chickens through the use of probiotics, prebiotics, pesticides, and basil flour [48, 49, and 50]. However, challenges arise due to the rapid formation of decomposed gases and the absence of effective tools to mitigate ammonia (NH_3) gas levels in the coops.

For this reason, the author proposes an integrated system in detecting the presence of ammonia gas. The writing team designed a good detection system that can monitor and control the gas to ensure the cage environment is maintained properly and

Vol.6 No. II 2023, 1-13
P-ISSN: 2621-0215, E-ISSN: 2621-489X

safely. In this article, we will describe the ammonia gas control system. In its application, using an IoT-based approach ESP8266 integrated with fuzzy logic [51, 52, and 53]. This aspect is the novelty of this study.

The development of an NH_3 gas control system in chicken coops, utilizing the ESP8266-based IoT approach and incorporating fuzzy logic, offers an effective solution to prevent the formation of ammonia gas and maintain its levels. This system provides farmers with convenient access and control, enabling them to monitor temperature, humidity, and gas levels within the chicken coop, thanks to its integration with the Internet of Things (IoT).

METHODOLOGY

The research was conducted from August 21, 2021, to September 21, 2022, at the researcher's residence in Bekasi and at the Instrumentation Development Center of the Indonesian Research and Innovation Agency (BRIN), LIPI Complex Building 80, Sangkuriang Street, Bandung.

Hardware Design

The block diagram of this equipment system is as follows in **Figure 1** below:

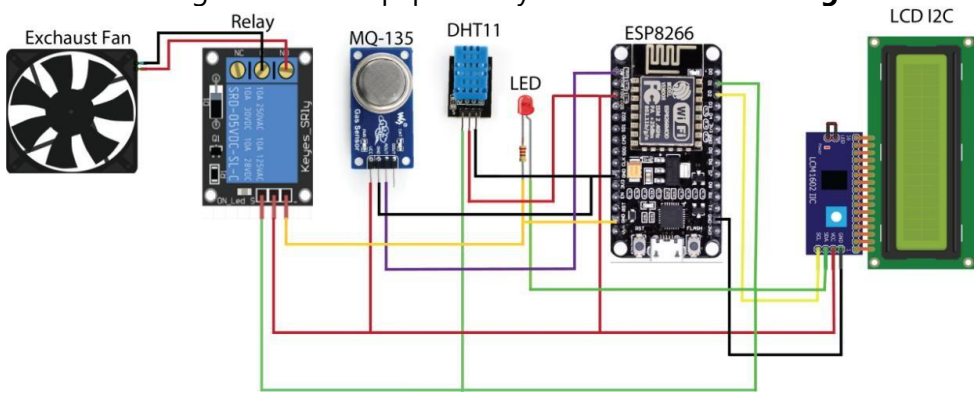

Figure. 1 The block diagram of the hardware design system

1. The explanation of the components contained in **Figure. 1**, including:
2. MQ-135 sensor is used to detect and measure the concentration of ammonia gas.
3. DHT11 sensor is used to detect the temperature and humidity of the environment.
4. Single relay module is used to control and supply electrical power.
5. LED indicators are used in the form of green and red lights.
6. Exhaust fan is used to circulate the ambient air.
7. ESP8266 is used to process and transmit data and connect to the internet.
8. LCD 16×2 is used to display the PPM value and temperature (in ºC) and humidity.

Vol.6 No. II 2023, 1-13
P-ISSN: 2621-0215, E-ISSN: 2621-489X

Fuzzy Logic Design

In this study, the Sugeno fuzzy logic method is employed on a microcontroller that has acquired data from both sensors, namely MQ-135 and DHT11. Fuzzy logic is an approach for making decisions using calculations with linguistic variable outputs. The Sugeno method is a fuzzy inference method for rules represented in the form of IF-THEN, where the output of this fuzzy logic is not in the form of sets but in the form of constants.

The following are the stages of fuzzy logic design as shown in **Figure 2**

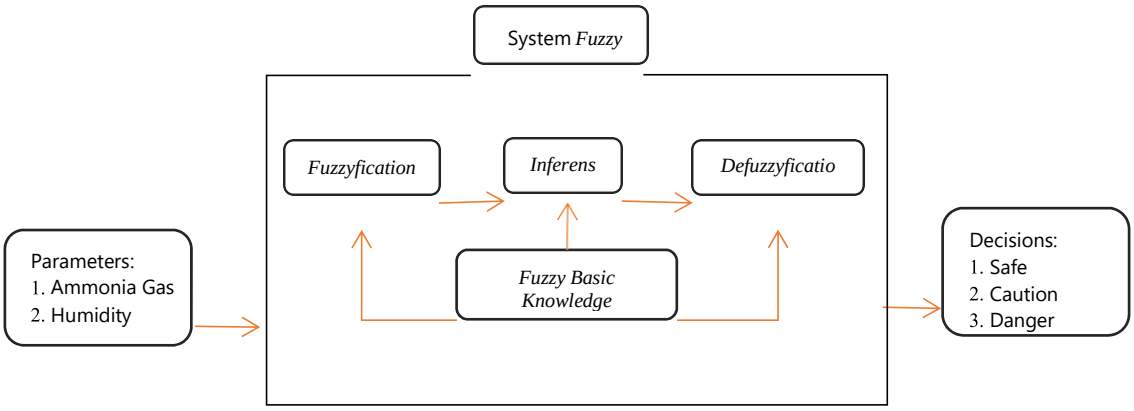

Figure. 2 Stages of Fuzzy Logic Design

Stage Design System

The following is a flow diagram of the ammonia gas detection system as shown in **Figure. 3.**

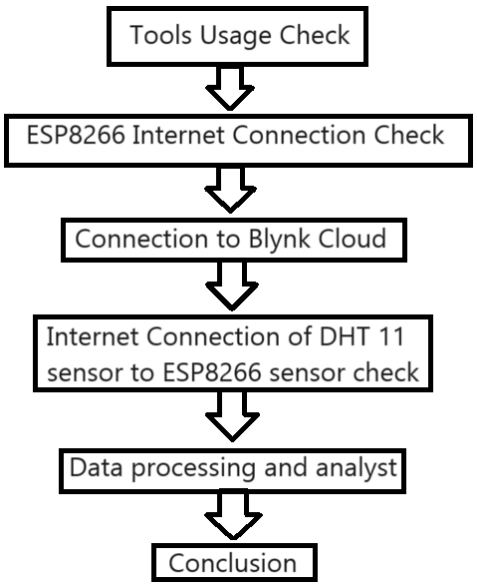

Figure. 3 Stage of the ammonia gas detection system

Vol.6 No. II 2023, 1-13
P-ISSN: 2621-0215, E-ISSN: 2621-489X

RESULTS AND DISCUSSIONS

A device with an ammonia gas control system using fuzzy logic has been successfully created. This system can provide Safe, Caution, and Danger decisions regarding ammonia gas levels in chicken coops using two sensors: the MQ-135 sensor and the DHT11 sensor.

The readings from both sensors will be transmitted via ThingSpeak with the internet serving as the data transmission medium. Subsequently, the data stored in ThingSpeak will be sent to the Blynk App to display the sensor values, decisions, suggestions, and recommendations for minimizing ammonia gas levels in the chicken coop based on the readings from both sensors. The exhaust fan and the red LED will turn "ON" if the fuzzy logic decision is Danger, and the red LED will turn "ON" if the fuzzy logic decision is Caution.

The overall view of the built device as shown in **Figure 4**.

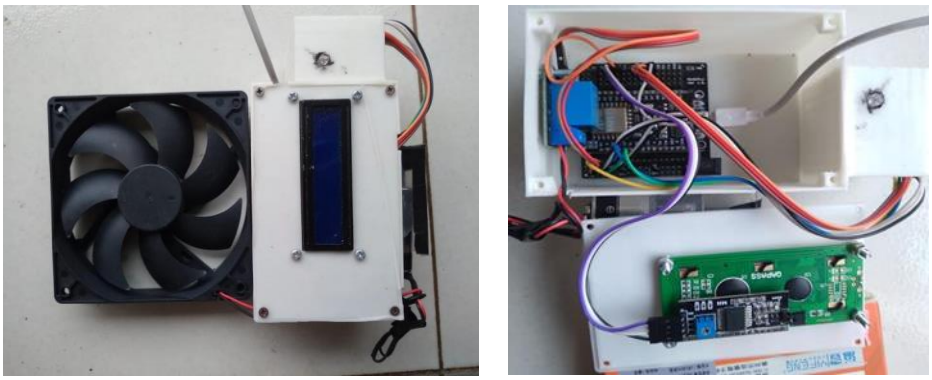

(a) (b)

Figure. 4 (a) Exterior view (b) Interior view of device sensor built

Matlab is instrumental in simulating fuzzy logic methods using the Fuzzy Logic Design tool. The simulation involves inputting linguistic variable parameters and membership functions. With two inputs, ammonia gas and humidity, and an output decision based on these inputs, the process involves substituting the two inputs. The inference step contains rules to generate the output decision from the input, with the decisions {Safe, Caution, Danger} represented in binary values as Safe (0), Caution (0.5), and Danger (1).

The results of these fuzzy rules are implemented in the form of a rule viewer. As an example, by inputting an ammonia gas level of 72.3 PPM and humidity of 71.4%, following the fuzzy rules where an ammonia gas level above 50 PPM falls into the high ammonia linguistic value range in the membership function and humidity above 65% falls into the high humidity linguistic value range in the membership function, the defuzzified result is 1 (Danger).

Testing the Accuracy of the MQ-135 Sensor

The MQ-135 sensor undergoes testing by reading varying levels of ammonia gas concentration using 25% ammonia. The sensor is placed at different distances from the MQ-135 sensor, and calculations are performed to obtain the PPM (Parts Per Million) value for 25% ammonia.

Testing the Temperature Sensor DHT11

The DHT11 sensor's temperature reading is tested by exposing it to flame or a candle with temperatures ranging from 80°C to 90°C, at varying distances. **Table 1** shown the accuracy of temperature readings from the DHT11 sensor using an HTC 1 Hygrometer.

Tabel 1 Data of testing accuracy and Accuracy rate of sensor DHT11

No.	Spacing	DHT11 (%)	Hygrometer HTC 1 (%)	Error Percentage (%)
1.	5 cm	45	46	2.22
2.	10 cm	47	48	2.13
3.	15 cm	50	52	4.00
4.	20 cm	51	52	1.96
5.	25 cm	52	53	1.92
Deviation Standard		**2.92**	**3.03**	0.88
Mean Absolute Percentage Error (MAPE)				2.45
Accuracy rate (100% - MAPE)				97.55

Analysis and Performance Testing Results in Fuzzy Logic Method

The testing that has been conducted yielded results from the designed device, and the data transmitted via NodeMCU8266 was successfully received by ThingSpeak and the Blynk App. Data displayed on the Blynk App was recorded at intervals of every 4 seconds during three different times of the day: morning, noon, and evening.

Sampling data to measure ammonia gas levels in the chicken coop is conducted at various times: morning, noon, afternoon, and evening as shown as **Table 2** to **Table 5**. Data sent to the ThingSpeak cloud is recorded every 15 seconds, and the average is calculated for each time based on the incoming data. The following are the hourly averages and the resulting graphs from various data collection times as shown as **Figure 5** to **Figure 8.**

The results of the morning analysis at the Chicken Livestock Coop in Sukaraya, Cikarang, Bekasi Regency are as shown in Table 2 follows:

Table 2 **The average hourly data for the morning hours (from 04:00 to 09:00)**

Average Hour of	Temperature (°C)	Humidity (%)	NH_3 (PPM)
1	31.41	70.9	4.45
2	30.92	73.18	1.23
3	33.43	62.77	1.59
4	32.92	58.8	2.46
5	33.55	66	4.37
6	34.62	61.17	4.34

The results of the afternoon analysis at the Chicken Livestock Coop in Sukaraya, Cikarang, Bekasi Regency are as shown Table 3 follows:

Table 3 **The average hourly data for the noon hours (from 09:00 to 14:00)**

Average Hour of	Temperature (°C)	Humidity (%)	NH_3 (PPM)
1	33.22	60.5	2.5
2	33	56.67	2.22
3	33.4	55.8	2.77
4	34.97	49	2.4
5	35.88	49.31	4.38
6	35.59	48.67	4.16

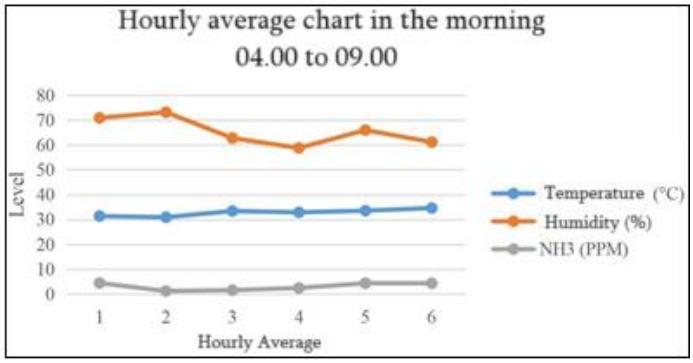

Figure. 5 Average Hourly Chart in the Morning (from 04:00 to 09:00)

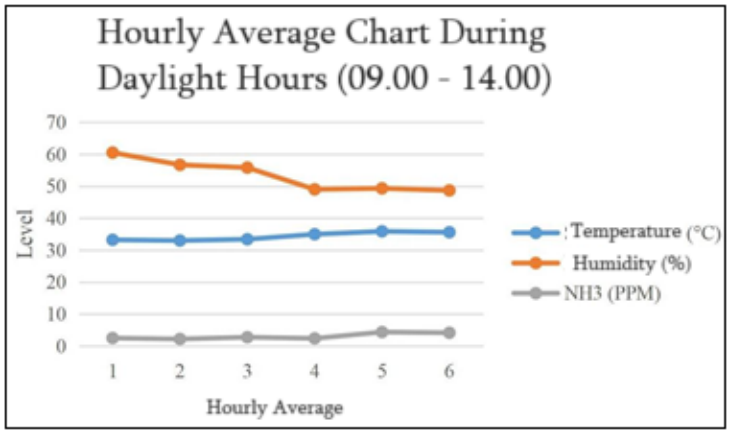

Figure. 6 Average Hourly Chart in the Noon (From 09.00 – 14.00)

Vol.6 No. II 2023, 1-13
P-ISSN: 2621-0215, E-ISSN: 2621-489X

The results of the afternoon analysis at the Chicken Livestock Coop in Sukaraya, Cikarang, Bekasi Regency are as shown Table 4 follows:

Table 4 The average hourly data for the afternoon hours (from 14:00 to 19:00)

Average Hour of	Temperature (°C)	Humidity (%)	NH_3 (PPM)
1	32.94	54.2	2.48
2	33.55	51.5	3.89
3	32.65	57.5	4.51
4	32.46	62	4.96
5	33.03	64.75	3.77
6	33.2	6433	4.68

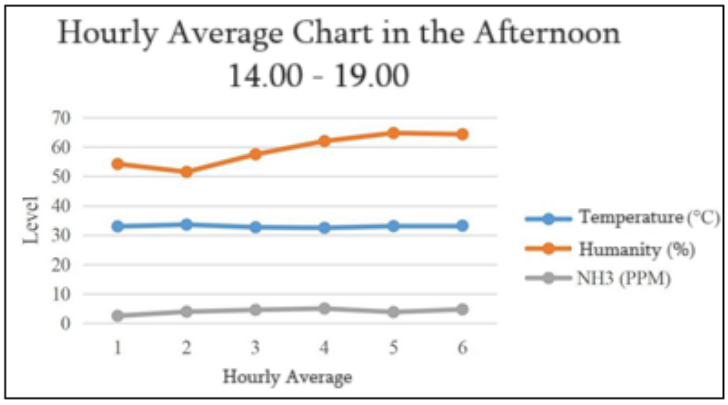

Figure. 7 Average Hourly Chart in the Afternoon (From 09.00 – 14.00)

The results of the evening analysis at the Chicken Livestock Coop in Sukaraya, Cikarang, Bekasi Regency are as shown as Table 5 follows:

Table 5 The average hourly data for the afternoon hours (from 19:00 to 04:00)

Average Hour of	Temperature (°C)	Humidity (%)	NH_3 (PPM)
1	33.72	62.67	4.73
2	34.6	62	4.76
3	34.58	62.6	4.8
4	34.42	62	4.76
5	34,17	60.22	4.17
6	34.2	60.8	4.26

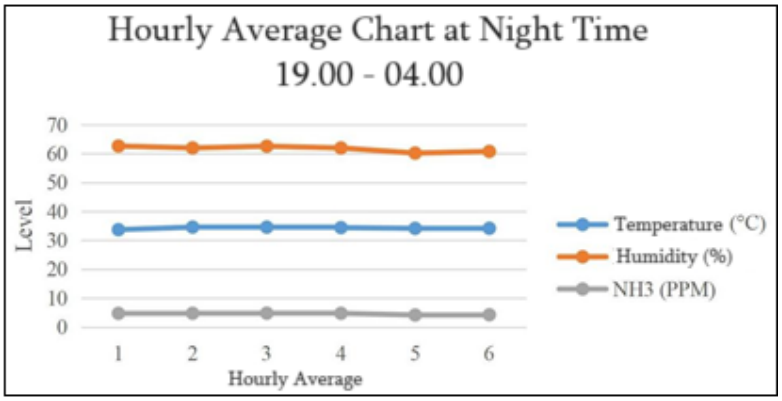

Figure. 8 Average Hourly Chart in the Afternoon (From 09.00 – 14.00)

Based on the data collected at the four different times throughout the 24 hours, it can be analyzed that each time has varying characteristics in temperature, humidity, and NH3 levels. However, the parameter levels remain within the acceptable range.

CONCLUSIONS

The conclusion of this research is that a successfully integrated control system has been developed, incorporating Internet of Things technology. Furthermore, the system effectively displays data on the Blynk app and provides decision status on the LCD screen. The Fuzzy Logic method is capable of making decisions based on data from both sensors. In cases where the ammonia gas level exceeds 50 ppm, the Fuzzy Logic system triggers alerts on the ammonia gas control system's LCD screen, activates a red warning LED, and turns on the exhaust fan to control ammonia gas levels. Based on data collected from the chicken coop at various times throughout the day, including morning, noon, and evening, efforts have been made to minimize ammonia gas levels. This research represents a significant advancement in the management and control of ammonia gas levels in poultry farms, demonstrating the potential for real-time monitoring and intervention through the integration of IoT technology and Fuzzy Logic methodology.

REFERENCES

[1] Li Day, Julie A. Cakebread, Simon M. Loveday, *Food proteins from animals and plants: Differences in the nutritional and functional properties,* Trends in Food Science & Technology Vol. 119, pp. 428-442, 2022.

[2] A.C. Alves et al., Mixing animal and plant proteins: Is this a way to improve protein techno-functionalities?, Food Hydrocolloids Vol. 97, 105171, December 2019.

[3] J.A. Cakebread et al., *Supplementation with Bovine milk or soy beverages recovers bone mineralisation in young growing rats fed an insufficient diet, in contrast to an almond beverage*, Curr Dev Nutr. Vol. 3, nzz115, Nov. 2019.

[4] C.-C. Chuang et al. *Hemp globulin heat aggregation is inhibited by the chaperone-like action of caseins*, Food Hydrocolloids, Vol. 93, pp. 46-55, 2019.

[5] A. Ramdhany and L. Ermansyah, *Statistik Peternak dan Kesehatan Hewan*, Jakarta: Direktorat Jenderal Peternakan dan Kesehatan Hewan Kementreian Pertanian RI, 2020.

[6] Luca Ferrari, Stefan-Alexandru Panaite, *Antonella Bertazzo and Francesco Visioli , Animal- and Plant-Based Protein Sources*: A Scoping Review of Human Health Outcomes and Environmental Impact, Nutrients, Vol. 14, 5115, 2022.

[7] M. K. Umam, H. S. Prayogi, and A. Nurgiartiningsih, *Penampilan Produksi Ayam Pedaging yang dipelihara pada Sistem kandang Lantai Kandang Panggung dan Kandang Bertingkat,* J. Ilmu-ilmu Peternak, Vol. 24, No. 3, pp. 79-87, 2015.

[8] Willett, W.; Rockström, J.; Loken, B.; Springmann, M.; Lang, T.; Vermeulen, S.; Garnett, T.; Tilman, D.; DeClerck, F.; Wood, A.; et al. *Food in the Anthropocene: The EAT–Lancet Commission on Healthy Diets from Sustainable Food Systems*, Lancet, Vol. 393, pp. 447–492, 2019.

[9] Adhikari, S.; Schop, M.; de Boer, I.J.M.; Huppertz, T., *Protein Quality in Perspective: A Review of Protein Quality Metrics and Their Applications*, Nutrients, Vol. 14, pp. 947, 2022.

[10] Goran Gržinić et al., *Intensive poultry farming: A review of the impact on the environment and human health,* Science of The Total Environment, Vol. 858, Part 3, No. 160014, February 2023

[11] B. P. H. N. (BPHN), *Tentang Keamanan, Gizi dan Mutu,* Indonesia 2004.

[12] M.E. Abd El-Hack, M.T. El-Saadony, A.M. Shehata, M. Arif, V.K. Paswan, G.E.-S. Batiha, A.F. Khafaga, A.R. Elbestawy, *Approaches to prevent and control Campylobacter spp. colonization in broiler chickens: a review,* Environ. Sci. Pollut. Res., Vol. 28, pp. 4989-5004, 2021.

[13] A.O. Adekiya et al., *Different organic manure sources and NPK fertilizer on soil chemical properties, growth, yield and quality of okra,* Sci. Rep., Vol. 10, 2020.

[14] K. Anderson, P.A. Moore, J. Martin, A.J. Ashworth, *Evaluation of a novel poultry litter amendment on greenhouse gas emissions*, Atmosphere, Vol. 12, p. 563, 2021.

[15] Ashraf, G. Liu, B. Yousaf, M. Arif, R. Ahmed, S. Irshad, A.I. Cheema, A. Rashid, H. Gu lzaman, *Recent trends in advanced oxidation process-based degradation of erythromycin: pollution status, eco-toxicity and degradation mechanism in aquatic cosystems*, Sci. Total Environ, Vol. 772, No. 145389, 2021.

[16] J. Astill, R.A. Dara, E.D.G. Fraser, B. Roberts, S. Sharif, *Smart poultry management: smart sensors, big data, and the internet of things*, Comput. Electron. Agric., Vol. 170, No. 105291, 2020.

[17] C.G. Awuchi, et al., *Mycotoxins' toxicological mechanisms involving humans, livestock and their associated health concerns*: a review Toxins, 14, No. 10.3390, pp. 167, 2022.

[18] J. Baker, W.H. Battye, W. Robarge, S. Pal Arya, V.P. Aneja, *Modeling and measurements of ammonia from poultry operations: their emissions, transport, and deposition in the Chesapeake Bay,* Sci. Total Environ., Vol. 706, No. 135290, 2020.

[19] O. Bamidele, et al., *Antimicrobial usage in smallholder poultry production in Nigeria*, Vet. Med. Int., p. 7746144, 2022.

[20] L. Baskin-Graves, et al., *Rapid health impact assessment of a proposed poultry processing plant in Millsboro, Delaware,* Int. J. Environ. Res. Public Health, Vol. 16, no. 10.3390, p. 3429, 2019.

[21] B. Chandra, *No. Title Pengantar Kesehatan Lingkungan*, Jakarta: EGC, 2004.
[22] Ghavam, S.; Vahdati, M.; Wilson, IG; Styring, P., *Proses Produksi Amonia Berkelanjutan*. Depan. Res Energi. Vol. 9, No. 580808, 2021.
[23] Kojima, Y. *Sifat Fisika dan Kimia Amoniak sebagai Pembawa Energi dan Hidrogen. Dalam Amonia Bebas CO_2 sebagai Pembawa Energi: Wawasan Jepang* ; Springer: Berlin/Heidelberg, Jerman, hlm. 17-28, 2022.
[24] Smith, C.; Bukit, AK; Torrente-Murciano, L. *Peran Amonia Haber-Bosch Saat Ini dan Masa Depan dalam Lanskap Energi Bebas Karbon*. Lingkungan Energi. Sains. Vol. 13, pp. 331-344, 2020.
[25] Liu, B.; Manavi, N.; Deng, H.; Huang, C.; Shan, N.; Chikan, V.; Pfromm, P. *Aktivasi N_2 pada Cluster Ni_3 dan Fe_3 yang Didukung Mangan Nitrida dan Relevansinya dengan Pembentukan Amonia*. J.Fisika. kimia. Biarkan. Vol. *12* , pp. 6535–6542, 2021.
[26] N. Roney and L. Fernando, *Toxicological Profile For Ammonia*. Atlanta: Agency for Toxic Substances and Disease Registry, 2004.
[27] Ben Hassen, T.; El Bilali, H. *Dampak Perang Rusia-Ukraina terhadap Ketahanan Pangan Global: Menuju Sistem Pangan yang Lebih Berkelanjutan dan Berketahanan?* Makanan, Vol. 11, No. 2301, 2022.
[28] Abdullah Emre Yüzbaşıoglu , Cemre Avsar , Ahmet Ozan Gezerman, *Current Research in Green and Sustainable Chemistry The current situation in the use of ammonia as a sustainable energy source and its industrial potential Current Research in Green and Sustainable*, Chemistry, Vol. 5, No. 100307, 2022.
[29] J.A. Faria, *Renaissance of ammonia synthesis for sustainable production of energy and fertilizers, Curr. Opin. Green Sustain*. Chem. Vol. 29, No. 100466, 2021.
[30] D.R. MacFarlane, P.V. Cherepanov, J. Choi, B.H.R. Suryanto, R.Y. Hodgetts, J.M. Bakker, F.M. Ferrero Vallana, A.N. Simonov, *A roadmap to the ammonia economy*, Joule, Vol. 4, pp. 1186–1205, 2020.
[31] J. Humphreys, R. Lan, S. Tao, S. *Development and recent progress on ammonia synthesis catalysts for Haber-Bosch process*, Adv. Energy Sustain. Res. Vol. 2, No. 2000043, 2020.
[32] G. Qing, R. Ghazfar, S.T. Jackowski, F. Habibzadeh, M.M. Ashtiani, C.P. Chen, M.R. Smith, T.W. Hamann, *Recent advances and challanges of electrocatalytic N2 reduction to ammonia*, Chem. Rev. Vol. 120, No. 9b00659 , 2020.
[33] K. Brigden and R. Stringer, "*Ammonia and Urea Production : Incidents of Ammonia Release From The Profertil Urea and Ammonia Facility*," *GreenPeace*. Greenpeace Research Laboratories, Department of Biological Sciences, Exeter, UK, 2000.
[34] G.F. Han, F. Li, Z.W. Chen, C. Coppex, S.J. Kim, H.J. Noh, Z. Fu, Y. Lu, C.V. Singh, S. Siahrostami, Q. Jiang, J.B. Baek, *Mechanochemistry for ammonia synthesis under mild conditions*, Nat. Nanotechnol. Vol. 16, No. 325–330, 2021.
[35] P. Bodhankar, S. Patnaik, G.R. Kale, *Thermodynamic analysis of autothermal steamreforming of methane for ammonia production*, Int. J. Energy Res. Vol. 45, pp. 6943–6957, 2020.
[36] H. Zhang, L. Wang, J. Van Herle, F. Marechal, U. Desideri, *Techno-economic comparison of green ammonia production processes*, Appl. Energy, Vol. 259,

No. 114135, 2020.

[37] Valera-Medina, F et al., *Review on ammonia as a potential fuel: from synthesis to economics*, Energy Fuel, Vol. 35, PP. 6964–7029, 2021.

[38] D. Schonvogel, J. Büsselmann, H. Schmies, H. Langnickel, P. Wagner, A. Dyck, *High temperature polymer electrolyte membrane fuel cell degradation provoked by ammonia as ambient air contaminant*, J. Power Sources, Vol. 502, No. 229993, 2021.

[39] J. Zheng, L. Jiang, Y. Lyu, S.P. Jian, S. Wang, *Green synthesis of nitrogen-toammonia fixation: past, present, and future, Energy & Environ.* Mater. Pp. 1-6, 2021.

[40] M. Wang, M.A. Khan, I. Mohsin, J. Wicks, A.H. Ip, K.Z. Sumon, C.-T. Dinh, E.H. Sargent, I.D. Gates, M.G. Kibria, *Can sustainable ammonia synthesis pathways compete with fossil-fuel based Haber- Bosch processes?* Energy Environ. Sci. Vol. 14, pp. 2535–2548, 2021.

[41] O. Sumarna, *Kimia fisika 1 Modul: Sifat-sifat Gas*. Jakarta: Universitas Terbuka Press, 2009.

[42] N. Ulupi and S. K. Inayah, "Performa Ayam Broiler dengan Pemberian Serbuk Pinang sebagai Feed Aditive," *J. Ilmu Produksi dan Teknol. Has. Peternak.*, vol. 3, no. 1, pp. 8–11, 2015.

[43] Bray, C.D., et al., *Global emissions of NH3, NOx, and N2O from biomass burning and the impact of climate change*. J. Air Waste Manag. Assoc. Vol. 71 No. 1, pp. 102–114, 2021.

[44] Domingo, N.G.G.,et al., *Air quality-related health damages of food*. Proc. Natl. Acad. Sci. U. S. A, Vol. 118, No.20, 2021.

[45] Gu, B., Zhang, et al.. *Abating ammonia is more cost-effective than nitrogen oxides for mitigating PM2.5 air pollution*. Science Vol. 374, No. 6568, pp. 758–762, 2021.

[46] Han, X., Zhu, L., Liu, M., Song, Y., Zhang, M., *Numerical analysis of the impact of agricultural emissions on PM2.5 in China using a high-resolution ammonia emissions inventory*. Atmos. Chem. Pys. Discuss. Vol. 3, pp. 1–31, 2020.

[47] Kanter, D.R., Chodos, O., Nordland, O., Rutigliano, M., Winiwarter, W., *Gaps and opportunities in nitrogen pollution policies around the world. Nat. Sustain*. Vol. 3, No. 11, pp. 956–963, 2020.

[48] O. P. Hulu, M. Sihombing, R. H. Saputro, A. Darmawan, and Y. Herbani, "*Aplikasi Teknologi Nanopartikel Perak (AgNPs) dalam Air Minum dan Bentuk Kabut terhadap Kadar Amonia Ekskreta Broiler*," J. Ilmu Nutr. dan Teknol. Pakan, vol. 17, no. 2, pp. 26–31, 2019.

[49] Ravi Kant Jain, *Experimental performance of smart IoT-enabled drip irrigation system using and controlled through web-based applications*, Smart Agricultural Technology, Vol. 4, No. 100215, 2023.

[50] A. Ullah, O. B. Kharisma, and I. Santoso, "*Fuzzy Logic Implementation to Control Temperature andHumidity in a Bread Proofing Machine*," Indones. J. Artif. Intell. Data Min., vol. 1, no. 2, p. 66, 2018.

[51] Rajesh Bose, Sandip Roy, Haraprasad Mondal, *A novel algorithmic electric power saver strategies for real-time smart poultry farming,* e-Prime - Advances in Electrical Engineering, Electronics and Energy, Vol. 2, No. 1000053, 2022.

[52] G. Patel, V. Pillai, P. Bhatt, S. Mohammad, *Application of nanosensors in the food industry*, in:, Micro and Nano Technologies, Nano sensors For Smart Cities, Elsevier, pp. 355–368, 2020.

[53] O. Debauche, S. Mahmoudi, S. Ahmed Mahmoudi, P. Manneback, J. Bindelle, F. Lebeau, Edge computing and artificial intelligence for real-time poultry monitoring, Procedia Compu.t Sci., Vol. 175, pp. 534-541, 2020.

Available online at:
Al-Fiziya: Journal of Materials Science, Geophysics,
Instrumentation and Theoretical Physics
Website: http://journal.uinjkt.ac.id/index.php/al-fiziya
Vol.6 No. II 2023, 14-29

Comparison of Kirchhoff Migration and Reverse Time Migration in the Time Domain: Case Study of Field "Y" North West Java Basin

Omar Moefti [1,2,*] and Abdul Haris[1]

[1]Master of Physical Science Program, Faculty of Mathematics and Natural Sciences, University of Indonesia, Indonesia
[2]National Research and Innovation Agency, Indonesia

[*]omarmoefti24@gmail.com

Submitted: December; Revised : February; Approved : March; Available Online: March

Abstract. This study evaluates and compares two seismic migration methods, namely Kirchhoff Migration and Reverse Time Migration (RTM), using 2D seismic data in the North West Java Basin. The main objective of the research is to investigate the relative performance of the two methods in restoring the position of reflectors that have undergone distortion due to the propagation phenomenon of seismic waves. The study involves a detailed analysis and comparison of these methods in terms of accuracy and computational time efficiency. The results show that the Kirchhoff Migration method achieves high accuracy in handling reflectors with significant dip angles. Additionally, this method also demonstrates good computational time efficiency. On the other hand, Reverse Time Migration, although recognized as a sophisticated approach, shows less satisfactory results under the conditions of this study, highlighting its dependence on data complexity and velocity model optimality. This research provides important insights for the appropriate selection of migration methods based on geological characteristics and existing seismic data. Kirchhoff Migration emerges as a superior choice, especially for regions with geological complexity and high dip angles. In conclusion, the selection of migration methods should carefully consider the specific characteristics of the relevant region to achieve optimal results.

Keywords: *North West Java Basin, Kirchhoff, Reverse Time, seismic*
DOI : 10.15408/fiziya.v6i2.36356

INTRODUCTION

In the pursuit of exploring energy sources beneath the Earth's surface, geophysical methods such as seismic play a crucial role. The processing of seismic data is an essential step in generating a clear and accurate depiction of subsurface layers. This process involves efforts to enhance resolution and reduce noise that may interfere with interpretation results. Therefore, caution and precision in data processing are paramount to obtain reliable outcomes.

Seismic exploration activities involve the placement of wave sources and receivers on the surface, creating challenges in project implementation. In line with this, the application of a specialized processing method is necessary to reconstruct data and form a model that provides an accurate representation. One critical stage in seismic processing is migration.

Migration is a process aimed at restoring the position of reflectors distorted by the propagation of waves to their original locations. When waves pass through a reflector plane, reflection occurs, altering the reflector's position. Through migration, the reflector's position can be corrected to align with its actual location [1,2]. The accuracy of migration in restoring the original position of reflectors from apparent reflectors is crucial.

This research aims to determine the most optimal migration method in restoring reflectors according to the structure and properties of the subsurface in a specific region. The primary objective of this study is to obtain an accurate model or image through a comparison of migration using Kirchhoff Migration and Reverse Time Migration (RTM) [5] methods on 2D seismic data.

It is hoped that this research will provide significant benefits and serve as a crucial reference for geophysical experts, especially in the field of seismic exploration. The results are expected to serve as valuable information for research in imaging and enhancing seismic resolution.

RESEARCH METHODS

Data Availability

This research was conducted in the western waters of the Java Sea, specifically in the North West Java Basin (Figure 1). The 2D seismic data were acquired by the vessel KR. Baruna Jaya II during the period from November 29 to December 13, 2009. Throughout the acquisition process, the vessel utilized Sercel Airgun with capacities of 150 cu and 250 cu as the seismic source, capable of generating waves that could penetrate the target depth. The seismic equipment on KR. Baruna Jaya II consisted of 192 receivers in a liquid streamer, spaced 12.5 meters apart.

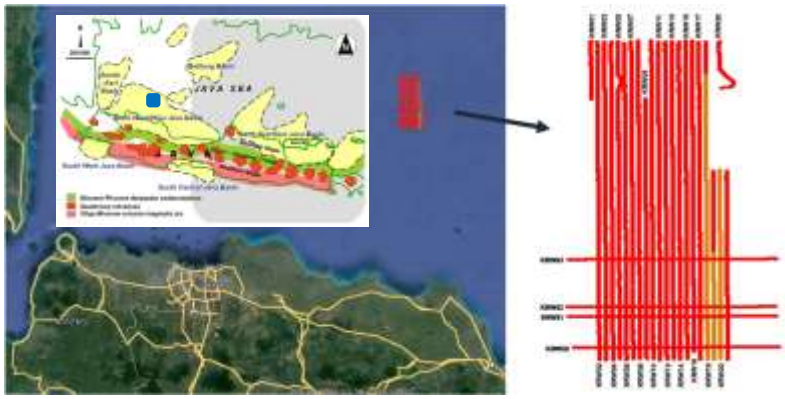

Figure 1. The research area is situated in the Northwest Java Basin, marked by blue box in the inlet map[1]. The seismic lines are overlaid on a Google Earth basemap, with the rightmost side indicating the seismic lines, KRW01 on the left, and KRW021 on the right, arranged sequentially.

As the seismic airgun source, two compressors with a power of 2 x 275 Standard Cubic Feet per Minute (SCFM) were employed to trigger ten airguns with a configuration

of 10 x 150 cu in. The shot distance between each source was set at 25 meters. This configuration yielded survey parameters, including the number of channels, source distance, and channel spacing, resulting in a fold value of 30. Acquisition parameters for this seismic survey included a shot interval of 25 m, group interval of 12.5 m, sample rate of 2 ms, recording length of 5000 ms, and a total of 120 channels.The survey line used in this research was KRW04, comprising 1334 shots from the first station (number 980) to the last station (number 2313). The minimum offset used was 100 m, and the maximum was 1600 m.

Data Processing and Tools

The processes undertaken to achieve the research objectives include geometry construction, trace editing, spectral analysis, filtering and muting, true amplitude recovery, predictive deconvolution, velocity analysis and velocity picking, normal moveout (NMO) and stack correction [2]–[4], Kirchoff Migration [5], and Reverse Time migration [6], and analysis of migration comparison results (Figure 2). In this study, the hardware utilized was the Lenovo ThinkStation C30 with the following specifications: 2 x Intel Xeon E5-2650 for a total of 32 CPUs, 64 GB ECC Register memory, storage using 2 x 256 GB SSDs in a new RAID configuration, and equipped with Nvidia Quadro K4000 graphics card supporting CUDA. The operating system used was Red Hat Enterprise Linux 4, and the software employed was ProMAX.

Vol.6 No. II 2023,14-29
P-ISSN: 2621-0215, E-ISSN: 2621-489X

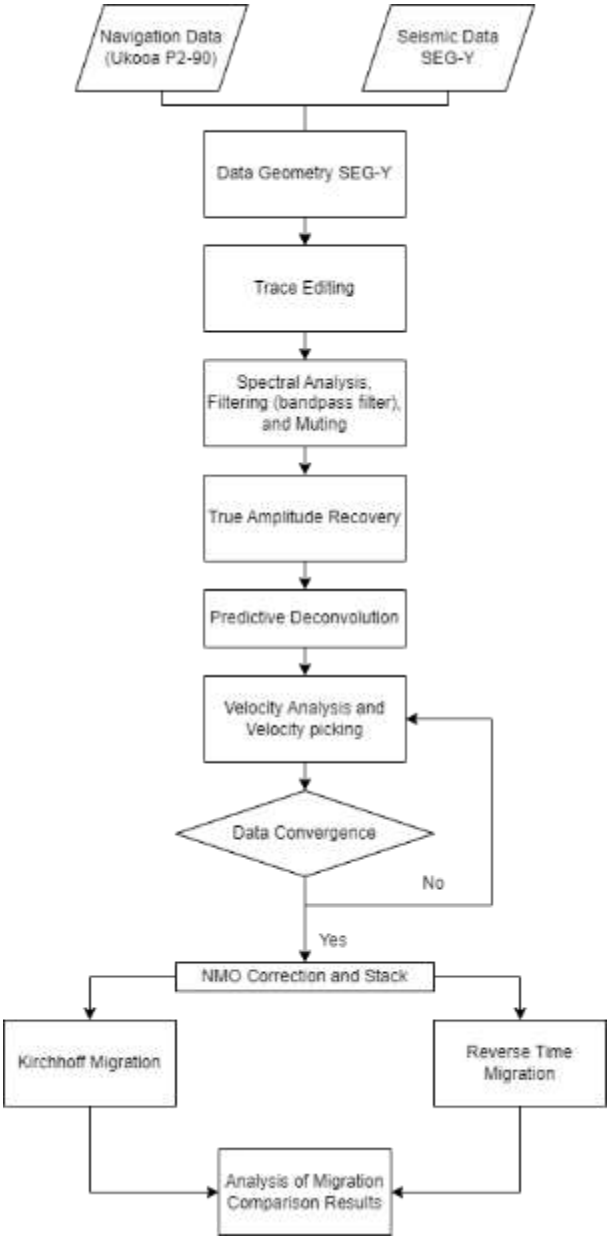

Figure 2. Research flowchart.

Geometry

The geometry process involves merging acquisition parameter data with seismic data to enhance available information. The formation of this geometry is independent of seismic data but utilizes existing marine geometry modules. Seismic data recorded in the field only includes station value (SOU_SLOC), field shot number (FFID), and active channel data. However, to facilitate further data processing and analysis, the addition of other acquisition parameter data such as shot point coordinates, receiver coordinates, common depth points (CDP) coordinates, CDP numbering, offset, and others into seismic data is necessary. Therefore, the Geometry process is crucial to complement this information. Geometry plays a crucial role in determining the true position of the acquired track [7]. Without accurate geometry, the acquisition track may deviate from its intended position.After the database is established, cross-correlation with navigation data can be performed, integrating it into the existing seismic data. Geometry configuration for the KRW04 data involves adjusting parameters based on acquisition specifications and eliminating shots that were not well recorded.

Trace Editing

Trace editing involves two key processes: trace muting and trace killing. Trace muting is a critical step in editing where the goal is to eliminate amplitude values of waves that could disrupt subsequent data processing, including direct waves and refracted waves. This is achieved by multiplying the selected wave amplitudes by zero. On the other hand, trace killing is the process of removing one or more traces deemed problematic during data acquisition, often related to excessive noise generation from specific receivers. The approach for trace killing mirrors that of trace muting, involving the multiplication of wave amplitudes by zero. In the specific case of line KRW04, traces affected by considerable noise or instances of missed shots are identified through the acquisition log, guiding the trace elimination process based on this recorded information.

Spectral Analysis and Bandpass Filter

Spectral analysis is conducted to examine the frequency composition within the data. Through this analysis, we can identify the dominant frequencies present in the data as well as frequencies characterized as noise. This aids in determining the frequency design to be employed. Generally, the frequency range commonly utilized in marine data falls between 10 and 80 Hz. However, this range is highly dependent on the strength of the utilized seismic source and the subsurface conditions of the sea floor. Based on the results of the spectral analysis, a cut-off bandpass value is determined to be 5.76-27.6-109-138 Hz. The results of spectral analysis typically involve frequencies with amplitudes above -20 dB, as these frequencies are considered signal frequencies and dominant frequencies in the data. The application of the bandpass involves using a Butterworth filter.

True Amplitude Recovery

True Amplitude Recovery (TAR) is a process aimed at recovering lost wave energy due to wave attenuation during wave propagation. In this process, the wave energy to be recovered is the energy lost due to geometric spreading. To execute this process, velocity analysis must be performed at least once to have the velocity component as input for geometric spreading correction. Typically, TAR correction that has undergone velocity analysis involves the Spherical Divergence correction process. The Spherical Divergence correction compensates for the loss of amplitude due to spherical wave spreading. If 1/distance is used as the basis for spherical spreading, then the gain correction is:

$$g(t) = t \times v(t) \quad (1)$$

If 1/(time * velocity^2) is used as the basis for spherical spreading, then the gain correction is:

$$g(t) = t \times v^2(t) \quad (2)$$

where t is time, and $v(t)$ is the root mean square (RMS) velocity functions (stacking).

Before TAR is performed, a parameter test is conducted to find the most optimal parameter values to be applied to the data. The optimal parameter values are those capable of revealing reflectors in the lower layers without adding noise. Three parameter

values, namely 2, 4, and 6 will be tested to determine the correction values in dB/sec to be used. These values can be adjusted according to preferences. However, typically, the parameter values in dB/sec applied to seismic data are around the mentioned values. After this process, FLOW TAR will be executed. In this process, the energy to be recovered is the wave energy lost due to geometrical spreading.

Deconvolution

Deconvolution acts as a process used to rectify the effects of wave spreading and eliminate the Earth's natural low-pass filter. When seismic waves propagate through the Earth's layers, convolution occurs between the wave source and the layer reflection response, which functions as a low-pass filter. Through deconvolution, efforts are made to obtain more accurate seismic information by restoring the true amplitude and wave response before experiencing the effects of this filter. One application of convolution is through predictive deconvolution. Predictive deconvolution utilizes the Wiener-Levinson Deconvolution basis by searching for predictable components within the seismic trace and removing them. In this process (Equation 3), sections that exhibit patterns or characteristics that can be mathematically predicted are identified and eliminated from the seismic data [8].

The mathematical equation (Equation 3) commonly used to represent the seismic trace, $x(t)$, is known as the convolution model. In this model, the recorded seismogram is the result of convolving the source signature, $p(t)$ (seismic pulse or wavelet), generated near the surface, with the Earth's impulse response, $e(t)$, along with the presence of additional noise, $n(t)$. Through the use of convolution, the seismic trace is formed by combining the signal from the wave source with the Earth's impulse response, while accounting for the influence of existing noise.

$$x(t) = p(t) \times e(t) + n(t) \tag{3}$$

Velocity Analysis and Velocity Picking

Velocity analysis is a crucial process in seismic data processing aimed at extracting information about the subsurface wave velocity. This velocity information is subsequently employed in various procedures such as true amplitude recovery, Normal Moveout (NMO) correction, and migration. The iterative nature of velocity analysis allows for the refinement of velocity sections, contributing to a more accurate representation of the subsurface structure. The semblance method is utilized for data processing, and the semblance calculation, known as precomputed in the ProMAX software, is preceded by Automatic Gain Control (AGC) to normalize semblance values. Adjustments to parameters, including the absolute offset of the first bin center, maximum offset, and semblance analysis values, are sequentially set to 50 m, 2337.5 m, 1540 m/s, and 4000 m/s, aligning with the KRW04 data parameters. These adjustments are meticulously tuned to achieve optimal outcomes tailored to the characteristics of the specific seismic dataset.

After forming the semblance analysis panel, the process proceeds to velocity picking, adhering to the standard selection of Vrms values for constructing the velocity section. Fundamental rules during picking include ensuring negative gradient velocities, indicating an increase with time, focusing on reflectors rather than multiples (with multiples having velocities around +/- 1500 m/s at twice the seabed time in marine data

cases). The chosen velocity for picking is not always the one with the highest semblance; the critical aspect is that the selected velocity effectively flattens the reflector after NMO correction. Efforts are made to increase interval velocity based on depth, prioritizing picking a velocity that straightens the reflector over obtaining a higher velocity interval from the layer above in certain cases.

The outcome of velocity picking results in a section of RMS velocity. Typically, a velocity section exhibits a geometry resembling the layers beneath the surface. However, strict adherence to this isn't necessary for the initial velocity model. The key criterion is that the selected velocity in the initial model provides effective normal moveout (NMO) correction in the data gather, allowing reflectors to appear straight or parallel. After obtaining NMO correction results, the velocity model can be updated to align with the layered structure following the NMO overlay with existing semblance control. The updated and optimized velocity model becomes crucial as it serves as the basis for migration in areas with complex structures.

Normal Moveout (NMO)

In this step, initial assumptions about the average wave velocity beneath the surface are employed to calculate the expected time difference depending on the distance or offset between the source and receiver. This time difference is then corrected in the seismic record, ensuring that the waves are accurately corrected and can be interpreted correctly. The NMO correction is applied according to Equation 4. $\frac{x}{v}$

$$T_x = \sqrt{T_0^2 + \left(\frac{x}{v}\right)^2} \tag{3}$$

Here, T_x represents the actual reflection time of the seismic event caused by the NMO effect, while T_0 is the reflection time at zero offset for that seismic event. x is the actual distance between the source and receiver, and v is the NMO velocity or stacking velocity for this reflection event.

The stacking process involves the merging or summing of seismic traces at a Common Depth Point (CDP) after applying the Normal Moveout (NMO) correction. To carry out the stacking process, a velocity parameter is required. The velocity used is the best velocity obtained from velocity analysis, and this velocity is subsequently applied in the NMO correction process. Using the best velocity picking results for line KRW05, NMO correction will be performed for each seismic trace before the stacking process. This is crucial to achieve accurate stacking results and generate a clearer image of the subsurface.

Kirchhoff Migration

Kirchhoff Migration, also known as Kirchhoff summation migration, is a migration method based on the summation of diffraction curves. This method employs a statistical approach where a subsurface point can originate from various possible locations with equal probability levels. In practice, Kirchhoff migration is performed by summing the amplitudes from the reflector point along the probable true locations. A reflector plane, commonly referred to as a reflector horizon in a two-dimensional section, is represented

as a superposition of diffraction hyperbolas from points on that plane acting as secondary Huygens sources. Kirchhoff migration relocates these points to their correct positions. This migration can be executed using RMS velocity and straight rays in time-based migration or using interval velocity and ray tracing in depth-based migration. The primary advantage of Kirchhoff migration lies in its ability to produce well-defined steep slopes in migration images. However, one of its drawbacks is a decline in image quality if seismic data contains high noise signals. Kirchhoff migration utilizes mathematical formulas involving convolution operations between the reflector at the target point and the source wavelet to form the resulting waveform.

In time domain migration, we utilize migration velocity and Equation 4 to compute the diffractor surface shape. This involves calculating the wave travel time from each source point to each receiver point. On the other hand, in depth domain migration, we employ the actual wave propagation, determined through the process of ray tracing, from each source to each receiver. This information is used to determine the diffractor surface shape occurring within the medium.

$$t_x = \sqrt{\left(t_0^2 + \frac{(x_s + x_r)^2}{v_{mig}^2}\right)} + \sqrt{\left(t_0^2 + \frac{(x_s - x_r)^2}{v_{mig}^2}\right)} \tag{4}$$

Reverse Time Migration

Reverse Time Migration (RTM) is a recent migration method capable of handling migration processes in complex structures that cannot be addressed by conventional migration methods. This method employs a two-way wave migration approach to produce more accurate imaging in areas with intricate structures and complex velocities, such as sedimentary regions with salt dome intrusions. RTM has proven effective in generating robust models and enhancing the understanding of layer structure boundaries by utilizing diverse velocity values. The utilization of RTM has demonstrated effectiveness in producing accurate models and improving the comprehension of layer structure boundaries at various velocity values [6].

The RTM algorithm employs a finite-difference-based grid staggered method with second to fourth-order accuracy in spatial dimensions. During the migration process, each seismic data gather is processed separately to obtain more detailed and accurate migration images. The equations in the RTM method are modeled Equation 5.

$$m_1(x) = \int F(x,t)R(x,t)dt \tag{5}$$

In the Promax software, the Reverse Time Migration T-K (Time-Wavenumber) performs migration on seismic data that has been offset or stacked, utilizing a reverse-time algorithm in the T-K (time-wavenumber) domain. This migration employs a single interval velocity function, Vint(t), in the time domain, effectively handling variations in vertical velocity. The Promax process utilizes a two-way wave equation and can visualize dips up to and beyond 90 degrees. This method is relatively fast and provides results comparable to Phase Shift Migration. In the case of line KRW05, the migration parameters for the Reverse Time method utilize the RMS velocity obtained through picking and converted using the Dix equation [9].

RESULT AND DISCUSSION

Velocity Model Analysis

In the analysis of the RMS velocity model on the KRW04 profile, the study was conducted up to time 2400 with a specific focus on areas showing distinctive geological features. A comparative analysis was performed between the velocity model and seismic traces before undergoing the Normal Moveout (NMO) process (Figure 4). At this analysis stage, there were interesting variations in velocity values that consistently followed changes in subsurface depth. The peak of the analysis occurred in the initial velocity model at time 1300 and CDP 5000, indicating a significant change in velocity values over a wide range. The initial velocity model was considered adequate as it aligned with the overlaid seismic trace. The seismic trace overlaid initially represents a stack of one channel horizontally, forming a coarse cross-section. The next step involves refining the velocity model by adjusting semblance picking consistency and incorporating additional control from geological layer information that has undergone the NMO process. The high density of picking velocities creates a velocity model with higher resolution compared to the initial model, aiming to enhance the accuracy of migration processes and reveal new features, especially in areas with significant velocity gradients.

Overlaying the final RMS velocity model and NMO on KRW04 (Figure 5) ensures the convergence of the RMS velocity model from the KRW04 profile with the seismic trace. The subsequent step is to convert the RMS velocity model into an interval velocity model using the Dix equation, an essential step to proceed with migration processes using the Reverse Time Migration (RTM). On the other hand, in the RTM method, the algorithm models the backward propagation of seismic waves from receivers to sources. Velocity intervals play a role in estimating wave travel time inside the Earth, influencing the wave contributions at potential reflection locations. The accurate conversion from RMS velocity to interval velocity through the Dix equation ensures that wave travel time estimates align with subsurface layer characteristics. The results of the velocity model transformation after conversion, showing a dense representation of interval velocity ranging from 1800 m/s to 4500 m/s (Figure 6). Although no horizon control is used yet, the red-circled area indicates one of the high-velocity anomalies, ranging from 4000 m/s to 5000 m/s, expected to strengthen the representation of geological features during migration processes using Finite Difference and Reverse Time Migration methods.

Vol.6 No. II 2023,14-29
P-ISSN: 2621-0215, E-ISSN: 2621-489X

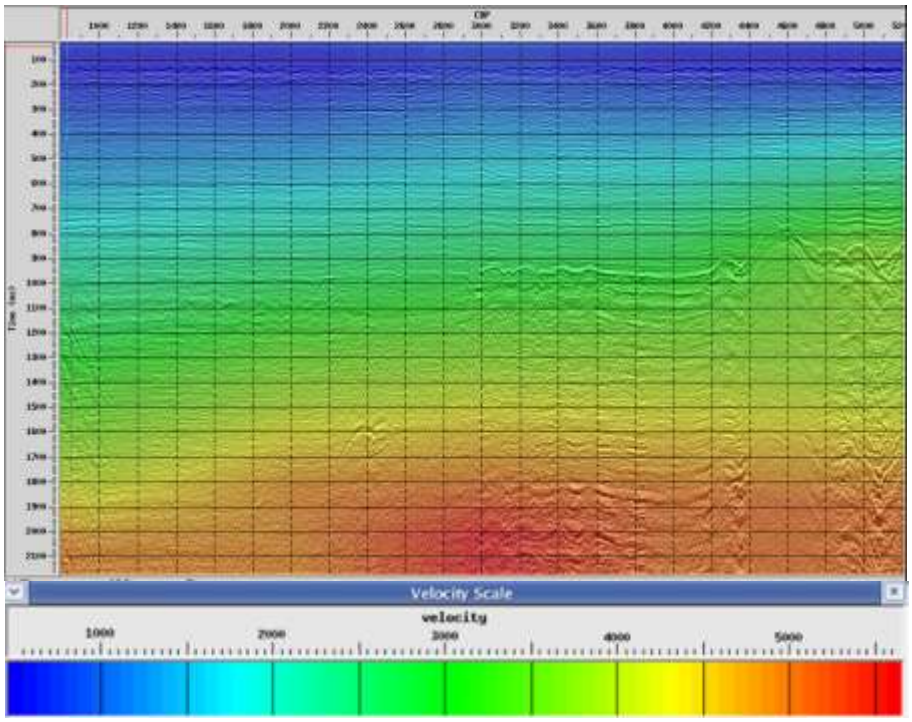

Figure 4. Overlay of the initial RMS velocity model and seismic trace KRW04.

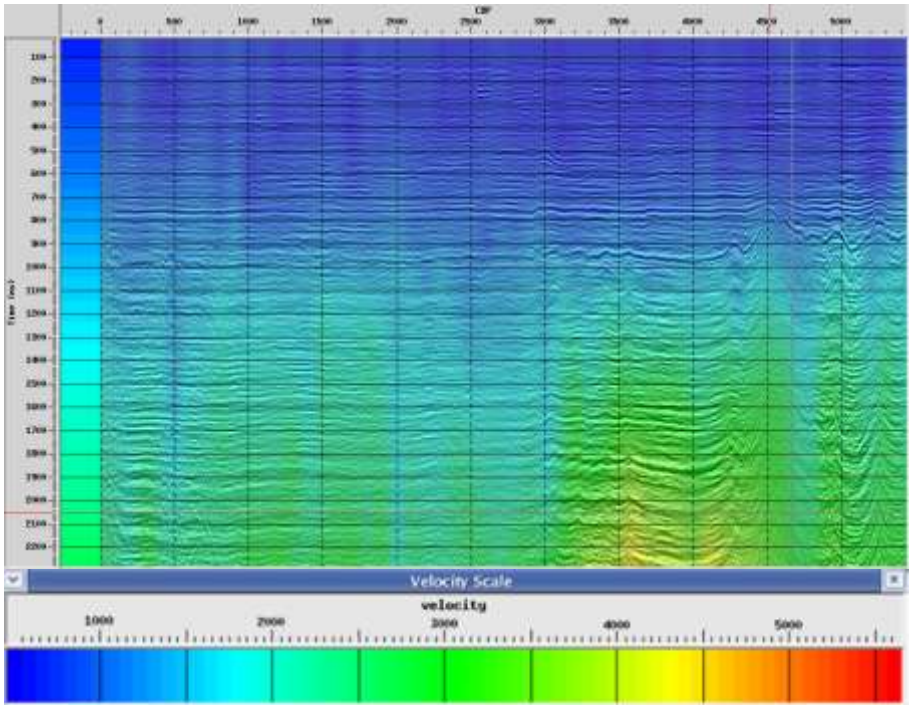

Figure 5. Overlay of the final RMS Velocity model and NMO on KRW04.

Vol.6 No. II 2023,14-29
P-ISSN: 2621-0215, E-ISSN: 2621-489X

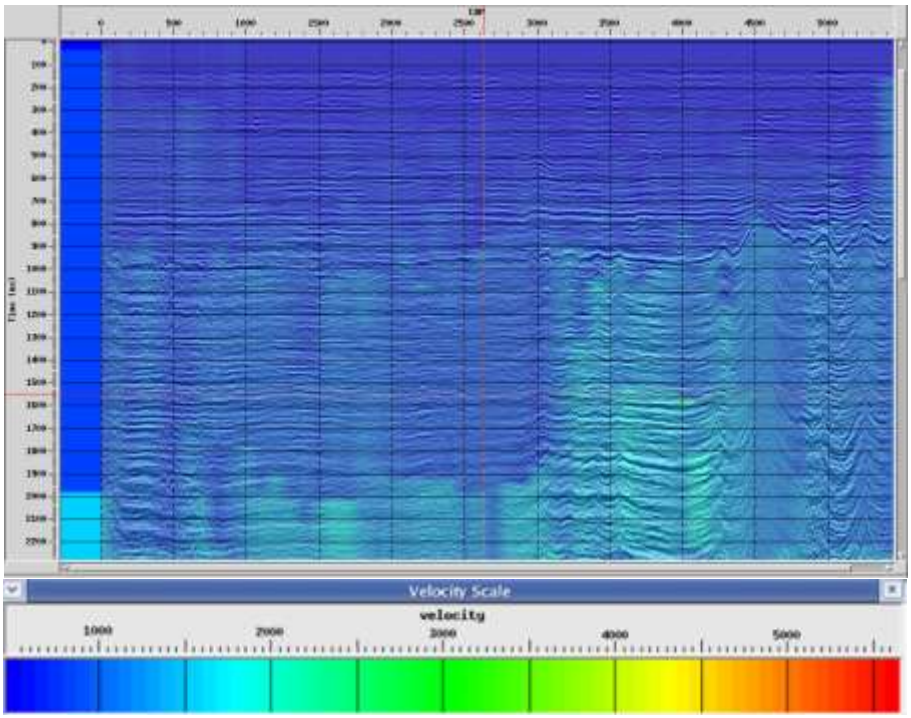

Figure 6. The result of the velocity interval transformation for the KRW04.

Kirchhoff Migration

The results of a series of migration experiments indicate that the use of a low aperture, especially a small aperture, produces images with distinct seismic events, particularly in the layers between traces with high clarity (Figure 7). In the seismic data employed in this study, the use of a low aperture has a significant impact on subsurface imaging, as it only considers data from a small area around the observation point (x, y). This approach enhances the ability to detect small seismic events because small details, both from actual data and noise, are more focused within the small aperture.

In the context of using a large aperture, such as 2000 and 3000, a reduction in clarity in the separation of low-frequency data is observed. This results in difficulties in identifying thin layers present in the data. With a more in-depth observation, it is revealed that the use of a 500 aperture produces the clearest image and demonstrates effective migration capabilities, especially in layers with significant dip angles, as indicated by the red-colored circles. This finding provides valuable insights into improving the quality of subsurface images through the optimization of aperture usage in seismic migration processes.

Vol.6 No. II 2023,14-29
P-ISSN: 2621-0215, E-ISSN: 2621-489X

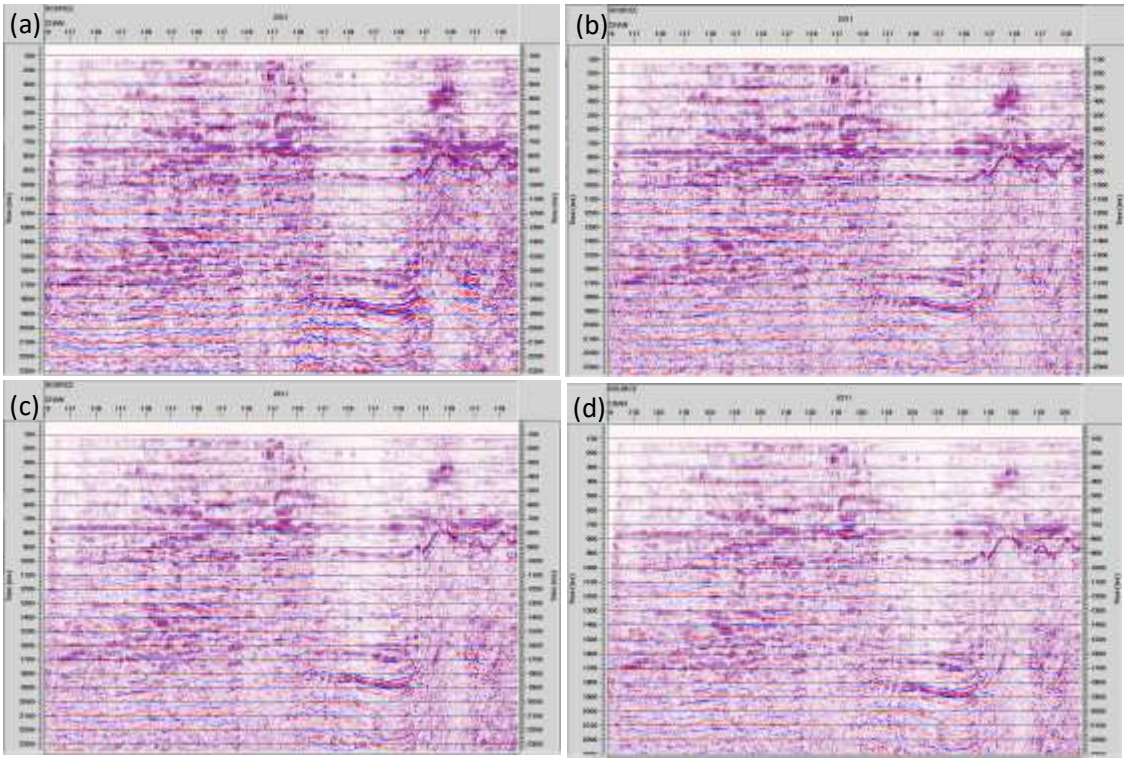

Figure 7. Migration results using the Kirchhoff method with various aperture parameters; (a) 500, (b) 1000, (c) 2000, (d) 3000.

Reverse Time Migration

In Reverse Time Migration (RTM), the process relies on information about changes in seismic wave velocity over time. This migration method employs a single interval velocity function, Vin(t), in the time domain and is capable of handling vertical velocity variations effectively. The RTM process utilizes two-way wave equations, producing images with slopes up to 90 degrees, including reflectors affected by turning-rays. This study varies the speed factor parameter, which controls the trade-off between computational speed and migration result quality, especially for steeply dipping reflectors. With a speed factor greater than 1.0, computations can be accelerated, but there is a risk of losing details on steeply dipping reflectors. The tested speed factors in this study are 1, 4, 7, and 10 (Figure 8). However, from the comparison results, the speed factor component does not show significant differences. The use of the speed factor does not have a notable impact on data with high dips or in areas with high-frequency details. The author opts for the RTM result with a speed factor of 1, which offers high computational efficiency, with the hope of recovering more reflectors to their original positions.

Vol.6 No. II 2023,14-29
P-ISSN: 2621-0215, E-ISSN: 2621-489X

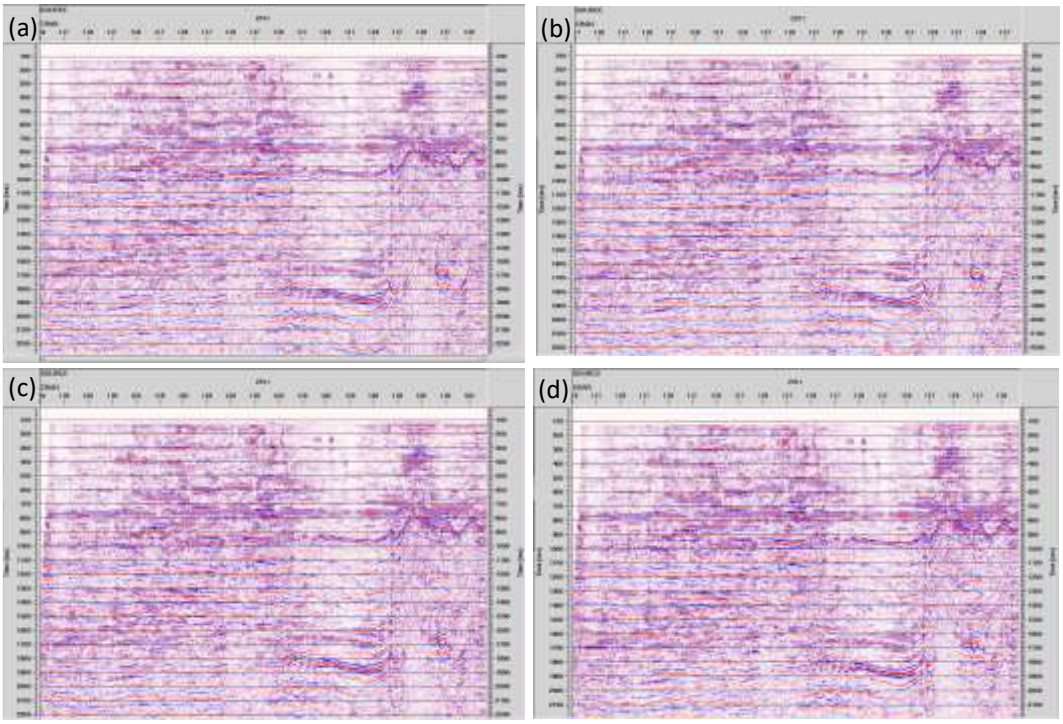

Figure 8. The results of the Reverse Time Migration method with speed factor parameters: (a) 1, (b) 4, (c) 7, (d) 10.

Comparison of results between Kirchhoff Migration and Reverse Time Migration

In the time range between 700 to 2000 milliseconds (Figure 9), highlighted in black circle, the low-frequency area and detailed resolution on the seismic traces appear clearer and more distinct. Structural formations, such as folds, are also more accurately represented in the migration process using the Kirchhoff method with an aperture of 500. However, the Reverse Time Migration (RTM) method shows cleaner results with less accompanying noise. Nevertheless, in the area highlighted with a green box, it is evident that the RTM method encounters challenges when dealing with high-dip areas. This region appears vertically exaggerated and does not smoothly continue into the subsequent layers.

The comparison of migration in areas with less steep dip, within the time range of 500 to 2000 ms, does not reveal significant differences between the Kirchhoff and RTM methods (Figure 10). Nevertheless, the Kirchhoff method demonstrates the ability to recover traces of thin sediments between the main sedimentary traces. This facilitates the horizon picking process and data interpretation, allowing for better identification of finer structures within the sedimentary layers.

Based on the analysis of the time aspect (Table 1) in the computation of Kirchhoff migration and Reverse Time Migration (RTM) methods, it can be concluded that RTM requires high-spec hardware, as indicated by the longer processing time. On the other hand, the Kirchhoff method tends to be more reliable and flexible as it is not heavily dependent on sophisticated hardware. The choice of migration method can be tailored based on specific needs, especially related to the complexity of the data and the available computer resources. In terms of computation time, RTM requires a longer time compared to Kirchhoff.

Vol.6 No. II 2023,14-29
P-ISSN: 2621-0215, E-ISSN: 2621-489X

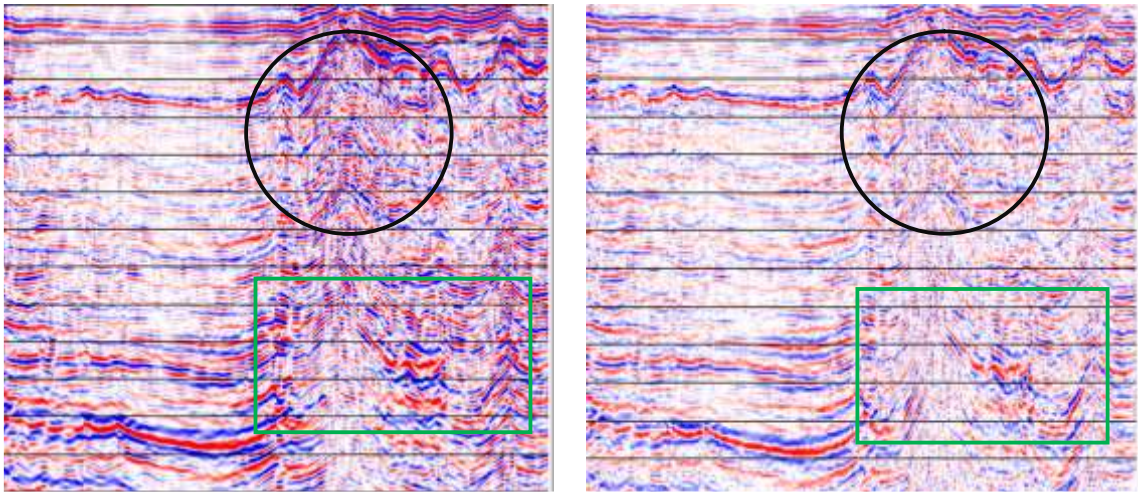

Figure 9. Comparison of structures between 700-2000 ms (Kirchhoff 500 vs RTM1).

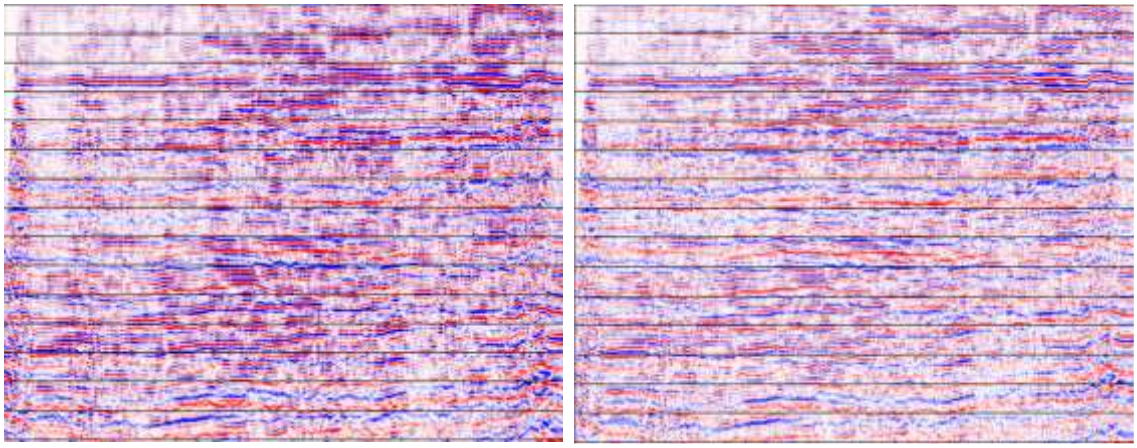

Figure 10. Comparison of 500-2000 ms Flat Layers (Kirchhoff 500 vs RTM1).

Table 1. Computation time of Kirchhoff Migration and Reverse Time Migration in this study.

Migration Method		**Computation Time (minutes)**
Kirchoff Migration	Aperture 500	45
	Aperture 1000	55
	Aperture 2000	80
	Aperture 3000	93
Reverse Time Migration	Speed Factor 1	60
	Speed Factor 4	47
	Speed Factor 7	42
	Speed Factor 10	38

CONCLUSION

The research results demonstrate the superiority of the Kirchhoff method in accurately restoring the reflector's position to its original location, with a significantly higher level of accuracy compared to the RTM method. The notable advantage of the Kirchhoff method lies in its ability to handle reflectors with steep dip angles, reflecting the flexibility and robustness of this method in representing geological structures in the research area. Not only in terms of accuracy, but the Kirchhoff method also excels in computational time efficiency, which is critical in the context of seismic data processing. High computational time efficiency can save resources and enhance the overall processing performance.

On the other hand, the RTM method with the T-K domain, despite being an advanced approach in seismic image processing, shows less satisfactory results in the context of this study. This limitation can be attributed to the complexity of the data used or a less optimal velocity model for the geological conditions in the research area. In conclusion, RTM may be more effective if applied in the Pre-Stack Depth Migration (PSDM) process for seismic data processing in more complex seismic regions.

ACKNOWLEDGMENTS

Thank you to the Marine Survey Technology Center - Agency for the Assessment and Application of Technology (now the National Research and Innovation Agency) for providing the data and software support for the completion of this publication.

REFERENCES

[1] N. Natasia, M. Kurniawan Alfadli, and I. Syafri, "Eocene-Late Miocene Tectonostratigraphy of Bima Field in Northwest Java Basin," *J. Geol. Sci. Appl. Geol.*, vol. 2, no. 3, 2017.
[2] O. Yilmaz, *Seismic Data Analysis*, 2nd ed. Society of Exploration Geophysicists, 2001.
[3] E. Barison *et al.*, "Processing and interpretation of seismic reflection data from the Los Humeros super-hot geothermal system," *Geothermics*, vol. 113, p. 102771, 2023, doi: https://doi.org/10.1016/j.geothermics.2023.102771.
[4] Landmark Graphics Corporation, *SeisSpace® Seismic Processing and Analysis Training Manual*, Volume 1. Houston, Texas: Halliburton, 2011.
[5] G. Liu, Z. Yu, J. Wang, and B. Li, "Accelerating Kirchhoff Pre-stack depth migration on a GPU by overlapping ray tracing and imaging," *Comput. Geosci.*, vol. 128, pp. 79–86, 2019, doi: https://doi.org/10.1016/j.cageo.2019.04.008.
[6] Z. Feng and G. T. Schuster, "Elastic least-squares reverse time migration," *GEOPHYSICS*, vol. 82, no. 2, pp. S143–S157, Feb. 2017, doi: 10.1190/geo2016-0254.1.
[7] M. Steiner and A. Flores Orozco, "formikoj: A flexible library for data management and processing in geophysics—Application for seismic refraction data," *Comput. Geosci.*, vol. 176, p. 105339, 2023, doi: https://doi.org/10.1016/j.cageo.2023.105339.
[8] M. J. Porsani and B. Ursin, "Direct multichannel predictive deconvolution," *GEOPHYSICS*, vol. 72, no. 2, pp. H11–H27, Mar. 2007, doi: 10.1190/1.2432260.
[9] "Dix formula." doi: 10.1093/oi/authority.20110803095723293.
[10] Chapman, M. (2015). Seismic Amplitude: An Interpreter's Handbook. SEG.
[11] Fomel, S., & Shipp, R. (2006). Local seismic attributes. The Leading Edge, 25(2), 150-152.
[12] Porsani, M. J., & de Lima, E. F. (2006). A review of seismic trace attributes and their physical meaning. Revista Brasileira de Geofisica, 24(4), 325-340.

[13] Biondi, B. (2004). Velocity analysis using AB semblance: Geophysical Prospecting, 52(3), 251-257.
[14] Dellinger, J. A., & Gaiser, J. E. (2005). Spectral decomposition and its potential for reservoir monitoring. The Leading Edge, 24(3), 264-270.
[15] Avseth, P., Mukerji, T., & Mavko, G. (2005). Quantitative seismic interpretation: Applying rock physics tools to reduce interpretation risk. Cambridge University Press.
[16] Taner, M. T. (2001). Multidimensional seismic analysis. The Leading Edge, 20(10), 1080-1096.
[17] Rickett, J., Claerbout, J., & Ikelle, L. (2001). Divergence and nonstationarity in prestack seismic data. Geophysics, 66(6), 1850-1860.
[18] Chopra, S., & Castagna, J. (2014). AVO inversion and attribute to rock properties. SEG Technical Program Expanded Abstracts 2014, 3890-3895.
[19] Fomel, S., & Claerbout, J. (2009). Multidimensional recursive filter design. Geophysics, 74(4), WCC1-WCC11.
[20] Aki, K., & Richards, P. G. (2002). Quantitative Seismology. University Science Books.

Available online at:
Al-Fiziya: Journal of Materials Science, Geophysics,
Instrumentation and Theoretical Physics
Website: http://journal.uinjkt.ac.id/index.php/al-fiziya
Vol.6 No. II 2023, 30-43

Analysis of Geothermal Potential Using Gravity Method in Way Ratai Area, Pesawaran Regency, Lampung

Putri Adelia[1,*], Suwondo[1], Agustya Adi Martha[2], Tiara Grace Franzisca[2]

[1]Physics Study Program, State Islamic University Syarif Hidayatullah Jakarta, Indonesia
[2]National Research and Innovation Agency, Indonesia

[*]putriadelia0915@gmail.com

Submitted: Sept; Revised: November; Approved: Desember; Available Online: Desember

Abstract. Way Ratai, Pesawaran is one of the areas in Lampung that has a surface manifestation, in the form of geothermal potential. Based on data from the Directorate of Geothermal in 2017, Way Ratai has a potential of more than 330 MW with the manifestation of hot springs and hot steam. This study aimed to determine the distribution of subsurface density of Mount Way Ratai, Pesawaran, Lampung region by using GGMplus satellite gravity data. Based on fault analysis method and 2D forward modeling in Oasis Montaj software. The results showed that the geothermal area of Way Ratai identified 2 types of faults, namely reverse faults and normal fault. Based on the results of forward modeling, subsurface density of Way Ratai area, Lampung offering can be identified at a density of 1.2 gr/cc suspected alteration rocks in the form of clay minerals, density of 1.55 gr/cc suspected sand gravel, density of 1.6 gr/cc suspected Tuff rocks, density of 2.3 gr/cc suspected breccia rocks and conglomerates, density 2.6 gr/cc suspected schist and chert, and density 2.99 gr/cc suspected basalt rocks.

Keywords: *Gravity Data, GGMplus, Oasis Montaj, Geothermal, Way Ratai.*

DOI : 10.15408/fiziya.v6i2.34659

INTRODUCTION

Background

The potential of geothermal energy sources in Indonesia is quite potential to be developed. Indonesia is included in a country that is rich in geothermal energy sources. This is because Indonesia is located between the confluence of three tectonic plates, namely the Indo-Australian Plate, Eurasian Plate and Pacific Plate [1]. The combination of these tectonic plates causes the formation of distinctive mountains and different types such as active mountains produce geothermal energy sources that make Indonesia have considerable geothermal potential. The potential of geothermal energy in Indonesia ranges from 28,617 MW, which is 40% of the world's geothermal reserves [15 = 2].

Vol.6 No. II 2023, 30-41
P-ISSN: 2621-0215, E-ISSN: 2621-489X

This study is one of the areas that have geothermal potential, namely Way Ratai located in Padang Cermin District, Pesawaran Regency, which is one of the areas in Lampung that has a surface manifestation, in the form of geothermal potential [16 = 3]. Based on data from the Directorate of Geothermal in 2017, the Way Ratai geothermal source has a potential of more than 330 MW with the manifestation of hot springs and hot steam [2=4].

The gravity method serves as an alternative approach to other geophysical methods in assessing the potential of geothermal systems. Gravity method is one of Geophysical methods to determine density distribution of subsurface structure [17=5]. Gravitational methods can provide enough detailed information about subsurface structures through rock density contrast to identify the presence of heat sources below the Earth's Surface [3=6]. Based on the discussion above, in this study will be conducted two-dimensional modeling of subsurface structure Way Ratai Lampung with forward modeling method based on gravity data analysis

METHODS

The research site is located in Way Ratai, Pesawaran Regency, Lampung with the coordinates of the boundary 5°30'59.76" - 5°38'33.54" S and 105° 7'41.52" - 105°15'25.93" E and area 29.86 x 31.04 km. Data processing is done by obtaining secondary data from the site GGMplus. This data processing is done to get the value of Complete Bouguer Anomaly that has been corrected - correction using gravity correction includes free-air correction, bouguer correction, and terrain correction [18=7]. Separation of anomalies in the Complete Bouguer Anomaly (CBA) which produces regional anomalies and residual anomalies. Furthermore, perform fault analysis in the Second Vertical Derivative (SVD) which will display the structure of the fault and fault.

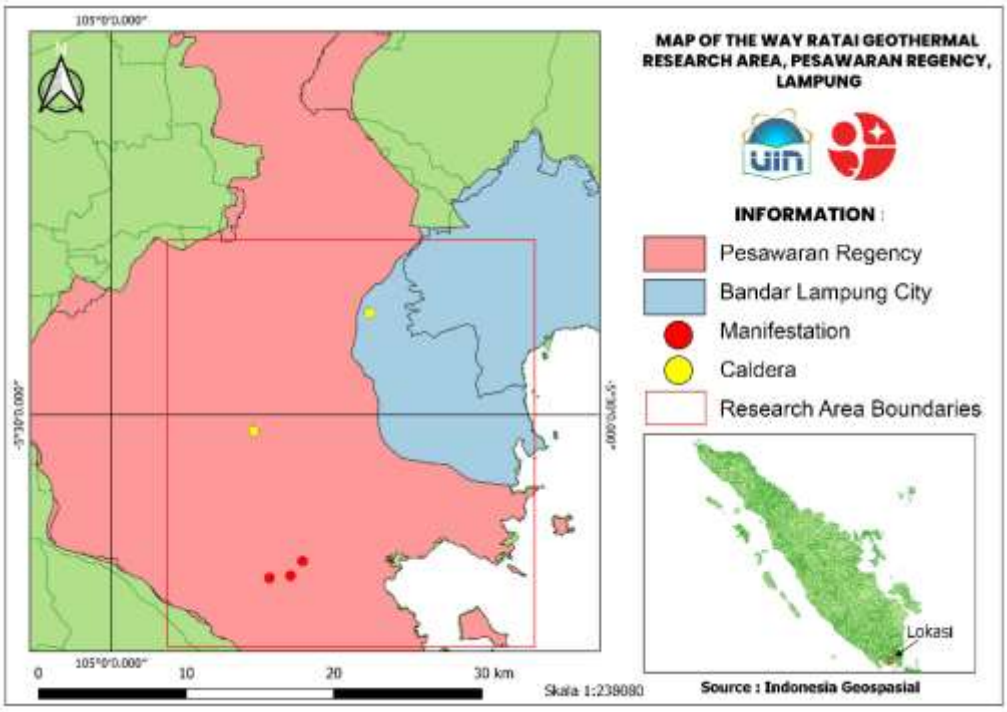

Figure. 4 Research Area Map.

Vol.6 No. II 2023, 30-41
P-ISSN: 2621-0215, E-ISSN: 2621-489X

Way Ratai Geological Setting

Regional geology in the Way Ratai area, Pesawaran is composed of rocks from four groups of rock types, namely tertiary, pre-eruptive volcanic, eruptive volcanic, quarter, and surface deposits. Tertiary rocks around the Way Ratai area are composed of sedimentary rocks from the ratai formation, composed of conglomerates, sandstones, lava breccias and clay rocks that are sometimes associated with andesite tuff. Pre-eruption volcanic rocks are Gebang Volcanic Rock, Gebang Ignimbrite, Gebang Lava, Debris Deposits, and Volcanic Banjarmerger. Rocks are located above tertiary sedimentary rocks. Quaternary volcanic rocks are separated into two eruption sources, namely the eruption of Mount Betung and Ratai at the bottom of the Gebang Caldera. Surface deposits include lava deposits and alluvial deposits [4=8], as **Figure 1.**

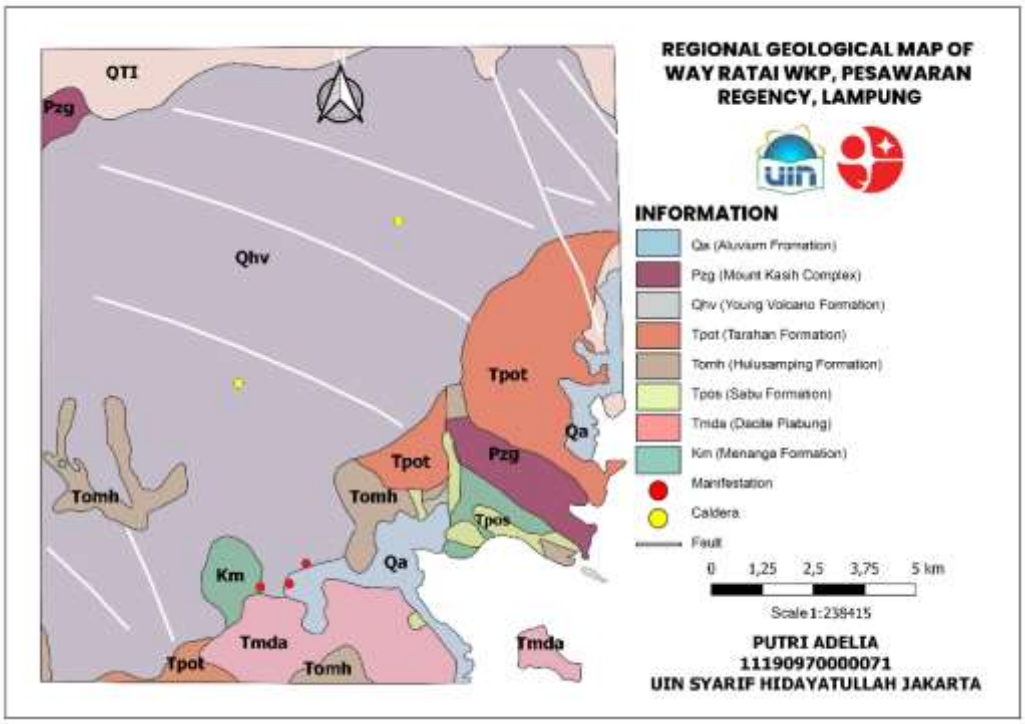

Figure. 1 Geological Map of Research Area [5=9].

Based on the geological map of Way Ratai area is dominated by the first formation, namely, QTI Formation (Lampung formation), Qhv Formation (r, b, p), Km Formation (Menanga Formation), Pgz Formation (Mount Kasih Complex Formation), Tmda Formation (Dacite Piabung), Tpos Formation (Sabu formation), Tpot Formation (Tarahan Formation), Tpos Formation (Sabu formation), Tomh Formation (Hulusamping Formation). Here are the rock formations of this research area on **Figure 2**.

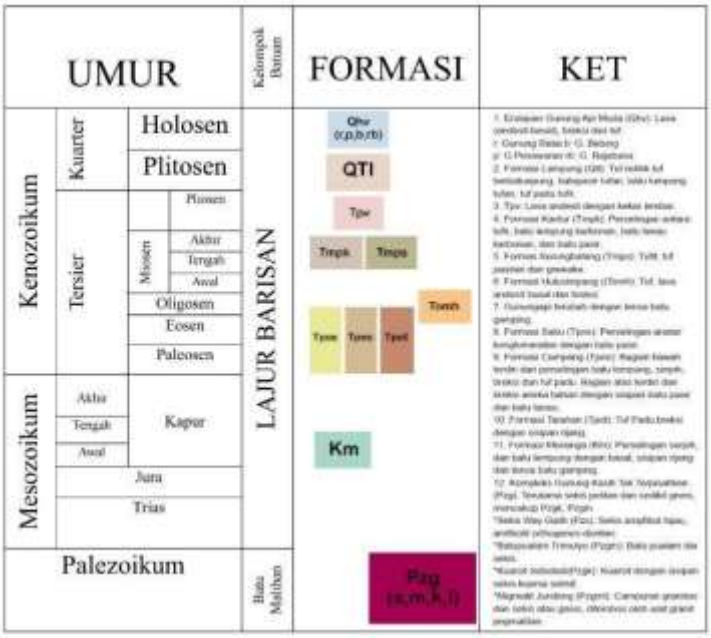

Figure. 2 Regional Stratigraphy on the Tanjung Karang Geological Map Sheet [5=9].

Geothermal System

Geothermal systems are systems that allow fluid from meteoric recharge to fill a reservoir above a heat source [6=10].

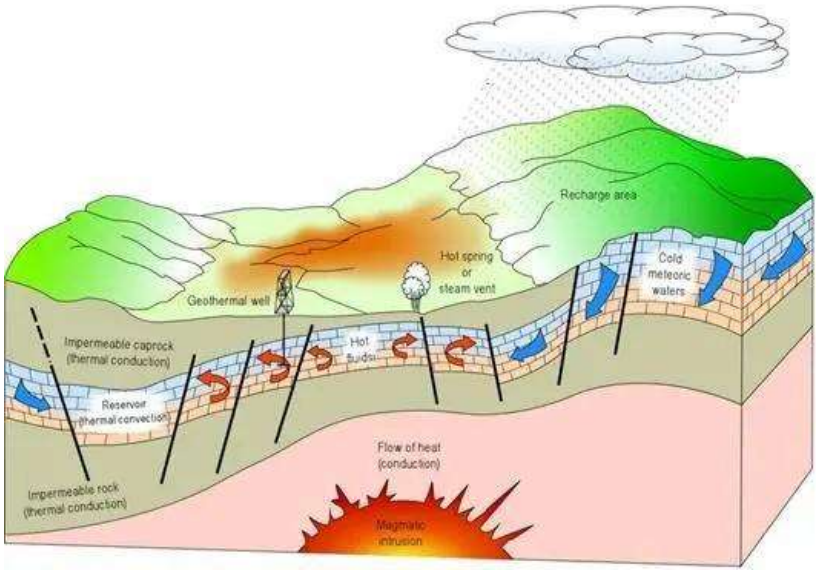

Figure. 3 Geothermal System Schematic [7=11].

The main components of a geothermal system [8=12] are as follows:

1. Heat source, in the bowels of the Earth and usually associated with the presence of volcanoes. Technically, for example, rainwater seeps into the underground rock until it reaches the storage rock.
2. Reservoir rocks are underground rock formations that can store and drain geothermal fluids. Reservoirs tend to be rocks with good porosity and permeability. Porosity serves to store hot liquids while permeability allows hot liquids to flow.

3. A layer of rock at the top of the tank called overburden, which is impermeable to water or difficult for liquids to penetrate. This layer is mostly mudstone because this mudstone can bind water but it is difficult to get out.
4. Recharge area or daerah resapan is an area where water seeps into the subsurface of the Earth. This area usually has a higher elevation. This area has a high water absorption potential than the surrounding area.
5. Discharge areas in geothermal fields are characterized by the appearance of surface manifestations in the form of Wells, hot springs, fumaroles (smoke), and hot pools.
6. Geological structures in the form of faults, fractures, and inconsistencies.

Gravity Correction

Free air correction or free air correction is a correction that occurs due to the effect of differences in altitude (h) to Earth's gravity. Which is where the measurement of gravity on the ground must be adjusted to the height above or below sea level [9=13]. Free air correction is expressed in the equation (1).

$$C_F = 0.3086 \times h \tag{1}$$

Bouguer correction is used to reduce the value of gravity because there is a mass of rock h meters above sea level between the measurement points. So that the measured gravity value is greater than the gravity value that should lie on the equipotential surface [10=14]. Bouguer correction is expressed in the equation (2).

$$C_B = 0.04193 \times \rho \times h \tag{2}$$

Terrain correction or terrain correction is a correction that accommodates the difference in topographic elevation around the measurement area usually within the inner and outer radius, measured elevation. Terrain correction is expressed in the equation (3).

$$C_T = 0.04191 \frac{\rho}{n} (r_2 - r_1 + \sqrt{{r_1}^2 + z^2} - \sqrt{{r_2}^2 + z^2}) \tag{3}$$

First Horizontal Derivative (FHD)

The First Horizontal Derivative (FHD) or the first horizontal derivative has another name, the Horizontal gradient. Horizontal gradients are caused by gravitational anomalies by bodies that tend to show the edges of the body [12=15]. The FHD equation is expressed as follows (5).

$$FHD = \frac{g_{(i+1)} - 2g_{(i)}}{\Delta x} \tag{5}$$

Second Vertical Derivative (SVD)

Second Vertical Derivative (SVD) is a screening technique for gravitational anomalies to obtain the second derivative and which shows little influence from regional effects [13=16]. SVD acts as a high-pass filter, which can describe residual anomalies associated with shallow structures that can be used to identify the type of descending or ascending fault formation [14=17]. The SVD equation is expressed as follows (6).

$$SVD = \frac{g_{(i-1)} + g_{(i+1)} - 2g_{(i)}}{\Delta x^2} \quad (6)$$

2D modeling in this study using a forward modeling method. Forward modeling is done in Geosoft Oasis Montaj software using GM-SYS tools by inputting residual grid data that has been obtained and then draw slicing or lines on the indicated trajectory of geothermal passing through faults and manifestations [19=18]. Modeling is done by making a variety of possible rock formations in each layer and the density of each in the rock. So as to analyze the structure of the subsurface research well.

RESULTS AND DISCUSSION

Complete Bouguer Anomaly or Anomaly Bouguer Lengkap is the result of the observed gravity value g_{obs} obtained by free air correction, bouguer correction, and field correction have been obtained from the value obtained is the result of the value of the acceleration of Earth's gravity [11=19].

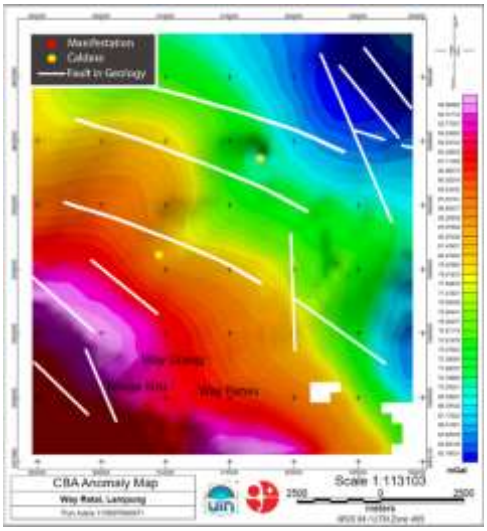

Figure. 6 Complete Bouguer Anomaly Map of Way Ratai, Lampung.

On the map Complete Bouguer Anomaly (CBA) **Figure 6** research area showed results ranging from 63.19 to 94.95 mGal of which there are three types of anomalies, namely low anomalies ranging from 63.19 to 70.78 mgal. This low anomaly dominates in the north to east areas of Pematang Wailimus, Segalamidar and Lebak Budi. A moderate anomaly that ranges from 71.59 to 82.67 mGal. This moderate anomaly dominates in the northwest to southeast, namely the area of Mount Betung and Mount Pesawaran. And

Vol.6 No. II 2023, 30-41
P-ISSN: 2621-0215, E-ISSN: 2621-489X

the anomaly height ranges from 87.83 mGal to 94.95 mGal which dominates in the south to Southwest, namely the area of Pematang Kamtur and Pematang Kubuato.

Separation of regional and residual anomalies resulting from the filtration process on the map Complete Bouguer Anomaly (CBA) using butterworth filter [20]. Viewed from both maps in regional anomaly Figure 7 (a), the resulting contour looks smoother due to the density of the study area deeper so that the resulting rock is deeper (homogeneous). While on the residual anomaly map Figure 7 (b), the resulting contour looks rougher due to the density of the study area is more shallow so that the resulting rock is shallow (heterogeneous).

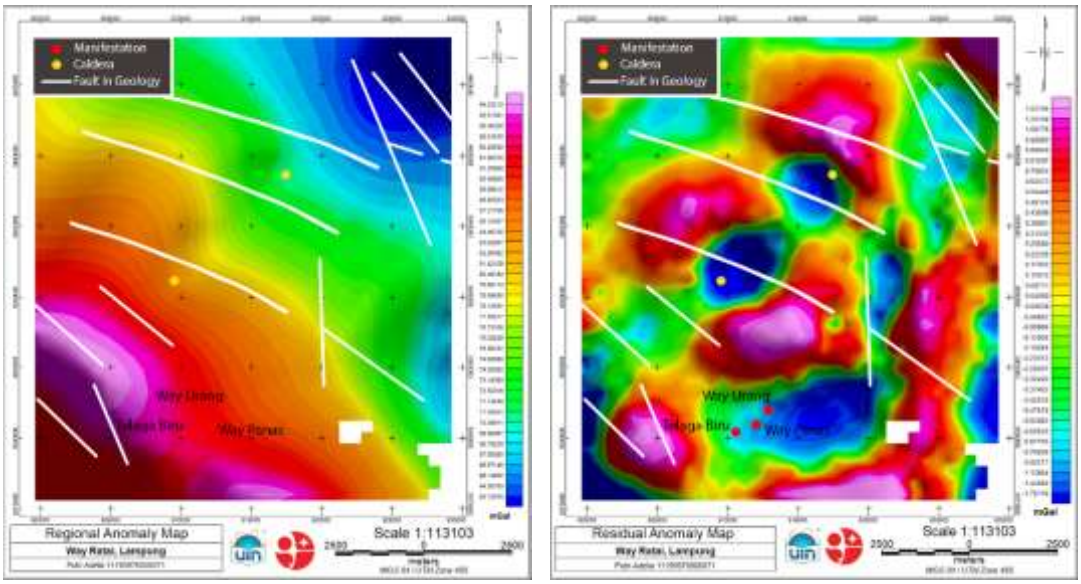

(a) (b)

Figure. 7. (a) Regional Map of Way Ratai, Lampung, (b) Residual Map of Way Ratai, Lampung.

On the regional map **Figure 7(a)** the research area showed results ranging from 63.72 to 94.03 mGal. The low anomaly pattern in the study area is seen to dominate in the north to east, moderate anomaly dominates in the northwest to southeast, and high anomaly pattern dominates in the south to southwest. On the residual map of **Figure 7(b)** the research area showed results ranging from -1.79 to 1.53 mGal. Based on the depth, residual anomalies are shallow anomalies from the surface compared to regional anomalies, residual anomalies have a rougher and closed contour pattern. Positive and negative values indicate the difference in density, position, and body in the rock.

Fault analysis is done by digitizing the grid on the SVD map to determine the type and location of the fault structure. The digitization process is carried out as many as 3 tracks, namely Line a–a' heading southwest to northeast, Line B–B' heading northwest to southeast, and Line C–C' southwest to northeast in Figure 8.

Vol.6 No. II 2023, 30-41
P-ISSN: 2621-0215, E-ISSN: 2621-489X

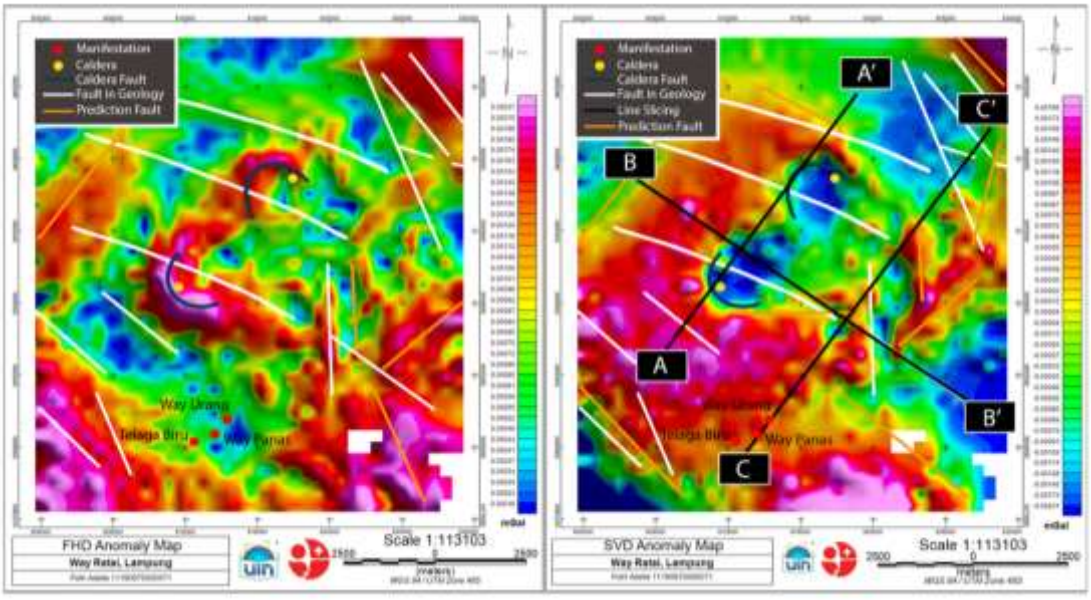

Figure. 8. Track Map FHD and SVD in the Way Ratai, Lampung.

Fault analysis is done by digitizing the grid on the SVD map to determine the type and location of the fault structure. The digitization process is carried out as many as 3 tracks, namely Line A-A' heading southwest to Northeast, Line B-B' heading northwest to Southeast, and Line C-C' Northwest to Southeast. Figure 5. From the results of this analysis obtained values in the form of coordinates UTM X, UTM Y, and SVD values. Fault indication results are shown with SVD values that are worth or close to zero (0).

In the results of the SVD graph, the X axis shows the value of the location of the coordinates on the UTM X and Y axis shows the value of SVD that has been normalized to SVD(n). The result of the graph is visible there will be a comparison between the two values, where the values confirm each other the type of location, as well as the direction of the fault.

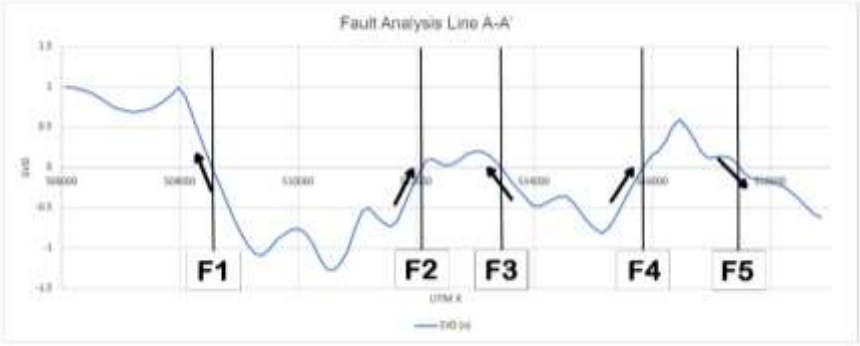

Figure. 10. Fault Point Chart in Line A-A'.

Vol.6 No. II 2023, 30-41
P-ISSN: 2621-0215, E-ISSN: 2621-489X

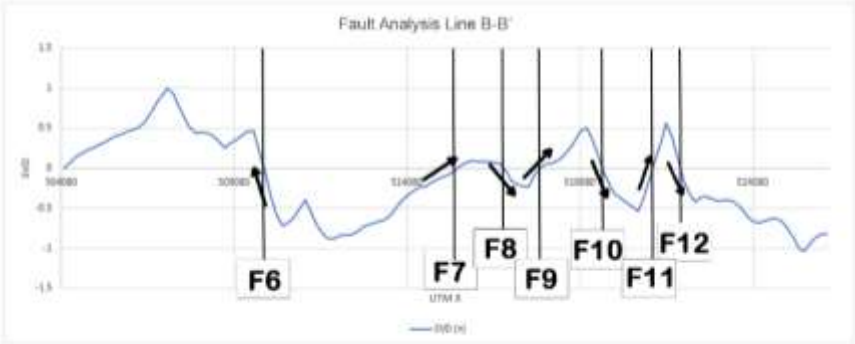

Figure. 11. Fault Point Chart in Line B-B'.

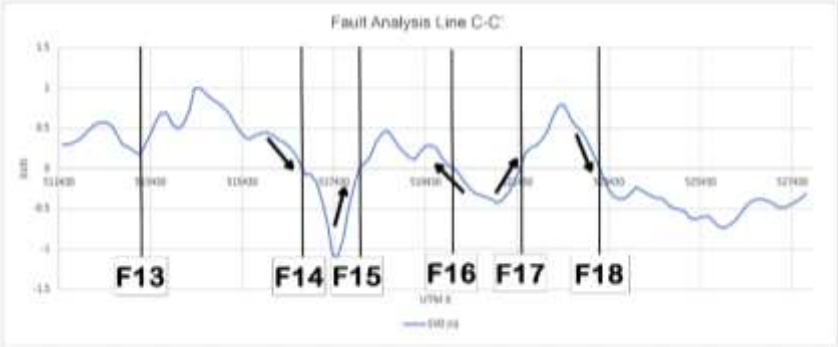

Figure. 12. Fault Point Chart in Line C-C'.

Sourced from the analysis of the three graphs, it was found that the existence of a fault structure at the incision Line A-A ' there are 5 faults, Line B-B' there are 7 faults, and Line C-C' there are 5 faults identified so that a total of three tracks there are as many as 10 faults marked by a black straight line. Then determine the type of fault, from the value $|SVD|min$ and $|SVD|max$. When:

$$|SVD|max > |SVD| = normal\ fault$$
$$|SVD|max < |SVD| = reverse\ fault$$
$$|SVD|max = |SVD| = strike - slip\ fault$$

The results of the calculation and analysis of the fault states that there are 13 types of reverse faults, and 4 normal faults. On Line A-A' shows 5 types of reverse faults and 1 type of normal faults. Then on Line B-B' shows 6 types of reverse faults and 1 normal faults. And Line C-C' shows 3 types of reverse faults and 2 normal faults. Obtained information 17 point fault marked in Black is a reverse fault and white is a normal fault. While the white line is the fault structure based on geological maps, and the black line is the same conjecture on the residual anomaly map.

Vol.6 No. II 2023, 30-41
P-ISSN: 2621-0215, E-ISSN: 2621-489X

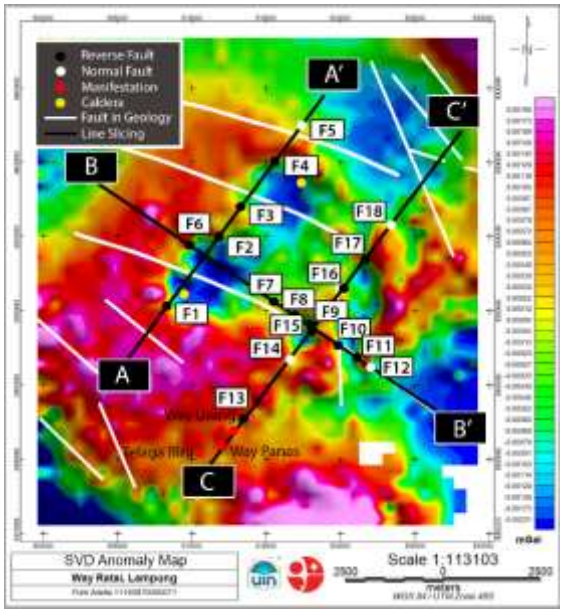

Figure. 9. Fault Point Plotting on SVD Map.

Forward modeling is the process of calculating data from theoretical results that will be observed on the Earth's surface if the model parameters are known. Often the term forward modeling is used for the process of Trial and Error. Forward modeling involves calculating the effect produced by a mathematical model of the expected subsurface conditions by changing the parameters of the model made so as to produce an effect that has an "acceptable" correlation with residual anomalies. 2D modeling in this study there are 3 modeling trajectories using residual anomaly map.

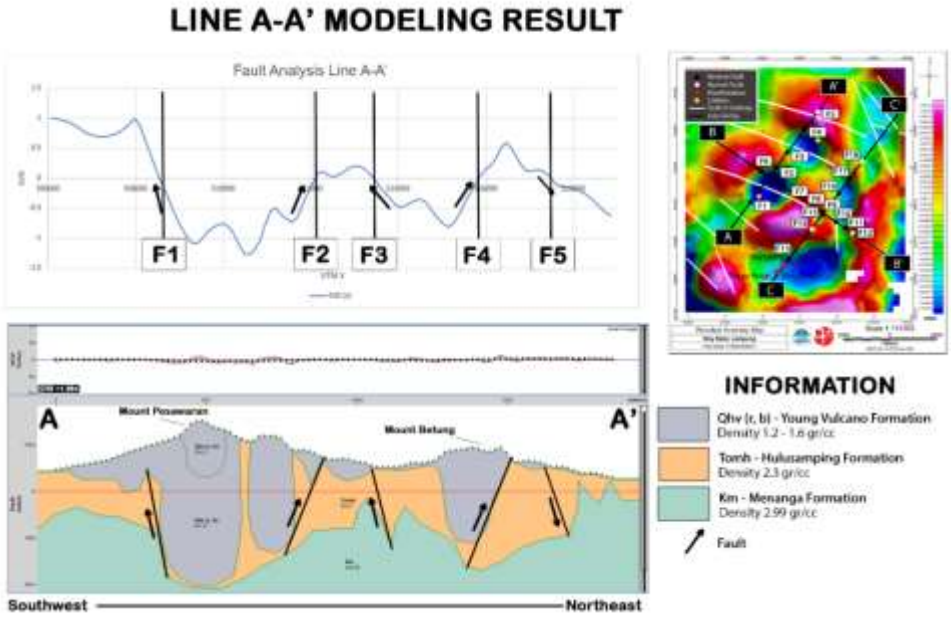

Figure. 13. Results Forward Modelling 2D Line A-A'.

Based on the modeling results of Line A - A ' in **Figure 13**, which is directed from Southwest to Northeast there are 3 layers of rock formation, with rock density values used respectively 1.2 gr/cc to 1.6 gr / cc is suspected as caprock rock rock alteration in

Vol.6 No. II 2023, 30-41
P-ISSN: 2621-0215, E-ISSN: 2621-489X

the form of clay and tuff minerals from the Formation of Young Volcano (Qhv (r, b)). Then the rock density of 2.3 gr / cc is thought to be a reservoir rock, which is a sedimentary rock in the form of breccia from the Hulusamping Formation (Tomh). And the lowest layer with a rock density of 2.99 gr / cc is thought to be an igneous rock in the form of basalt from the Menanga Formation (Km). The fault in the Model Line A-A' is produced in the form of F1, F2, F3, F4, as the reverse fault because the value of SVD_{min} is greater than SVD_{max}. While F5 as a normal fault because the value of SVD_{min} is smaller than its SVD_{max}.

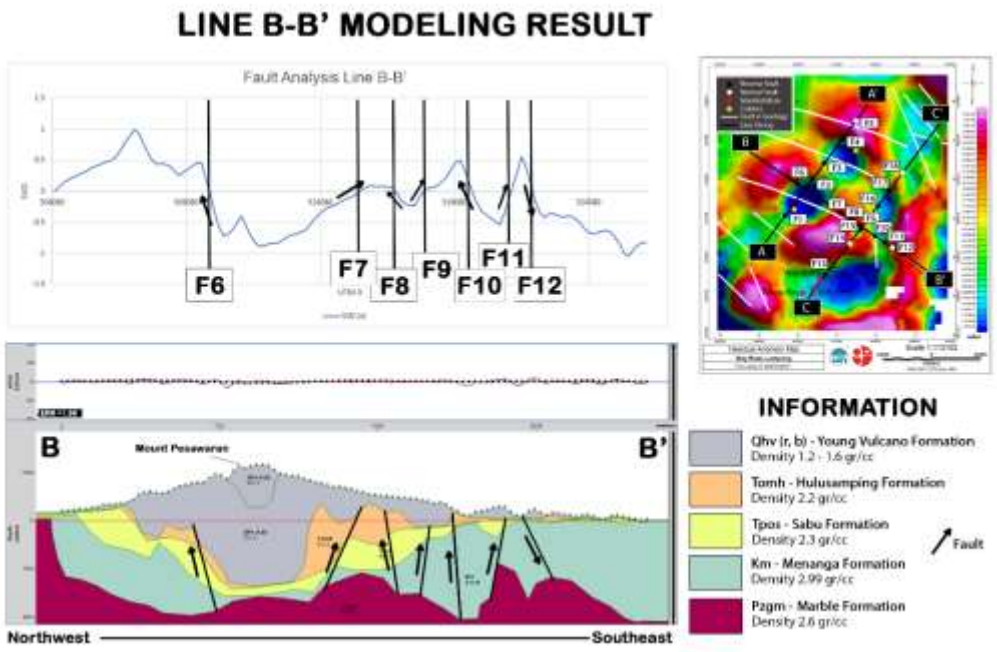

Figure. 14. Results Forward Modelling 2D Line B-B'.

Based on the modeling results of Line B - B ' in **Figure 14**, which is directed from Northwest to Southeast there are 5 layers of rock formations, with rock density values used each 1.2 gr/cc to 1.6 gr/cc is suspected as caprock rocks as well as alteration rocks in the form of clay and tuff minerals from the same formation, namely the Formation of Young Volcano (Qhv (r, b)). Then the second layer with a rock density of 2.2 gr/cc is thought to be a reservoir rock, which is a sedimentary rock in the form of breccia from the Hulusamping Formation (Tomh). The third layer with a rock density of 2.3 gr/cc is thought to be a reservoir rock in the form of a conglomerate from the Sabu Formation (Tpos). Furthermore, the fourth layer with a rock density of 2.99 gr/cc is thought to be an igneous rock in the form of basalt from the Menanga Formation (Km). And in the lowest layer with a rock density of 2.6 gr/cc is thought to be a metamorphic rock in the form of schist from Trimulyo Marble Rock Formation (Pzgm). The fault in the Model Line B-B' is produced in the form of F6, F7, F8, F9, F10, and F11 as the reverse fault because the value of SVD_{min} is greater than SVD_{max}. While F12 as a normal fault because the value of SVD_{min} is smaller than its SVD_{max}.

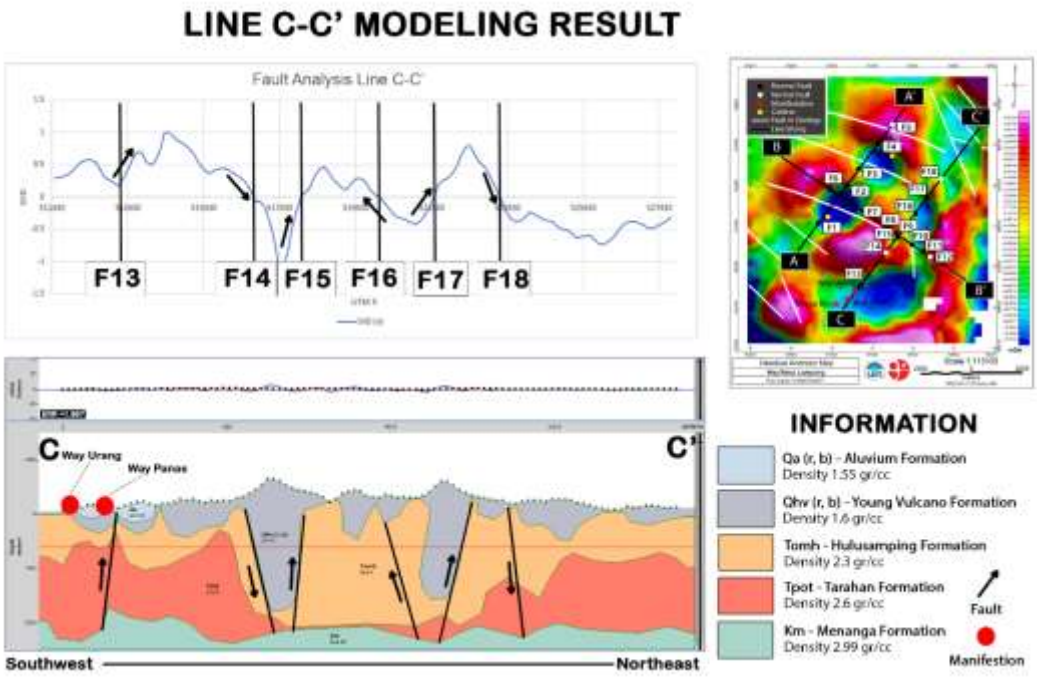

Figure. 15. Results Forward Modelling 2D Line C-C'.

Based on the results of modeling Line C - C ' in **Figure 15**, which is directed from Southwest to Northeast there are 5 layers of rock formation, with the value of rock density used each 1.55 gr/cc is suspected as a caprock rock that is sand gravel from Alluvial Formation (Qa). Then the second layer of rock density of 1.6 gr / cc is thought to be caprock rock as well as tuff rock from the Formation of Young Volcano (Qhv (r, b)). The third layer with a rock density of 2.3 gr/cc is thought to be a reservoir rock in the form of breccia from the Hulusamping Formation (Tomh). The fourth layer with a rock density of 2.6 gr/cc is thought to be a reservoir rock in the form of chert from Tarahan Formation (Tpot). And in the lowest layer with a rock density of 2.99 gr / cc is thought to be an igneous rock in the form of basalt from the Menanga Formation (Km). The fault on the Model Line C-C' is produced in the form of faults F13, F15, F16 and F17 as a reverse fault because the value ofSVD_{min} is greater than SVD_{max}. While F14 and F18 as a normal fault because the value of SVD_{min} is smaller than its SVD_{max}. Line C - C ' there are also 2 geothermal manifestations in the form of hot springs, namely Way Panas and Way Urang, indicating that there is indeed the potential of geothermal systems below the surface of the area due to reverse faults and the presence of reservoir rocks, namely breccia and chert.

CONCLUSIONS

Based on the results of research conducted to the authors draw the conclusion that:

1. Based on the results of forward modeling, subsurface density of Way Ratai area, Lampung offering can be identified at a density of 1.2 gr/cc suspected of alteration rocks in the form of clay minerals, density of 1.55 gr/cc suspected of sand gravel, density of 1.6 gr/cc suspected of tuff rocks, density of 2.3 gr/cc

suspected of breccia and conglomerate rocks, density of 2.6 gr/cc suspected of schist and chert rocks, and density of 2.99 gr/cc suspected of basalt rocks.

2. Based on the results of fault analysis on the Model Line A-A′ there are 4 faults. On Line B-B′ there are 3 faults. And on Line C-C′ there are 3 faults.
3. Potential distribution of geothermal system in Way Ratai area located in Padang Cermin sub-district identified as Way Panas and Way Urang Hot Springs is thought to be caused by reverse faults.

REFERENCES

[1] Hall R, Blundell DJ. *Tectonic evolution of southeast Asia*. vol. 106. Geological Society Publishing House; 1996

[2] Alper Kıyak, Can Karavul, Levent Gülen, Ertan Pekşen, A. Rıza Kılıç (2015), Assessment of geothermal energy potential by geophysical methods: Nevşehir Region, Central Anatolia, Elsevier Journal of Volcanology and Geothermal Research, Pages 55-64.

[3] Peter Bayer, Guillaume Attard, Philipp Blum, Kathrin Menberg, May 2019, *The geothermal potential of cities*, Elsevier Renewable and Sustainable Energy Reviews, Volume 106, Pages 17-30.

[4] G. Direktorat Panas Bumi, Direktorat Jenderal EBTKE Pusat Sumber Daya Mineral, Batubara, dan Panas Bumi, *Potensi Panas Bumi Indonesia*, 2017.

[5] S. Bruce Kohrn, Chloe Bonet, Dan DiFrancesco, Helen Gibson, January 2011, Geothermal Exploration Using Gravity Gradiometry – a Salton Sea Example, researchgate.

[6] Putri, M. K., Suharno, dan Hidayatika, A. 2014. *Introduction to Geothermal System of Way Ratai*. Proceedings Indonesia International Geothermal Convention & Exhibition, 1–5.

[7] Sorja Koesuma, Mela Budiani Septianingsih, and Budi Legowo, Identification of Subsurface Structures of Geothermal Potential Area in East of Mount Lawu Using The Gravity Method, Indonesian Journal of Applied Physics (2020) Vol.10 No.1 halaman 65.

[8] Donovan, R., Karyanto., Ordas Sewanto., 2021. *Studi Sifat Termal Batuan Daerah Lapangan Panas Bumi Way Ratai Berdasarkan Pengukuran Metode Konduktivitas Termal*. Jurnal Geofisika Eksplorasi Vol. 4/No. 3

[9] Mangga S. Andi, ddk. 2010. *Peta geologi lembar Tanjung Katang, Sumatera*. Pusat Survei Geologi. Bandung: Pusat Penelitian dan Pengembangan Geologi, 1993.

[10] Torkis, R., 2012. *Analisa dan Pemodelan Struktur Bawah Permukaan Berdasarkan Metode Gayaberat di Daerah Prospek Panas Bumi Gunung Lawu*. Skripsi. Universitas Indonesia. Depok.

[11] International Geothermal Association. (2004).

[12] Suharno. 2013. *Eksplorasi Geothermal*. Lampung: Penerbit Lembaga Penelitian Universitas Lampung.

[13] Blakey, R.J., 1995, *Potensial Theory in Gravity and Magnetic Applications*, Cambridge University Press.

[14] Andrian, Jefri (2018). *Pemetaan Struktur Basemen Menggunakan Metode Energy Spectral Analysis – Multi Window Test (ESA-MWT) Data Gravitasi Pada Cekungan Sumatera Utara*. Universitas Indonesia.

[15] Zulfawati, Laela, Suhayat Minardi, Lily Maysari Angraini. 2019. *Analisis Spektrum Pada Data Gaya Berat Daerah Lombok Tengah Dan Lombok Timur Untuk Menentukan Estimasi Ketebalan Sedimen*. Jurnal Inovasi dan Pembelajaran Fisika, Volume 06, No. 1, Mei 2019, hal. 34-4.

[16] Zaenudin, A., Sarkowi, M., dan Suharno. (2013, November). *Pemodelan Sintetik Gradien Gaya Berat Untuk Identfikasi Sesar*. In Seminar Nasional Sains & Teknologi V (pp. 269-277). Jurusan Teknik Geofisika Fakultas Teknik, Universitas Lampung.

[17] Lestari, I. & Sarkowi, M. (2013). *Analisis Struktur Patahan Daerah Panasbumi Lahendong - Tompaso Sulawesi Utara Berdasarkan Data Second Vertical Derivative (SVD) Anomali Gayaberat*, Seminar Nasional Sains & Teknologi V, Lembaga Penelitian Universitas Lampung 19-20 November 2013

[18] Dan D. Kosloff, Edip Baysal, Forward modeling by a Fourier method, Geophysics (1982) 47 (10): 1402–1412

[19] Hartati, Sri (2012). *Peningkatan Hasil Belajar Ipa Melalui Penerapan Model Pembelajaran Student Teams Achievement Divisions (Stad) Bagi Siswa Kelas IV Sd Puri 01 Kecamatan Pati Kabupaten Pati tahun Pelajaran 2012/2013*. Skripsi thesis, Universitas Muhammadiyah Surakarta.

[20] M. Nafian, N R Permana, A Anjani, B Gunawan and L A Sanjaya, 2019 Identification 2D Modelling of Subsurface Structure Geothermal Prospect Area by Gravity Method: Case Study in Tanuhi, South Kalimantan ,Journal of Physics: Conference Series.

Available online at:
Al-Fiziya: Journal of Materials Science, Geophysics, Instrumentation and Theoretical Physics
Website: http://journal.uinjkt.ac.id/index.php/al-fiziya
Vol.6 No. II 2023, 44-52

The Effects of Tempering and Cooling Media on The Strength of Hadfield Steel

Putri Sukmayanti [1], Arif Tjahjono [1,*], and Permana Andi Paristiawan [2]

[1]Department of Physics, Faculty of Science and Technology, Syarif Hidayatullah State Islamic University Jakarta, Indonesia

[2]Research Center for Metallurgy, National Research and Innovation Agency (BRIN), Indonesia

[*]arif.tjahjono@uinjkt.ac.id

Submitted : December; Revised : February; Approved : March ; Available Online: March

Abstract: Hadfield steel is a steel known for its good toughness, but it often experiences damage due to excessive loads. In this study, an analysis of the heat treatment process was conducted on Hadfield steel to enhance its strength through homogenization at a temperature of 850°C and tempering at 600°C with a holding time of 30 minutes, followed by a rolling process with a 20% reduction. The data analysis results indicate that the sample cooled using water as the cooling media produced the most optimum strength. This is evident from its tensile strength value, which reached 941 MPa, with a grain size of 3.51 µm. Although its hardness value 351.98 BHN is slightly lower compared to the sample cooled with air, the difference is not significant. The metallographic observations show that there is a phase change in the sample. Initially, the sample only had an austenite phase during the homogenization process. However, after undergoing tempering, there is a phase change to austenite, ferrite, martensite, and carbide phases. This change will result in an increase in the strength of Hadfield steel.

Keywords: Hadfield Steel, Homogenization, Tempering, Cooling Media
DOI : 10.15408/fiziya.v6i2.36379

INTRODUCTION

Steel Hadfield, also known as austenitic manganese steel, has a high content of carbon and manganese, reaching 0.9-1.2% C and 11-14% Mn [1]. The high carbon and manganese content make this material predominantly austenitic at room temperature. The advantages of Hadfield steel are its good toughness, high wear resistance and hardness, and resistance to corrosion [2],[3]. In its applications, this type of steel is widely used in industrial components that require good toughness [4]. However, a common problem is the premature failure of Hadfield steel due to excessive loading, resulting in a significant decrease in its strength.

Several studies have been conducted to improve the strength of Hadfield steel, such as the research by Ilham Azmy et al., which studied the effect of tempering process on the microstructure and post-annealing hardness of austenitic manganese steel. The study showed that tempering process caused a decrease in hardness due to the formation of martensite phase and coarse-grained carbide phase ($FeMn_3C$) within the austenite matrix [5]. Another study conducted by Permana et al, [6] showed that variations in holding time and cooling media during the solution treatment process of $Fe_{12}Mn_{1.5}Mo$ steel result in a microstructure consisting of a dominant austenite phase as the matrix, with the presence of undissolved carbides at grain boundaries and within grains [6]. The manganese content and austenitization temperature also influence the microstructure and mechanical properties of manganese steel, where manganese steel with medium (9-10% Mn) and high (15-16% Mn) manganese content results in a stable austenite structure. Increasing the austenitization temperature in manganese steel leads to the emergence of a dominant austenite phase, which cause the hardness of manganese steel to decrease in the as quenched condition [2].

In this research, a heat treatment process will be conducted on Hadfield steel through 2 stages, namely homogenization and tempering. The homogenization stage is carried out to make the structure of Hadfield steel more homogeneous, with the formation of a fully austenitic phase, while tempering is done to improve the strength of the steel. In addition, variations in cooling media are also conducted in this study to obtain optimal strength, so that the premature failure of Hadfield steel can be avoided before its service life is over.

MATERIALS AND METHODS

A. MATERIALS

The equipment used in this study includes a furnace for heat treatment (Nabertherm LH-15/14"/C440 type), Hypertherm Plasma Cutting Machine, Hardness Brinell Test AFFRI/206 RTD, Tinius Olsen 300SL Testing Machine, and an Olympus BX 53M optical microscope. The materials used in this research are Hadfield steel samples with dimensions of 9.9 cm x 5.56 cm x 1.62 mm, sandpaper (80 to 1500 mesh), polishing cloth (5 m and 1 m), alumina, hardener, resin, ethanol, and 2% nital etchant. The chemical composition of the Hadfield steel sample was analyzed using SpectroLab OES (Optical Emission Spectroscopy), as shown in Table 1 [7].

Table 1. Chemical Composition of Hadfield Steel

Element	Mn	Si	S	C	Ni	P	Mo	Cr	Fe
Wt%	13	0.40	0.03	1.15	10.86	0.045	0.90	0.462	Bal.

B. METHODS

The process begins with cutting the Hadfield steel test sample using a Hypertherm Plasma Cutting Machine with dimensions of 9.9 cm x 5.56 cm x 1.62 mm. Furthermore, 2 stages of heat treatment homogenization and tempering, as well as two

cooling variations using air and water as the cooling media. The homogenization process involves heating the test sample to a temperature of 850 ^{0}C with a holding time of 30 minutes, followed by rolling with a 20% reduction percentage. This is followed by the tempering process, which involves reheating the test sample to a temperature of 600 ^{0}C with a holding time of 30 minutes and rolling with a 20% reduction. Variations are also made in the cooling process, using air and water as the cooling media. Please refer to Figure 1 for the stages of heat treatment for Hadfield steel.

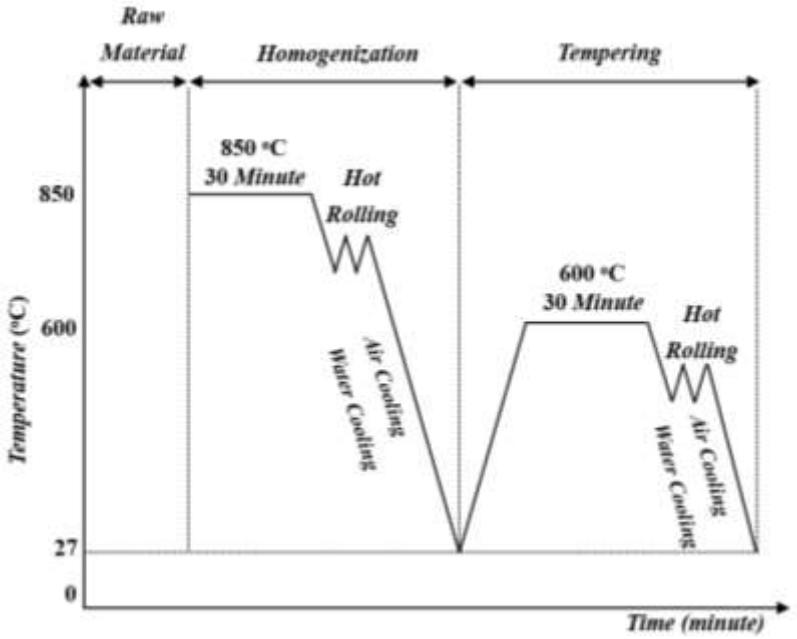

Figure 1. Heat Treatment Process of Hadfield Steel

RESULTS AND DISCUSSION

A. HARDNESS TEST RESULT

The hardness testing in this study was conducted using the Brinell method, which involves applying pressure to the surface of the sample using a steel ball indenter at 5 different points [8]. The results of the hardness testing for Hadfield steel can be seen in Figure 2.

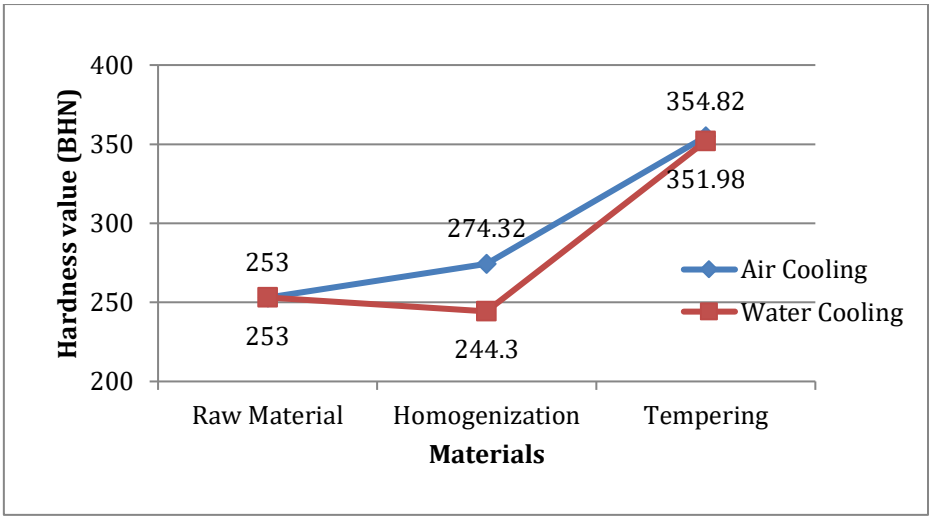

Figure 2. Brinell Hardness of Hadfield Steel

Based on Figure 2, it can be seen that after the tempering process, the hardness value of Hadfield steel increases, whether it is cooled with air or water. This increase in hardness value reaches more than 38% from the previous value, from 253 BHN to 354.82 BHN for air cooling and 351.98 BHN for water cooling. Looking at the given treatment process, this increase in hardness value can be attributed to the hot rolling process [9], as stated in the study by Paristiawan et al., 2020 [10] which indicates that the hot rolling process can increase the hardness value of materials. The difference in cooling processes is also observed in this sample, where cooling with air actually results in a higher hardness value compared to water [11], although the difference is not significant. The slow cooling rate during air cooling will lead to the formation of a stronger structure [12],[13].

B. TENSILE STRENGTH RESULT

Tensile strength testing is a method of testing that involves applying opposing forces to a material in a direction away from the center point. Tensile testing is performed to determine the mechanical properties of a material[14].

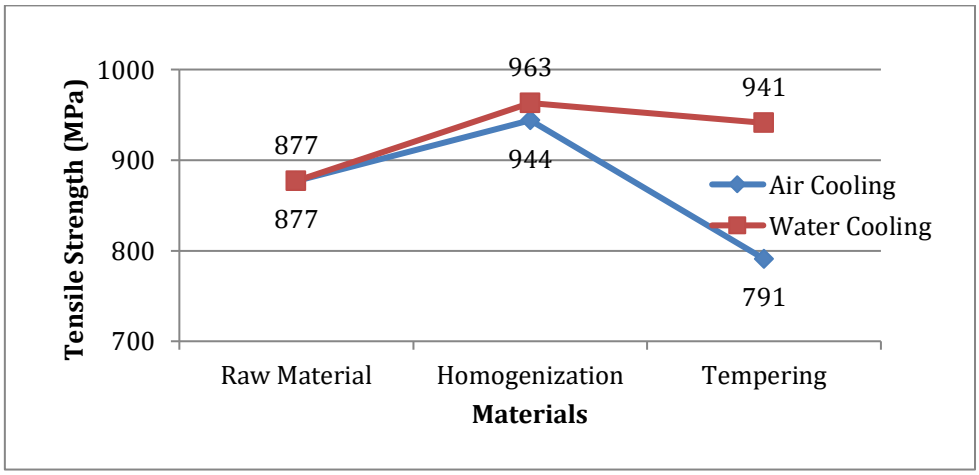

Figure 3. Tensile Strength of Hadfield Steel

Based on the data from the tensile strength test as shown in Figure 3, it can be observed that the tensile strength values of the samples increase after the homogenization process. This indicates the success of the homogenization process, which makes the samples more homogeneous and results in the formation of fully austenite phase and the dissolution of carbides within the grain boundaries [15]. The heating process at 850°C also disperses the carbides more evenly within the grain boundaries, as seen from the metallographic results, leading to an improvement in the sample's toughness. However, after undergoing the tempering process, the tensile strength values decrease again, although they are still higher than the raw material. This occurs because repeated heating processes can cause carbide re-precipitation at the grain boundaries which can reduce the toughness value [16], [17]. Overall, the tensile strength values of the test samples tend to increase, especially for samples cooled using water, from an initial value of 877 MPa to 941 MPa. Although there is a decrease in samples cooled with air compared to before, it is due to the increase in hardness value, which impacts the decrease in tensile strength values of samples cooled with air.

C. METALOGRAPHY

The microstructure of Hadfield steel samples was observed using metallographic techniques with an Olympus optical microscope at a total magnification of 20x. The results of the microstructure observation are presented in Figure 4.

(a)

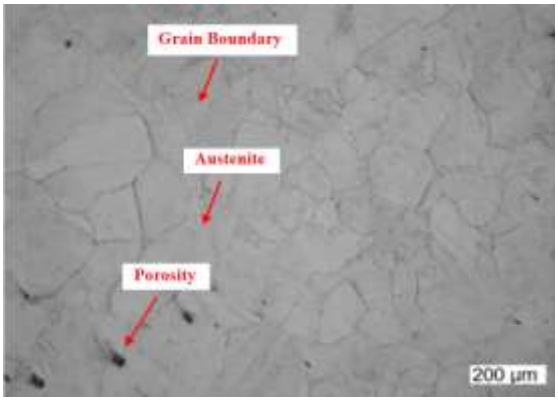

(b)

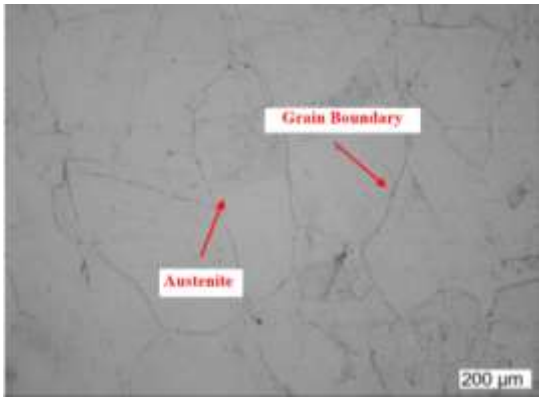

(c)

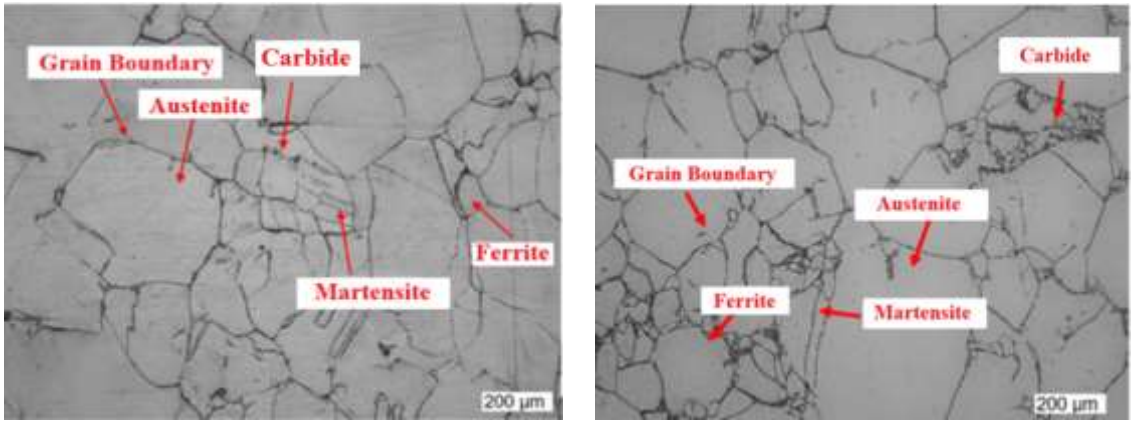

(d) (e)

Figure 4. Optical Microscope Observation Results: Raw Material (a), Homogenization With Air Cooling (b), Homogenization With Water Cooling (c), Tempering With Air Cooling (d), Tempering With Water Cooling (e)

In Figure 4, it can be observed that there is a difference in the phases formed between the raw material and the sample that has undergone the homogenization process at a temperature of 850°C. In both samples cooled with air and water, no carbides were found at the grain boundaries, and carbon atoms in the carbides have fully diffused into the austenite phase. The homogenization process successfully creates a homogeneous sample with a fully austenite phase. The formation of this phase can enhance the toughness of the sample as it is soft and ductile [18], as proven by the increased tensile strength test results. After undergoing the tempering process, in addition to the austenite phase, other phases such as ferrite, martensite, and carbides are also formed at the grain boundaries. All of these phases are detected in the samples that have undergone the tempering process, whether cooled with air or water. The formation of carbide phases is a result of the repeated heating process conducted on the test samples, while the formation of martensite phase is a result of the austenite phase transformation during rapid cooling [19].

D. GRAIN SIZE

The size and shape of grain structures in the microstructure of a material affect its properties, especially its strength, hardness, and toughness.

Table 2. Grain Size of Hadfield Steel

Sample	Grain Size (μm)
Raw Material	5.33
Homogenization Air Cooling	3.81
Homogenization Water Cooling	3.07
Tempering Air Cooling	4.54
Tempering Water Cooling	3.51

In Table 2, it can be seen that the homogenization and tempering processes result in a reduction in the grain size of the samples, from the initial size of 5.33 µm to 4.54 µm for samples cooled with air, and 3.51 µm for samples cooled with water. This is because

the high-temperature heating process has a high energy input, resulting in faster cooling rates and smaller grain growth [20]. Based on Table 2, it is also known that smaller grain sizes lead to better sample strength, as found in the research by Arif et al., 2023 [7]. This is further supported by the tensile strength test results, where samples with a grain size of 3.51 μm exhibit higher tensile strength of 941 MPa compared to samples with a grain size of 4.54 μm, which have a lower tensile strength of 791 MPa.

CONCLUSIONS

Based on the test results, it is known that Hadfield steel can be strengthened through a heat treatment process, which includes homogenization at a temperature of 850 ^{0}C and tempering at 600 ^{0}C with a holding time of 30 minutes, followed by hot rolling with a 20% reduction. The data analysis results indicate that the sample that underwent the cooling process using water as a medium produced the most optimum strength, as seen from its tensile strength value reaching 941 MPa with a grain size of 3.51 μm. Although its hardness value of 351.98 BHN is slightly lower compared to the sample cooled with air, the difference is not significant. The metallographic observation results show that there is a phase change in the test sample. Initially, it only had an austenite phase during homogenization, but after undergoing the tempering process, it transformed into austenite, ferrite, martensite, and carbide phases.

ACKNOWLEDGEMENTS

Specials thanks to the Department of Physics, Faculty of Science and Technology, Syarif Hidayatullah State Islamic University Jakarta and Research Center for Metallurgy, National Research and Innovation Agency (BRIN) who have contributed to this research.

REFERENCES

[1] F. Nurjaman, F. Bahfie, W. Astuti, and A. Shofi, "The effect of solid solution treatment on the hardness and microstructure of 0.6%wt C-10.8%wt Mn-1.44%wt Cr austenitic manganese steel," *J. Phys. Conf. Ser.*, vol. 817, no. April, p. 012066, 2017, doi: 10.1088/1742-6596/817/1/012066.

[2] O. O. Agboola *et al.*, "Optimization of heat treatment parameters of medium carbon steel quenched in different media using Taguchi method and grey relational analysis," *Heliyon*, vol. 6, no. 7, p. e04444, 2020, doi: 10.1016/j.heliyon.2020.e04444.

[3] B. E. dan Y. S. Kurniawan, "Pengaruh variasi *Holding Time* Pada Perlakuan Panas *Quench Annealing* Terhadap Sifat mekanik dan Mikro Struktur Pada Baja mangan AISI 3401," *J. Tek. POMITS*, vol. 3, no. 1, pp. 1–4, 2014.

[4] G. Tęcza and S. Sobula, "Effect of Heat Treatment on Change Microstructure of Cast High-manganese Hadfield Steel with Elevated Chromium Content," *Arch. Foundry Eng.*, vol. 14, no. 3, pp. 67–70, 2014.

[5] I. Azmy, M. A. K. Umam, dan R. Muliawan, "Studi pengaruh proses tempering terhadap struktur mikro dan kekerasan post-annealing baja mangan austenitik," *J. Polimesin*, vol. 19, no. 2, pp. 169–175, 2021, [Online]. Available: http://e-jurnal.pnl.ac.id/polimesin/article/view/2285

[6] F. M. Ridlo, P. A. Paristiawan, dan M. A. Prasetyo, "Pengaruh Variasi Holding Time dan Media Pendingin pada Proses Solution Treatment terhadap Kekerasan dan Ketangguhan Paduan Baja $Fe_{12}Mn_{1,5}Mo$," *Met. Indones.*, vol. 42, no. 2, p. 77, 2020, doi: 10.32423/jmi.2020.v42.77-85.

[7] A. Tjahjono, N. S. Frendyta, and P. A. Paristiawan, "The Effect of Double Solution Treatment on Changes in the Microstructure of Austenitic Manganese Steel," *Chiang Mai J. Sci.*, vol. 50, no. 6, pp. 1–11, 2023, doi: 10.12982/cmjs.2023.060.

[8] Budiarto, "Analisis Pengaruh Temperatur *Normalizing* dan Media Pendingin Terhadap Struktur Mikro, Identifikasi Fasa dan Kekerasan pada Paduan Ingat Bentuk Cu Zn Fe," vol. 15, no. September, pp. 121–137, 2015.

[9] K. Khalid, K. Kardiman, and V. Naubnome, "Pengaruh Variasi Temperatur Tempering Terhadap Sifat Mekanik Dan Sifat Fisik Baja Aisi 1045 Sebagai Bahan Pisau Mesin Pencacah Plastik," *Din. J. Ilm. Tek. Mesin*, vol. 12, no. 1, p. 19, 2020, doi: 10.33772/djitm.v12i1.15007.

[10] P. A. Paristiawan, V. Puspasari, A. W. Pramono, dan B. Adjiantoro, "Pengaruh Variasi Persentase Reduksi pada Proses Pengerolan Panas terhadap Sifat Mekanik dan Struktur Mikro Baja Laterit," *J. Rekayasa Mesin*, vol. 11, no. 2, pp. 297–305, 2020, doi: 10.21776/ub.jrm.2020.011.02.16.

[11] E. Nugroho, S. D. Handono, A. Asroni, and W. Wahidin, "Pengaruh Temperatur dan Media Pendingin pada Proses *Heat Treatment* Baja AISI 1045 terhadap Kekerasan dan Laju Korosi," *Turbo J. Progr. Stud. Tek. Mesin*, vol. 8, no. 1, pp. 99–110, 2019, doi: 10.24127/trb.v8i1.933.

[12] I. Saefuloh, A. Pramono, W. Jamaludin, dan I. Rosyadi, "Studi Karakterisasi Sifat Mekanik Dan struktur Mikro Material Piston Alumunium-Silikon Alloy," *FLYWHEEL J. Tek. mesin Untirta*, vol. IV, no. 2, pp. 56–63, 2018.

[13] M. A. Priadi, I. N. P. Nugraha, dan G. Widayana, "Pengaruh Media Pendinginan Terhadap Kekerasan Dan Struktur Mikro Hasil Pengelasan *Oxy Acetylene* Pada Material Baja St-37," *J. Pendidik. Tek. Mesin Undiksha*, vol. 5, no. 2, 2017, doi: 10.23887/jjtm.v5i2.10397.

[14] A. S. Kurniawan, S. Rr, dan P. Puspitasari, "Analisis Kekuatan Tarik Dan Struktur Mikro Pada Baja St.41 Akibat Perbedaan Ayunan Elektroda Pengelasan SMAW," *J. Tek. Mesin*, vol. 22, no. 2, pp. 1–12, 2014.

[15] F. Bahfie, "Studi pengaruh kadar mangan dan temperatur austenisasi terhadap struktur mikro dan sifat mekanik baja mangan," vol. 10, no. 1, pp. 69–75, 2020.

[16] Abrianto Akuan, "Analisis Struktur Mikro dan Sifat Mekanik Baja Mangan Austenitik Hasil Proses Perlakuan Panas," *Jurnal Teknik: Media Pengembangan Ilmu dan Aplikasi Teknik*, vol. 7, no. 2. pp. 90–99, 2020. doi: 10.26874/jt.vol7no2.284.

[17] M. A. Rizki *et al.*, "Pengaruh Proses *Pack Carburizing* Dengan Variasi Temparatur Dan Karbon Aktif Terhadap Kekerasan Permukaan Baja Aisi 1020," vol. 6, no. 2, pp. 63–67, 2022.

[18] A. Tjahjono, *Fisika Logam dan Alloy*. UIN Jakarta Press, 2013.

[19] R. Adawiyah, Murdjani, dan A. Hendrawan, "Pengaruh Perbedaan Media Pendingin Terhadap Struktur Mikro Dan Kekerasan Pegas Daun Dalam Proses Hardening," *J. Poros Tek.*, vol. 6, no. 2, pp. 55–102, 2014.

[20] M. Ariati, T. W. Sulistio, A. Manaf, dan Sutopo Sutopo, "Persamaan Empiris Pertumbuhan Butir Austenit Baja HSLA-0,019% Nb pada Proses Pendinginan non-Isotermal," *J. Tek. Mesin*, vol. 11, no. 1, pp. 59–66, 2009, [Online]. Available: http://puslit2.petra.ac.id/ejournal/index.php/mes/article/view/17886

Available online at:
Al-Fiziya: Journal of Materials Science, Geophysics, Instrumentation and Theoretical Physics
Website: http://journal.uinjkt.ac.id/index.php/al-fiziya
Vol.6 No. II 2023, 53-62

ANALYSIS OF LANDSLIDE POTENTIAL IN GUNUNG OMEH SUB-DISTRICT LIMA PULUH KOTA REGENCY USING HVSR METHOD

Agma Nabilla [1,*], Syafriani

[1] Department of Physics, Universitas Negeri Padang, Indonesia

[*]nnabilla273@gmail.com

Submitted: November; Revised: February; Approved: February ; Available Online: March 2024

Abstract. On BPBD Lima Puluh Kota designated Gunung Omeh Sub-district as a disaster-prone area due to the detected potential of moving soil. This mobile soil causes gaps in the soil with the potential to continue to move at any time and is exacerbated by unstable soil conditions that cause the risk of landslides. Therefore, there is a need for research in Gunung Omeh sub-district on landslide potential. This research aims to analyse the landslide potential in Gunung Omeh sub-district. Data collection is limited to 9 measurement points using a set of Sysmatrack MAE seismograph sensor type S3S. The data generated is in the form of seismic wave signals which are then processed with the HVSR method using Geopsy software to produce H/V curves with parameters A_0 and f_0. From these two parameters, the values of soil susceptibility index (K_g) and ground shear strain (γ_g) are obtained. The results showed that the susceptibility index ranged from 0.26 x 10^{-6} s^2/cm to 16.34 x 10^{-6} s^2/cm and ground shear strain ranged from 1.32 x 10^{-4} to 2.15 x 10^{-6}. Thus, the highest landslide potential is found at point 6 with the highest susceptibility index of 16.34994479 and ground shear strain of 1.32x$10^{\neg 4}$.

Keywords: *Landslide, HVSR, Seismic Susceptibility, Ground Shear Strain*
DOI : 10.15408/fiziya.v6i2.35996

INTRODUCTION

Landslides are among the most significant natural damaging events in mountain environments. They are one of the primary causes of property damage, loss of life and injuries of persons [1]. Landslides are one of the most common natural disasters in Indonesia. This is because Indonesia has many hilly areas with steep slopes. In addition, the tropical climate results in high rainfall in most parts of Indonesia which is also one of the factors causing landslides. on September 8, 2021 in Nagari Sarilamak, Harau District, Lima Puluh Kota Regency there was high-intensity rain and unstable soil contours resulting in landslides. Landslides is one of the natural disaster symptoms of mass movement of soil or rock down the slope. Landslides are caused by destabilization of the soil or rocks that make up the slope [2]. Soil characteristic parameters that influence the

occurrence of landslides include soil texture, which is related to the movement of water and solutes,air, heat movement, soil volume weight, specific surface area, ease of soil compaction, etc. Lima Puluh Kota districk is an area that has a high level of vulnerability to landslides, although so far there have been no casualties due to natural disasters, especially in the Gunung Omeh District. Gunung Omeh Sub-district has an area of 156.54 km^2, located at an altitude of 800-1100 meters above sea level, has a topography formed by sedimentary rocks, igneous rocks and volcanic products located in the Barisan range zone. On November 24, 2022 BPBD Lima Puluh Kota designated Gunung Omeh Sub-district as a disaster-prone area due to the detected potential of moving soil. This mobile soil causes gaps in the soil with the potential to continue moving at any time and is exacerbated by unstable soil conditions that cause the risk of landslides so that attention is needed to this area.

Efforts to minimize the impact caused by landslides are through disaster mitigation. One of the ways of disaster mitigation that can be done is by identifying areas that have the potential to experience landslides. The identification is done by using geophysical method, namely HVSR (Horizontal to Vertical Spectral Ratio) method. The HVSR method is one of the measurement methods that can be used to determine the characteristics of the subsurface layer structure without causing damage to the structure[3]. Data processing using the HVSR method produces two parameters, namely the dominant frequency factor (f_0) and the dominant amplification factor (A_0) where the dominant frequency represents the rock layer[4] These two parameters are used to obtain seismic vulnerability index and ground shear strain values which are useful as parameters for analysis in identifying potential landslide areas. So from the above problems, further research was conducted on the potential of landslides in Gunung Omeh sub-district.

RESEARCH METHOD

The research method began by taking measurements at 9 points in the Gunung Omeh sub-district with 55 minutes of insurance. Then, the results of microtremor measurements are processed based on the HVSR method. The HVSR method is used to identify local subsurface structures seen from physical parameters in the form of frequency and amplification which are used to estimate the seismic vulnerability index[5]. Then, it is analyzed using geopsy software to obtain an H/V graph to obtain frequency (f_0) and amplification (A_0) values[6].The dominant frequency is the frequency value of the rock layer in the area to show the type and characteristics of the rock. Based on the frequency of the soil, it is formulated with the following equation (1):

$$f_0 = \frac{v_b}{4AH} \qquad (1)$$

Where v_b is the wave velocity below the ground surface, A is the amplification factor and H is the sediment thickness[7].
The following soil classification based on the dominant frequency according to Kanai can be seen in table 1 below:

Table 1. Classification of Seismic Vulnerability Values [8]

No	Dominant frequency (Hz)	Description	Categories
1	6,667 – 20	The thickness of the surface sediments is very thin, dominated by hard rocks.	Hard
2	10 – 4	The thickness of the surface sediments falls into the medium category of 5 - 10 meters.	Medium
3	2,5 – 4	Surface sediment thickness falls into the thick category of about 10 - 30 meters	Soft
4	< 2,5	The thickness of the surface sediments is very thick.	extremely soft

Amplification gives an idea of the change (magnification) of ground motion acceleration of the surface bedrock. The amplification equation can be seen in equation (2) below:

$$A_0 = \frac{\rho_b . v_b}{\rho_s . v_s} \qquad (2)$$

Where ρ_b is the density of bedrock (gr/ml), ρ_s is the density of soft rock (gr/ml), v_b is the speed of wave propagation in bedrock (m/s) and v_s is the speed of wave propagation in soft rock (m/s)[9].
The following amplification classification can be seen in Table 2 below:

Table 2. Classification of Dominant Amplification [10]

Zone	Classification	Amplification Factor Value	Colors in the mapping
1	Low	< 3	Green
2	Medium	3 – 6	Blue
3	High	6 – 9	Yellow
4	Extremely High	≥ 9	Red

Based on the frequency and amplification, the vulnerability index value is obtained using the following equation (3):

$$K_g = \frac{A^2}{f_0} \qquad (3)$$

where K_g is seismic susceptibility, A_0 is amplification and f_o is frequency
The classification of seismic vulnerability index values can be seen in table 3 below:

Table 3. Classification of seismic vulnerability index values[11]

Zone	Value Kg
Low	<3
Medium	3-6
High	>6

The value of ground shear strain in an area estimates the potential for soil layers to shift and move due to earthquake impacts. Ground Shear Strain is applied to impacts caused

by earthquakes including landslides, liquefaction, subsidence and ground shaking[12]. The ground shear strain value can be seen in equation 4 below:

$$\gamma_g = K_g \times 10^{-6} \times \alpha \quad (4)$$

Where γ_g is strain seismic, K_g is seismic susceptibility α adalah PGA

Another input parameter used is Peak Ground Acceleration (PGA), PGA is the value of ground acceleration at a place of earthquake vibration in a certain period of time[13]. The parameters used to obtain the PGA value are the strength of the earthquake and the distance of the earthquake hypocenter to the measurement location. The PGA equation can be seen in equation (5) below:

$$\alpha = 427e^{0,278Mw}(R+25)^{-1.301} \quad (5)$$

Where α is PGA, M_w is earthquake strength and R is hypocenter distance to the measurement site
With

$$R = \sqrt{\Delta^2 + h^2} \quad (6)$$

$$\Delta = \sqrt{(X_1 - X_2)^2 + (Y_1 - Y_2)^2} \quad (7)$$

Where X_1 is latitude of epicenter, X_2 latitude of the measurement point (°), Y_1 is longitude of epicenter (°), Y_2 is longitude of the measurement point (°), Δ is distance episenter (1° = 111,1 km) and h is the depth of the earthquake.

RESULTS AND DISCUSSIONS

Data collection in the research in Gunung Omeh District, Lima Puluh Kota Regency using the HVSR method was carried out at nine points with different coordinates. The distance between measurement points is around 500-700 meters and 55 minutes of recording time. After obtaining the recorded data, the data was processed using Geopsy software to convert the time form to frequency using the FFT process to obtain the H/V curve[14]. The H/V curve shows the analysis of seismic wave data to obtain the dominant amplification value and dominant frequency. The amplification and dominant frequency are related to the type and character of the soil and sediment layer by using equations (1) and (2), then the analysis of frequency and amplification can be seen in table 4 below:

Table 4. Frequency and amplification analysis

Points	Longitude (m)	Latitude (m)	Dominant Amplification	Classification	Dominant Frequency (Hz)	Soil Character Classification
1	100.412538	-0.093735	4.29631	Medium	3.05425	Soft
2	100.4 14253	-0.094846	2.94077	Low	8.25293	Hard

3	100.412178	-0.090658	3.64844	Medium	2.96886	Soft
4	100.413076	-0.088669	4.26677	Medium	7.53724	Hard
5	100.414812	-0.090216	2.845	Low	4.57499	Medium
6	100.416951	-0.090026	6.6508	High	2.7054	Soft
7	100.41535	-0.09373	3.67754	Medium	5.92698	Medium
8	100.411231	-0.092512	1.79365	Low	12.0908	Hard
9	100.413712	-0.091405	3.12717	Medium	6.81838	Hard

Based on Table 4, the results of the dominant frequency analysis can be concluded that Points 1, 3 and 6 have soft soil characteristics, points 5 and 7 have medium soil characteristics and points 2, 4, 8 and 9 have hard soil characteristics. Frequency is related to the type and character of the soil and the thickness of the sediment layer. The smaller the dominant frequency value (f_0), the thicker the sediment layer and the deeper the base layer. And for theoretical amplification if the dominant amplification value (A_0) is greater then the sediment in the area is softer and vice versa. Based on table 4, it can be concluded that the classification is low to high. With the highest peak at point 9 and has a soft sedimentary soil condition. Then, from the frequency and amplification values, the seismic vulnerability index value is obtained [15]. using equation (3). The following are the results of the seismic vulnerability analysis and its classification based on Table 5:

Table 5. Soil Vulnerability Analysis

Points	Longitude (m)	Latitude (m)	Seismic Vulnerability Index (K_g)	Classification
1	100.412538	-0.093735	6.043473722	High
2	100.414253	-0.094846	1.047885805	Low
3	100.412178	-0090658	4.483577681	Medium
4	100.413076	-0.088669	2.415383646	Low
5	100.414812	-0.090216	1.769189659	Low
6	100.416951	-0.090026	16.34994479	High
7	100.41535	-0.09373	2.281819823	Low
8	100.411231	-0.092512	0.266084984	Low
9	100.413712	-0.091405	1.434239835	Low

Based on Table 5, it explains the vulnerability index values data at 9 research points. Analyzed the vulnerability index values of frequency and amplification values in the Gunung Omeh sub-district area. The seismic vulnerability index value obtained ranges from 0.266084984 to 16.34994479 with a classification in the low to high category. It can be seen that the highest value is at point 6 with a high classification and the lowest at point 8 with a low classification. The following contour map of the seismic vulnerability index analysis results based on table 5 is shown in figure 1:

Vol.6 No. II 2023, 51-60
P-ISSN: 2621-0215, E-ISSN: 2621-489X

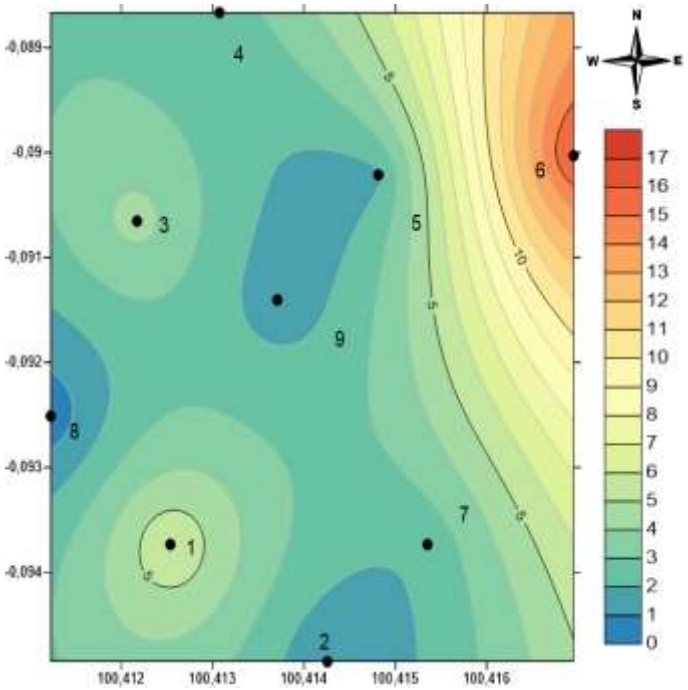

Figure 1. Seismic Vulnerability Index Distribution Map

Figure 1 shows a contour map with soil susceptibility index value of Gunung Omeh Sub-district ranges from 0 to 17 by connecting the susceptibility index value in table 5, then obtained soil susceptibility index of Gunung Omeh Sub-district especially aisle Pandam Gadang is included in the low to high landslide potential zone. Points 2, 5, 8 and 9 are dominated by blue color so they have low landslide potential, points 1, 3, 4 and 7 are dominated by green to yellow color so they have medium landslide potential and point 6 is dominated by red so it has high landslide potential. This is in line with the opinion of Rendi W.K and Wahyudi N.P which states that if the value of seismic vulnerability is greater, the level of risk of damage caused will be greater[16].

The level of risk of damage is also related to the geological conditions in the Gunung Omeh sub-district, especially the Pandam Gadang area, which has constituent materials consisting of pumice and andesite, Miocene sandstone and early tertiary andesite. According to the rock constituent material, the density characteristics of this type of rock are relatively small because this rock constituent material is classified as having low to medium water permeability[17]. The characteristics of these materials in the rainy season have the ability to absorb water and have the potential for landslides. The ground shear strain value is influenced by the seismic vulnerability index and peak ground acceleration (PGA) [18]. Next, to analyze the strain value (γ_g) obtained based on equation (4) shown in table 6:

Vol.6 No. II 2023, 51-60
P-ISSN: 2621-0215, E-ISSN: 2621-489X

Table 6. Analysis of soil shear strain values

Point	Longitude (m)	Latitude (m)	Ground Shear Strain (γ_g)
1	100.412538	-0.093735	$4.87x10^{-5}$
2	100.414253	-0.094846	$8.42x10^{-6}$
3	100.412178	-0.090658	$3.63x10^{-5}$
4	100.413076	-0.088669	$1.96x10^{-5}$
5	100.414812	-0.090216	$1.43x10^{-5}$
6	100.416951	-0.090026	$1.32x10^{-4}$
7	100.41535	-0.09373	$1.83x10^{-5}$
8	100.411231	-0.092512	$2.15x10^{-6}$
9	100.413712	-0.091405	$1.16x10^{-5}$

Table 6 shows the shear strain data obtained from 9 test points. The shear strain values obtained ranged from $2.15x10^{-6}$ to $1.32x10^{-4}$. The higher the shear strain value of an area, the higher the landslide potential of the area. It can be seen that the highest value is found at point 6 with a value of $2.15x10^{-6}$ and the lowest value is found at point 8 with a value of $1.32x10^{-4}$. According to Table 6, the soil shear strain distribution map is shown in Figure 2:

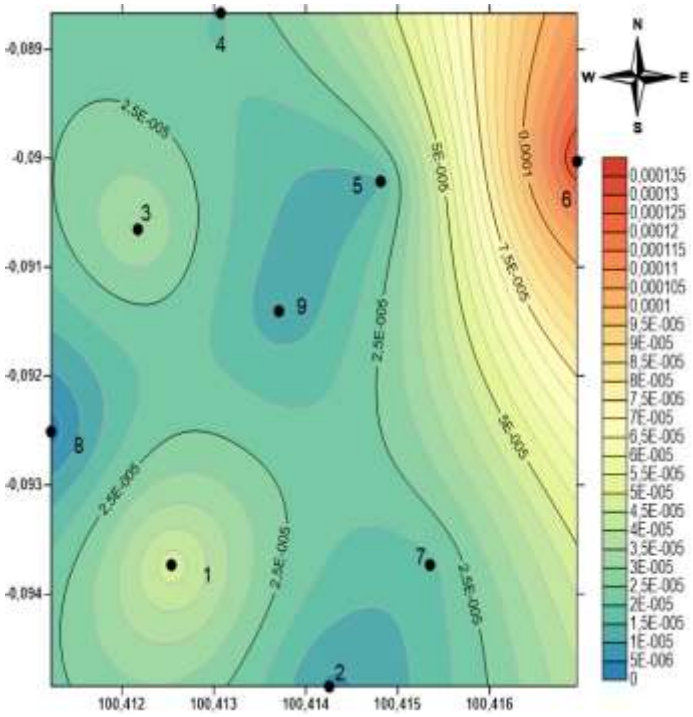

Figure 2. Strain distribution map in Gunung Omeh Sub-district

Figure 2 is a contour map of the ground shear strain value in Gunung Omeh Subdistrict specifically Jorong Pandam Gadang by connecting with table 3, It is obtained that the ground shear strain is included in the low to high landslide potential zone. Points 2, 5, 8 and 9 are dominated by blue color so they have low landslide potential, points 1, 3, 4 and 7 are dominated by green to yellow color so they have moderate landslide potential and point 6 is dominated by red color so it has high landslide potential. The soil layer will experience static conditions if the shear strain value is around 100 x 10^{-6} and for shear strain values >10,000 x 10^{-6} soil conditions are prone to fractures, landslides, and liquefaction in the event of an earthquake[19]. Some plate boundaries glide past each other smoothly, while others are punctuated by catastrophic failures. Some earthquakes stop after only a few hundred metres while others continue rupturing for a thousand kilometres. Earthquakes are sometimes triggered by other large earthquakes thousands of kilometres away [20]. The strain value obtained in the Gunung Omeh sub-district of Lima Puluh Kota regency is about 0.266084984 and the soil strain is 2.15x10-6. From the value of soil shear strain obtained from the research site, several points have the potential to experience the phenomenon of landslides, soil compaction and liquefaction. According to the research of Ayu Shaleha et al, who also studied the identification of soil layer structure in landslide prone areas in Banyubiru Subdistrict, Semarang Regency using HVSR method. Based this research, the strain results obtained were 10.5 x 10-1- 191.8 x 10-1, thus showing the potential for landslides.

It can be concluded that the analysis of potential landslides uses the HVSR method with parameters of seismic vulnerability index and soil shear strain: Potential landslides in Gunung Omeh District are divided into 3 categories. The 3 categories are low, medium and high. The highest value is shown at point 6 with susceptibility index value of 16.34994479 and soil strain of 1.32 x 10^{-4}. The lowest value at point 8 with susceptibility index value of 0.266084984 and soil strain of 2.15x10^{-6}. The analysis is also validated by the soil characteristics, strain, and geology of Gunung Omeh Sub-district.

CONCLUSIONS

Based on the result of the research, it can be concluded that the landslide potential using HVSR method with seismic susceptibility parameter (K_g) has a value range of 0.266084984-16.34994479 and ground shear strain with a value range of 2.15 x 10^{-6}-1.32 x 10^{-4}. Landslide potential in Gunung Omeh sub-district has low to high potential where the highest landslide potential is shown at point 6 (northeastern part of the study area) with a vulnerability index value of 16.34994479 and ground shear strain of 1.32 x 10^{-4}. The research results also refer to the soil characteristics, strain and geology of Gunung Omeh District.

REFERENCE

[1] Jan Blahut, Cees J. van Westen, Simone Sterlacchini. (2010). "Analysis of landslide inventories for accurate prediction of debris-flow source areas". Geomorphology, Volume 119 (Issues 1-2), Pages 36-51

[2] R. Amukti, "Identifikasi Kerentanan Longsor Daerah Pangalengan Dengan Metode Slope Morphology," 2017. [Online]. Available: http://journal2.um.ac.id/index.php/jpse

[3] C Damayanti and Sismanto, 2021," Analysis of potential soil fracture based on ground shear strain values in Solok, West Sumatra," IOP Conf. Ser.: Earth Environ. Sci. 789 012058

[4] I. N. Risa, M. Maison, and I. K. Dewi, "Analisis Kerentanan Tanah Berdasarkan Pengukuran Mikrotremo di Desa Jati Mulyo, Tanjung Jabung Timur," *JGE (Jurnal Geofisika Eksplorasi)*, vol. 9, no. 1, pp. 18–31, Mar. 2023, doi: 10.23960/jge.v9i1.236.

[5] Arif Ismul Hadi, Refrizon, M. Farid, Budi Harlianto, and Julia Inti Sari, "Landslide Potential Investigation for Disaster Risk Reduction in Central Bengkulu Regency, Bengkulu Province, Indonesia," Indonesian Journal on Geoscience, Vol. 8 No. 3 December 2021

[6] G. Dal Moro, "On the Identification of Industrial Components in the Horizontal-to-Vertical Spectral Ratio (HVSR) from Microtremors," *Pure Appl Geophys*, vol. 177, no. 8, pp. 3831–3849, Aug. 2020, doi: 10.1007/s00024-020-02424-0.

[7] M. Mucciarelli and M. R. Gallipoli, "A critical review of 10 years of microtremor HVSR technique Project INSIEME (Induced Seismicity in Italy: Estimation, Monitoring, and sEismic risk mitigation)," 2015. [Online]. Available: https://www.researchgate.net/publication/279895512

[8] M. I. Nurwidyanto, M. Zainuri, A. Wirasatrya, and G. Yuliyanto, "Struktur Bawah Permukaan Pantai Semarang berdasarkan Metode HVSR," *Indonesian Journal Of Applied Physics*, vol. 13, no. 1, pp. 117–127, Apr. 2023, doi: 10.13057/ijap.v13i1.66864.

[9] A. S. Zuhri, G. Yuliyanto, and U. Harmoko, "Modeling of 3D Aquifer Layers using Poisson's Ratio Analysis HVSR Method in Tembelang Village, Candimulyo District, Magelang Regency," 2020. [Online]. Available: https://ejournal2.undip.ac.id/index.php/jpa/index

[10] A. Kansa Maimun *et al.*, "Analisis Indeks Kerentanan Seismik, Periode Dominan, Dan Faktor Amplifikasi Menggunakan Metode HVSR di Stage Of Tangerang," 2020.

[11] D. Ikhlas Fadli *et al.*, "Identifikasi Daerah Rawan Longsor Secara Mikrozonasi di Jalan Alternatif Provinsi Menggunakan Metode Simple Additive Weighting (SAW)," *Indonesian Journal of Applied Physics (IJAP)*, vol. 13, no. 1, p. 37, 2023, doi: 10.13057/ijap.v13i1.62110.

[12] Y. Nakamura, "Clear identification of fundamental idea of Nakamura's technique and its applications," 2000. [Online]. Available: https://www.researchgate.net/publication/228603691

[13] Teguh Hariyanto, Filsa Bioresita, Cherie Bhekti Pribadi, Chomia Nilam Safitri "Determination Of Earthquake Intensity Based On PGA (Peak Ground Acceleration) Using Multi-Event Earthquake Data", IOP Conference Series: Earth and Environmental Science, 2021.

[14] W. S. Yuliawati, S. Rasimeng, and K. Karyanto, "Pengolahan Data Mikrotremor Berdasarkan Metode HVSR Dengan Menggunakan Matlab," *JGE (Jurnal Geofisika Eksplorasi)*, vol. 5, no. 1, pp. 45–59, Jan. 2020, doi: 10.23960/jge.v5i1.22.

[15] I. Saraswati Siregar, "Analisis Mikrotremor Dengan Metode HVSR Untuk Mengetahui Zona Penguatan Gempa Bumi di Wilayah Stasiun Seismik Jawa Timur," *Jurnal Inovasi Fisika Indonesia (IFI)*, vol. 06, pp. 33–38, 2017, [Online]. Available: http://202.90.198.100/webdc3/

[16] Wijaya Rendi K dan Nasrul Wahyudi P, "Analisa Potensi Longsor Menggunakan Data Mikrotremor dan Kemiringan di Jalan Raya Puncak Kabupaten Bogor," *Jurnal Widya Climago*, vol. 2, pp. 38–46, May 2020.
[17] A. Widiastari, "Analisa Datamining dengan Metode Klasifikasi C4.5 Sebagai Faktor Penyebab Tanah Longsor," *Journal of Computer System and Informatics (JoSYC)*, vol. 2, no. 3, 2021.
[18] N. Sugianto and M. Farid, "Kondisi Geologi Lokal Kota Bengkulu Berdasarkan Ground Shear Strain (GSS)," *Jurnal Fisika dan Aplikasinya* , vol. 2, pp. 29–36, 2017, doi: 10.21009/SPEKTRA.
[19] Dyah Gofur AGP dan Budi Nugroho Wibowo, "Identifikasi Daerah Longsor Kecamatan Bagelen MenggunakanMetode Mikrotremor," *Wahana Fisika*, vol. 3(2), pp. 102–110, 2018.
[20] Hiroo Kanamori and Emily E Brodsky,(2004) "The physics of earthquakes". *Iop science*, Volume 67, Number 8.

Available online at:
Al-Fiziya: Journal of Materials Science, Geophysics, Instrumentation and Theoretical Physics
Website: http://journal.uinjkt.ac.id/index.php/al-fiziya
Vol.6 No. II 2023, 63-79

Development of Perovskite Manganate-Based Materials as Microwave Absorbers (A Literature Study)

Amanda Haiqal [1], Danang Pamungkas Priambodo[1,*], Fattah Ardhi Faddakiri[1]

[1]Physics Study Program, Faculty of Sciences and Technology, State Islamic University Syarif Hidayatullah Jakarta, Indonesia

*danangpamungkas.priambodo20@mhs.uinjkt.ac.id

Submitted: December; Revised : January ; Approved: March; Available Online: March 2024

Abstract. The 5.0 industrial revolution has led to the rapid development of digital devices and radar detection technology. Electromagnetic (EM) radiation generated by digital devices, such as smartphones, computers, and airplanes, is proven to cause great harm to human health. Manganese perovskite is one material that can produce changes such as its crystal structure, electron transfer, electrical properties, and magnetic properties. Doping applied to manganese perovskite-based materials can induce phenomena such as Colossal Magnetoresistance (CMR) and Magnetocaloric Effect (MCE), giving manganese perovskite-based materials great potential to be used as microwave absorbers. Through this article, the development of various manganese perovskite-based materials as microwave absorbers will be reviewed and summarized. Synthesis methods and microwave absorption mechanisms will also be reviewed. This article focuses on the doping of A-site and B-site manganese perovskite-based materials and their performance in absorbing microwaves. Hopefully, this article can be one of the guidelines for designing new manganese perovskite-based materials, to be applied as microwave absorbers.

Keywords: *Perovskite manganate, microwave absorbers, mechanism, synthesis, doping.*
DOI : 10.15408/fiziya.v6i2.36991

INTRODUCTION

The industrial revolution 5.0 causes the development of digital devices and radar detection technology to develop rapidly. This can make human life more comfortable, however, behind all that there is a concern that can threaten human health [1]. Electromagnetic (EM) radiation generated by digital devices, such as smartphones, computers, and airplanes, has been proven to cause great harm to human health. This radiation can heat up human cells or disrupt the intrinsic EM field of the human body, thus adversely affecting human health [2].

Therefore, developing various materials as microwave absorbers is very important. The main indicators that a material can be used as a good microwave absorber are high reflection loss (R_L), thin thickness, wide bandwidth, and low density. Some of these properties must be possessed by a material so that it has the potential to absorb most microwaves and can be used practically in many fields. These properties can be achieved by develop the size, shape, internal structure, composition, and synthesis method [2].

Recently, many materials have been designed as microwave absorbers in various types of materials, such as nanometer-scale materials, ferrites, conductive polymers, polycrystalline iron fibers and crystalline materials [3]. In general, microwave absorbing materials can be classified into magnetic type and dielectric type according to the loss mechanism. Among these absorbers, perovskite oxides have attracted wide attention among researchers due to their unique crystal structure and mixed ionic electronic conductivity, especially in manganate-based perovskite oxides [4].

Manganate perovskite is one of the materials that can produce changes in physical phenomena in a material, such as changes in crystal structure, electron transfer, electrical properties, and magnetic properties [5]. Manganate perovskite has the general formula $RE_{1-x}A_xMnO_3$, where RE is a rare earth metal ion (La^{3+}, Nd^{3+}, Pr^{3+}) and A is a divalent ion (Sr^{2+}, Ba^{2+}, Ca^{2+}). Doping applied to manganate perovskite-based materials can cause various interesting phenomena such as Colossal Magnetoresistance (CMR) and Magnetocaloric Effect (MCE). The presence of these phenomena makes manganese perovskite-based materials have great potential to be used as microwave absorbers [6].

Many researchers have reported the results of designing manganese perovskite-based materials as microwave absorbers. Based on this, it is necessary to review and summarize these research results. In this article, the mechanism of microwave absorption will be reviewed, then continued with a summary and review of the development of manganese perovskite-based material engineering as a microwave absorber starts from the synthesis method to doping on the material. Hopefully, this article can be one of the guidelines for designing new manganese perovskite-based materials, to be applied as microwave absorbers.

MICROWAVE ABSORPTION MECHANISM

According to the microwave absorption theory, the incident microwave can be divided into three parts when the incident wave hits the absorbing material, namely reflection, absorption, and transmission [2]. When the wave comes to the absorbing material, there are three possibilities: the wave can be absorbed by the material (absorption), reflected (reflection), or transmitted (transmission). In this case, the entire wave is completely absorbed by the microwave absorbing material, and nothing is transmitted. To find out what percentage of the wave is absorbed by the microwave absorbing material, we can calculate the reflection loss (R_L). This reflection loss value will reflect the material's ability to absorb microwave energy [7], [8].

Microwave absorption is characterized by its two main electromagnetic properties. Dielectric loss is the first property and magnetic loss is the second property [9]. Dielectric Loss represents the electronic characteristics between the Electric field of electromagnetic radiation resulting in reflection loss. While magnetic loss represents the characteristics of the magnetic interaction between the material and its electromagnetic waves [10].

The ability of microwave absorbing materials to absorb microwave energy can be determined by calculating the amount of reflection loss (R_L). This value will describe the material's ability to absorb energy [7], [8]. The smaller the RL value, the greater the percentage of waves absorbed by the material. Based on theory, reflection loss can be defined by Eq. 1 and Eq. 2:

$$R_L(dB) = 20 \log \left| \frac{Z_{in} - Z_0}{Z_{in} + Z_0} \right| \quad (1)$$

$$Z_{in} = \left(\frac{\mu_r}{\varepsilon_r}\right)^{\frac{1}{2}} \tanh \left[j \left(\frac{2\pi f d}{c}\right) (\mu_r \varepsilon_r)^{\frac{1}{2}} \right] \quad (2)$$

where Z_{in} is the impedance of the absorber material, Z_0 is the impedance of electromagnetic waves in air, μ_r is the relative permeability of the material, ε_r is the relative permittivity of the material, f is the frequency, c is the speed of light, and d is the thickness of the absorption field of the material [1].

The parameters ε_r and μ_r are expressed in the equations below by considering the real and imaginary components of permittivity $(\varepsilon', \varepsilon'')$ and real and imaginary permeability (μ', μ'').

$$\varepsilon_r = \varepsilon' + j\varepsilon" \quad (3)$$

$$\mu_r = \mu' + j\mu" \quad (4)$$

The real part of the permittivity (ε') indicates the ability of the material to store electrical energy, while the imaginary part (ε'') indicates the ability of the material to release electrical energy. The same principle also applies to permeability, the real part of the permeability (μ') states the ability of the material to store magnetic fields, while the imaginary part (μ'') states the ability of the material to absorb magnetic fields [11]. The results of microwave absorption on manganese perovskite can vary, this is because the structure, doping, composition, and synthesis methods used in each material differ from one another. Discussion of the structure, doping, composition, synthesis method, and microwave absorption properties of some of the research results that have been reported, are exposed after this.

SYNTHESIS METHOD

As mentioned before, the synthesis method is one way to develop manganese perovskite-based materials for microwave absorbers. The synthesis method determines the physicochemical properties of the material. This will affect the material's ability to absorb microwaves. Some methods that are commonly used to synthesize manganate perovskite-based materials are solid reaction method, sol-gel method, and co-precipitation method [4].

Solid-State Reaction Method

The solid reaction method is a conventional method to synthesize manganate perovskite-based materials, the process of this method is fairly simple. In general, the main compounds of the related elements (especially oxide-based ones) are weighed

Vol.6 No. II 2023, 61-77
P-ISSN: 2621-0215, E-ISSN: 2621-489X

according to the stoichiometric ratio. Then the alloy of the related compounds will be calcined at high temperature after mixing, mixing is usually assisted by high-energy ball milling. The advantage of this method is that there are no impurity phases and the doping characteristics are easy to control. The disadvantage of this method is that it is difficult to obtain a single phase. This will result in grain size that does not match the specific surface area and inadequate absorption strength. The high energy consumption factor and long reaction time are also disadvantages of this method [4].

S. Saptari et al [12]–[14] synthesized the materials $La_{0.67}Ba_{0.33}Mn_{1-x}Ni_xO_3$ (x = 0; 0.02; 0.04; 0.06), $La_{0.67}Ba_{0.33}Mn_{1-x}Ti_xO_3$ (x = 0; 0.02; 0.04; 0.06), and $La_{0.67}Ba_{0.33}Mn_{1-y}Ni_{y/2}Ti_{y/2}O_3$ (y = 0.02; 0.04; 0.06) using the solid recitation method. In $La_{0.67}Ba_{0.33}Mn_{1-x}Ni_xO_3$ (x = 0; 0.02; 0.04; 0.06), the constituent compounds were mixed according to the stoichiometric ratio for 25 hours, then calcined at 800℃ for 10 hours, and sintered at 1200℃ for 2 hours. The results show that for the price of x = 0-0.04 the sample has a single phase with a monoclinic crystal structure and space group I 1 2/c 1, while for the value of x = 0.06 the sample has a dual phase, namely $La_{0.67}Ba_{0.33}Mn_{1-x}Ni_xO3$ with a monoclinic crystal structure and $BaMnO_3$ with a hexagonal crystal structure. The XRD pattern of $La_{0.67}Ba_{0.33}Mn_{1-x}Ni_xO_3$ (x = 0; 0.02; 0.04; 0.06) sample can be seen in Figure 1.

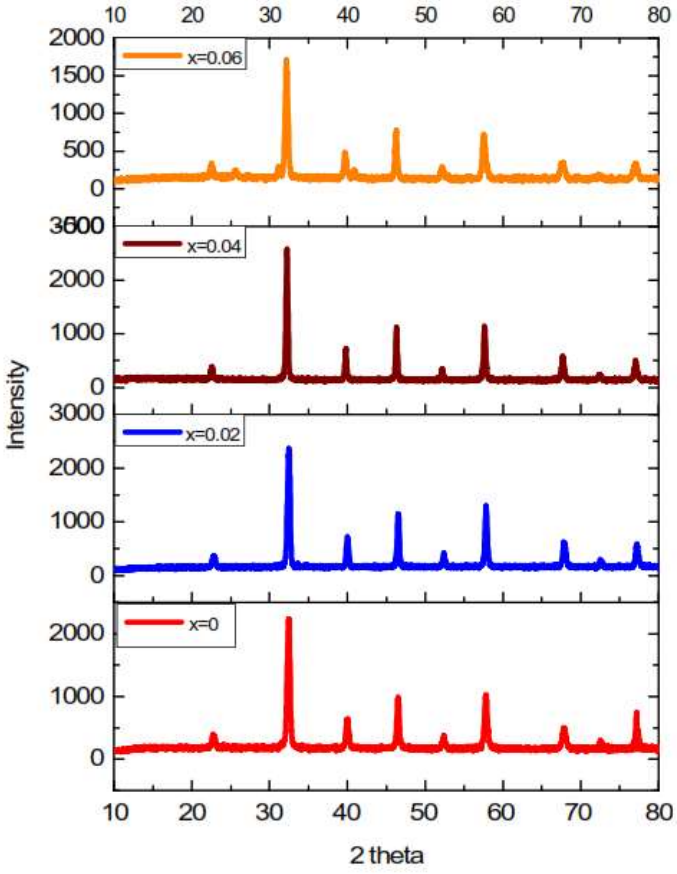

Figure 1 XRD pattern of $La_{0.67}Ba_{0.33}Mn_{1-x}Ni_xO_3$ sample [12].

In $La_{0.67}Ba_{0.33}Mn_{1-x}Ti_xO_3$ material (x = 0; 0.02; 0.04; 0.06), the constituent compounds were mixed according to the stoichiometric ratio for 25 hours using Planetary Ball Milling with a fixed powder/ball ratio of 1:10. The samples were then calcined at 800℃ for 10 hours and sintered at 1200℃ for 2 hours. The results show that the samples have a single

Vol.6 No. II 2023, 61-77
P-ISSN: 2621-0215, E-ISSN: 2621-489X

phase without any impurities for all x values with monoclinic crystal structure and space group I 1 2/c 1. The XRD pattern of $La_{0.67}Ba_{0.33}Mn_{1-x}Ti_xO_3$ sample (x = 0; 0.02; 0.04; 0.06) can be seen in Figure 2.

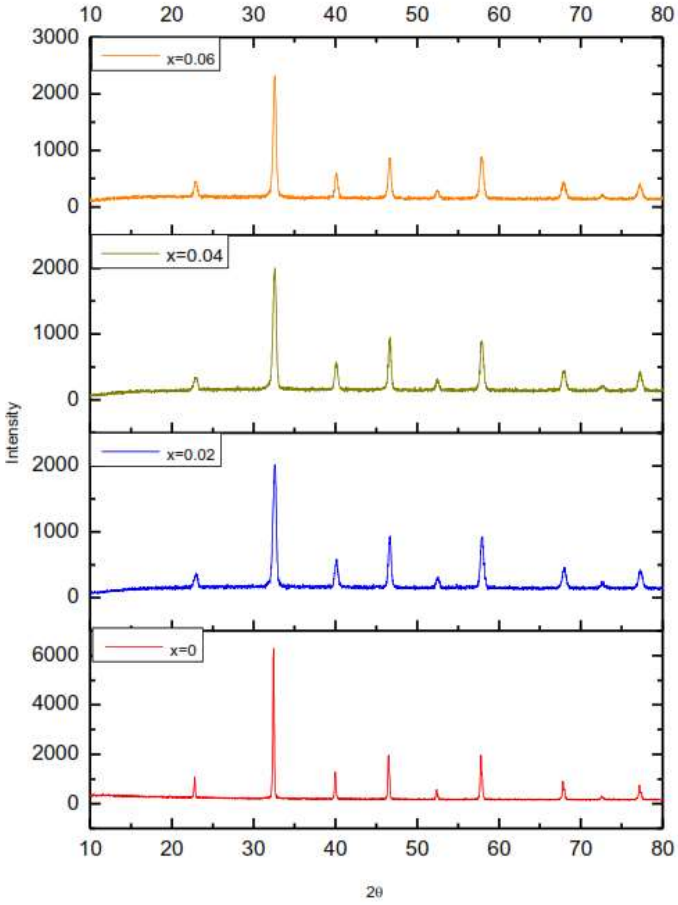

Figure 2 XRD pattern of $La_{0.67}Ba_{0.33}Mn_{1-x}Ti_xO_3$ sample [13].

In $La_{0.67}Ba_{0.33}Mn_{1-y}Ni_{y/2}Ti_{y/2}O_3$ (y = 0.02; 0.04; 0.06), the constituent compounds were mixed according to the stoichiometric ratio for 40 hours using planetary ball milling. The samples were then calcined at 900℃ for 10 hours and sintered at 1200℃ for 10 hours. The results show that the sample has a single phase without any impurities for all x values with monoclinic crystal structure and space group I 1 2/c 1. The XRD pattern of $La_{0.67}Ba_{0.33}Mn_{1-y}Ni_{y/2}Ti_{y/2}O_3$ (y = 0.02; 0.04; 0.06) sample can be seen in Figure 3.

Vol.6 No. II 2023, 61-77
P-ISSN: 2621-0215, E-ISSN: 2621-489X

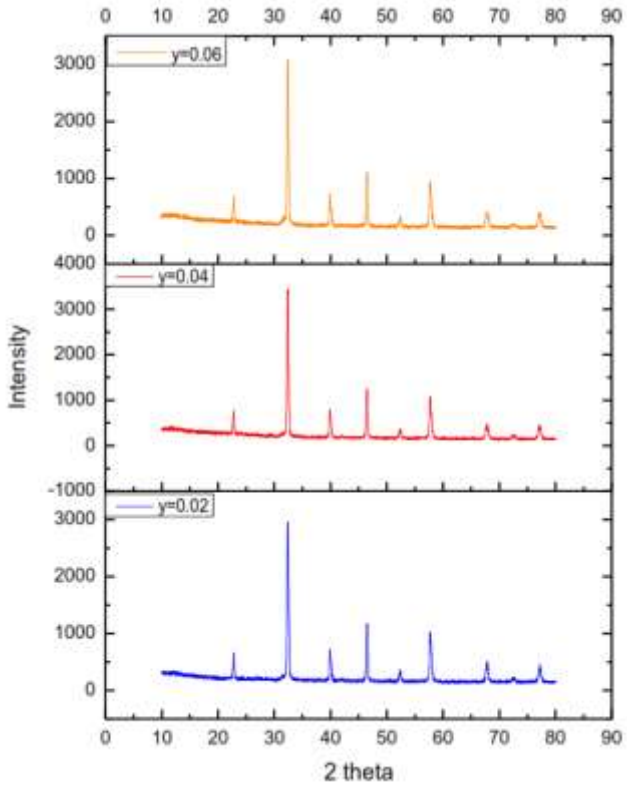

Figure 3 XRD pattern of $La_{0.67}Ba_{0.33}Mn_{1-y}Ni_{y/2}Ti_{y/2}O_3$ sample [14].

S. Zhang et al [15] also synthesized $La_{0.7}Sr_{0.3}MnO_3$ material using the solid reaction method with variations in sintering temperature. The samples were sintered in the temperature range of 900℃-1150℃ with an increase of 50℃ in each sample. The results show that at 900℃ and 950℃ the perovskite phase has not yet formed. The perovskite phase began to form at 1000℃. The XRD pattern of $La_{0.7}Sr_{0.3}MnO_3$ sample can be seen in Figure 4.

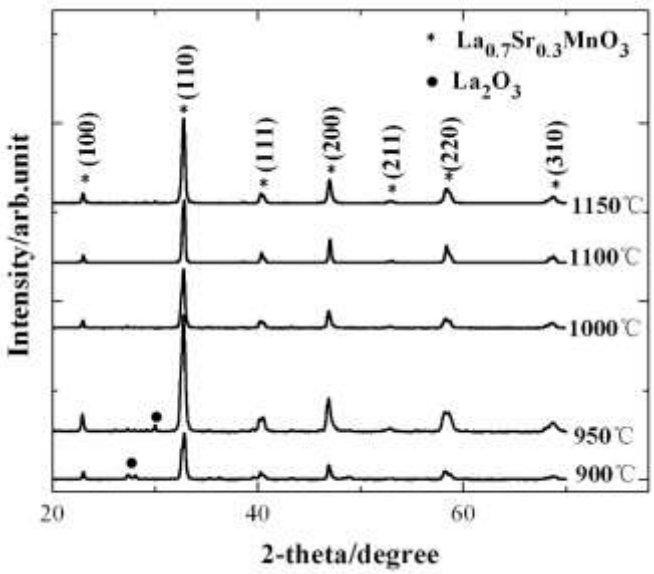

Figure 4 XRD pattern of $La_{0.7}Sr_{0.3}MnO_3$ sample [15].

Vol.6 No. II 2023, 61-77
P-ISSN: 2621-0215, E-ISSN: 2621-489X

Sol-Gel Method

The sol-gel method is one of the most frequently used methods to synthesize manganese perovskite-based materials. In this method, "sol" is first formed by hydrolysis or alcoholization of metal compounds or inorganic metal salts. Afterwards, a "gel" will be obtained through a polycondensation process. The "gel" forming compounds used in this method include citric acid, ethanol, ammonia, polyvinyl acrylate (PVA). This method is often referred to as the citric acid method, as citric acid is commonly used as a ligand in this method. The structure, chemical properties, and particle size of the sample can be adjusted by controlling the sintering temperature. Products produced from this method usually have high purity and uniform particle distribution [4].

J. W. Liu et al [16] synthesized $La_{1-x}Ca_xMnO_3$ (x = 0 - 0.5) material using sol-gel method. All precusors were mixed according to stoichiometric calculations. After forming the gel, the sample was calcined at 800 ℃ for 2 hours. The results show that the sample has a single phase with a perovskite structure. The XRD pattern of $La_{1-x}Ca_xMnO_3$ sample can be seen in Figure 5.

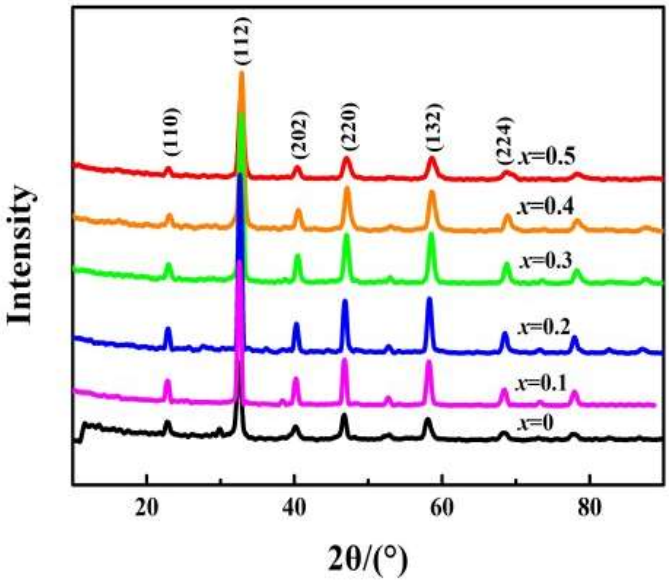

Figure 5 XRD pattern of $La_{1-x}Ca_xMnO_3$ sample [16].

F. Rizky et al [17] synthesized $La_{0.7}Ca_{0.3}Mn_{1-x}Ti_xO_3$ (x = 0; 0.1; 0.2; 0.3) material using sol-gel method. All precursors were mixed according to stoichiometric calculations. After gel formation, the samples were calcined at 600℃ for 6 hours and sintered at 1000℃ for 12 hours. The results show that all samples have a single phase without any impurities. The XRD pattern of $La_{0.7}Ca_{0.3}Mn_{1-x}Ti_xO_3$ sample can be seen in Figure 6.

Vol.6 No. II 2023, 61-77
P-ISSN: 2621-0215, E-ISSN: 2621-489X

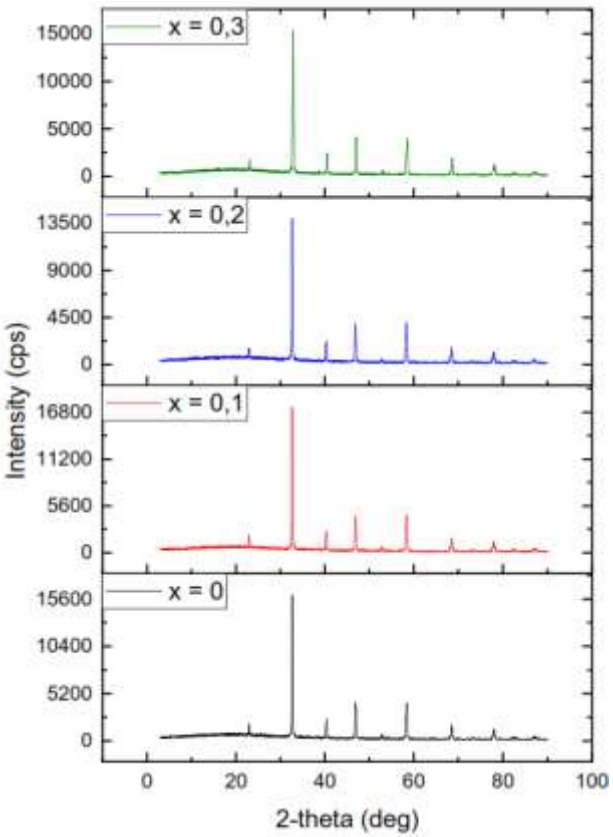

Figure 6 XRD pattern of $La_{0.7}Ca_{0.3}Mn_{1-x}Ti_xO_3$ sample [17].

N. H. Latifah et al [18] synthesized $La_{0.7}Sr_{0.3}Mn_{1-x}(Ni,Ti)_{x/2}O_3$ (x = 0.1; 0.3; 0.5) material using sol-gel method. All precursors were mixed according to the stoichiometric calculation. After gel formation, the samples were calcined at 600℃ for 6 hours and sintered at 1000℃ for 12 hours. The results show that all samples have a single phase without any impurities. The XRD pattern of $La_{0.7}Sr_{0.3}Mn_{1-x}(Ni,Ti)_{x/2}O_3$ sample can be seen in Figure 7.

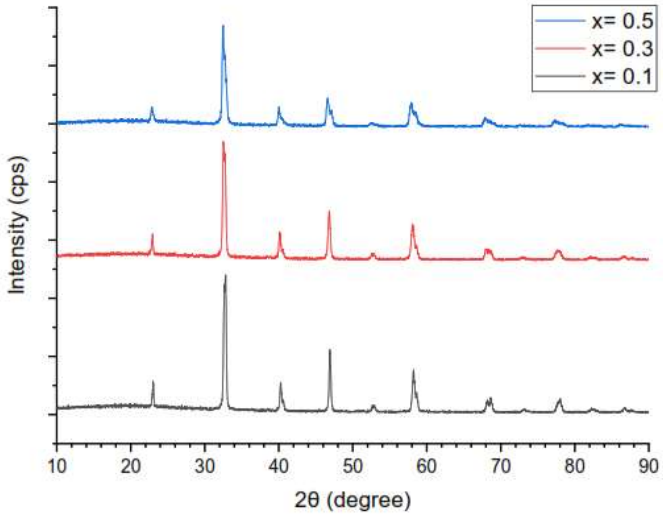

Figure 7 XRD pattern of $La_{0.7}Sr_{0.3}Mn_{1-x}(Ni,Ti)_{x/2}O_3$ sample [18].

Vol.6 No. II 2023, 61-77
P-ISSN: 2621-0215, E-ISSN: 2621-489X

Copreticipation Method

In general, the coprecipitation method begins by mixing salt solutions of two or more metals used according to a pre-calculated stoichiometric ratio, the solution is then filtered to obtain the precipitate. Then the precipitate is washed and calcined to obtain the desired perovskite phase. Alkaline earth metals are one of the most commonly used precipitants in synthesizing manganate perovskite-based materials. The advantage of this method lies in the short synthesis cycle. The disadvantage of this method is that the resulting sample is easily agglomerated due to high local concentration when the resulting precipitate is not uniform, this can affect the uniformity of particle size. To overcome these problems, dispersion technology needs to be used to ensure the uniformity of the samples produced from the precursors used, such as ultrasound, microwave, and freeze drying [4].

F. Jiang et al [19] synthesized $La_{0.1}Ca_{0.9}MnO_3$ and $CaMnO_3$ materials using the coprecipitation method. All precursors were mixed according to stoichiometric calculations in solution form. The samples were then dried at 70℃ in a thermoelectric thermostat drying box, then the samples were calcined at 950℃ for 3 hours. The XRD test results show that the samples have a single phase, $La_{0.1}Ca_{0.9}MnO_3$ and $CaMnO_3$, respectively.

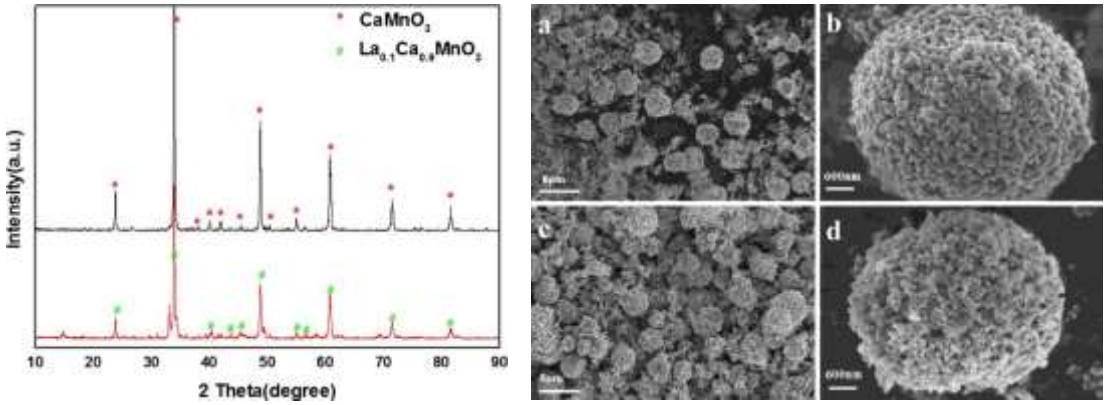

Figure 8 XRD pattern and morphology of $La_{0.1}Ca_{0.9}MnO_3$ and $CaMnO_3$ sample [19].

While the SEM results show that the particles have an irregular granular shape with a size of about 200 nm and a grain size of 4-6 μm.The XRD pattern and morphology of the samples can be seen in Figure 8 and Figure 9.

DEVELOPMENT OF MANGANESE PEROVSKITE AS MICROWAVE ABSORBER

The unique chemical and physical properties of manganese perovskite-based materials such as insulator-metal phase switching that are strongly related to temperature, it causes a phenomenon called the Giant Magnetoresistance Effect. The presence of this phenomenon attracts wide attention in the application of manganese perovskite-based materials as microwave absorbers [4].

Unmodified manganate perovskite-based materials have a weak absorption ability to microwaves, which is related to the limited dielectric, conductive, and magnetic properties that are not suitable. Ions on the A site and B site on manganate perovskite can be substituted with other metal elements. The doping of these ions can change the

Vol.6 No. II 2023, 61-77
P-ISSN: 2621-0215, E-ISSN: 2621-489X

physicochemical properties of a manganate perovskite and cause distortions in the crystal lattice (Jahn-teller effect). Manganate perovskite-based materials are known to have ferromagnetic properties, therefore, doping is generally carried out using metals that have semiconductor conductivity values or conducive metals. As a result, the crystal structure will change from lower to higher symmetry and change the electric dipole moment thus increasing the dielectric loss value [20], [21].

Develop by simply doping ions on the A site and B site is widely researched because it can affect the crystalline degree directly and the Jahn-teller effect occurs, engineering with this formation produces manganate perovskite-based materials that have the ability to absorb microwaves [1], [4]. S. Zhang et al [15] performed Sr^{2+} ion doping on $LaMnO_3$ material into $La_{0.7}Sr_{0.3}MnO_3$ with a sintering temperature variation of 900℃ - 1150℃ to see its absorption performance against microwaves. The results show that $La_{0.7}Sr_{0.3}MnO_3$ material sintered at 1000℃ and 1100℃ has the best absorption performance with values of -10.71 dB at 9.96 GHz and -17.46 dB at 15.87 GHz, respectively. There is a decrease in the absorption value when the sample is sintered at 1150 ℃ to -9.01 dB at a frequency of 12.51 GHz. It can be seen that as the sintering temperature increases, the absorption peak shifts to higher frequencies, then shifts to lower frequencies.

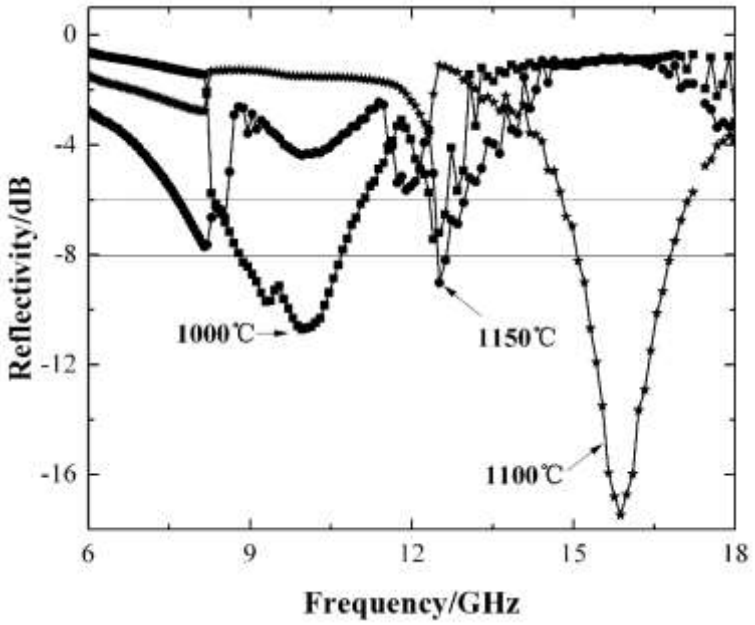

Figure 9 Reflectivity of x with different sintered temperature [15].

The effect of Ba2+ ion doping on the microwave absorption ability of $La_{1-x}Ba_xMnO_3$ (x = 0.1; 0.2; 0.3; 0.4; 0.5) material in nanoparticle form was reported by J. Deng [22]. The results show that the x = 0.2 and 0.3 prices have the best absorption performance with values of -21 dB at 8.4 GHz and -21.4 dB at 7.7 GHz, respectively. It can be seen that the composition of Ba2+ ions can affect the absorption performance of $La_{1-x}Ba_xMnO_3$ material towards microwaves.

Vol.6 No. II 2023, 61-77
P-ISSN: 2621-0215, E-ISSN: 2621-489X

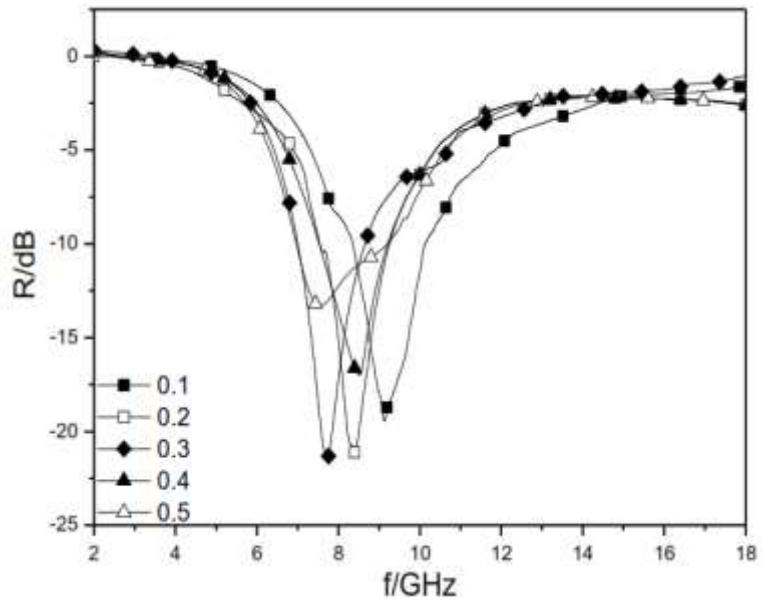

Figure 10 Reflectivity curve $La_{1-x}Ba_xMnO_3$ with different Ba composition [22].

J. W. Liu et al [16] studied the effect of Ca^{2+} ion doping on $La_{1-x}Ca_xMnO_3$ material (x = 0 - 0.5) to see its microwave absorption ability. The sample is made with a thickness of 2 mm, the results show that for the value of x = 0.1 has the largest absorption capability of -42 dB at a frequency of 10.5 GHz with a bandwidth of 3.5 GHz.

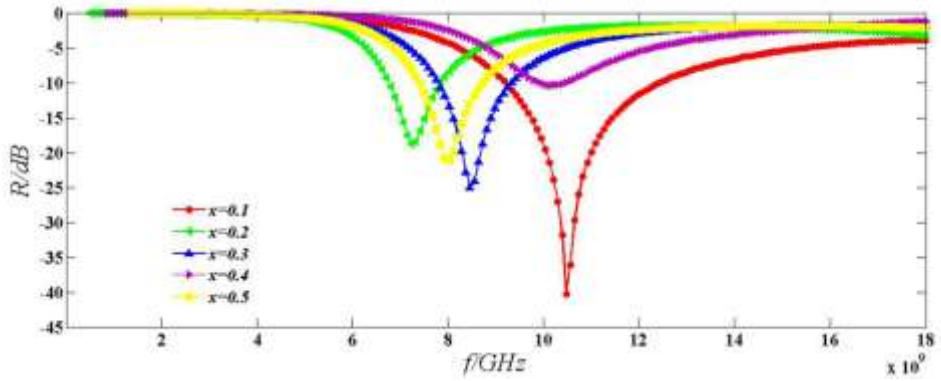

Figure 11 Reflectivity curves of the samples with different doping concentration x (2mm) [16].

F. Jiang et al [19] also studied the microwave absorption performance of $La_{0.1}Ca_{0.9}MnO_3$ and $CaMnO_3$ materials. The samples were made with a thickness of 6 mm. The results show that the $CaMnO_3$ sample has an RL value of -10 dB at 5 GHz and -15 dB at 16.6 GHz. While the $La_{0.1}Ca_{0.9}MnO_3$ sample has the largest RL value of -31 dB at a frequency of 11.5 GHz.

Vol.6 No. II 2023, 61-77
P-ISSN: 2621-0215, E-ISSN: 2621-489X

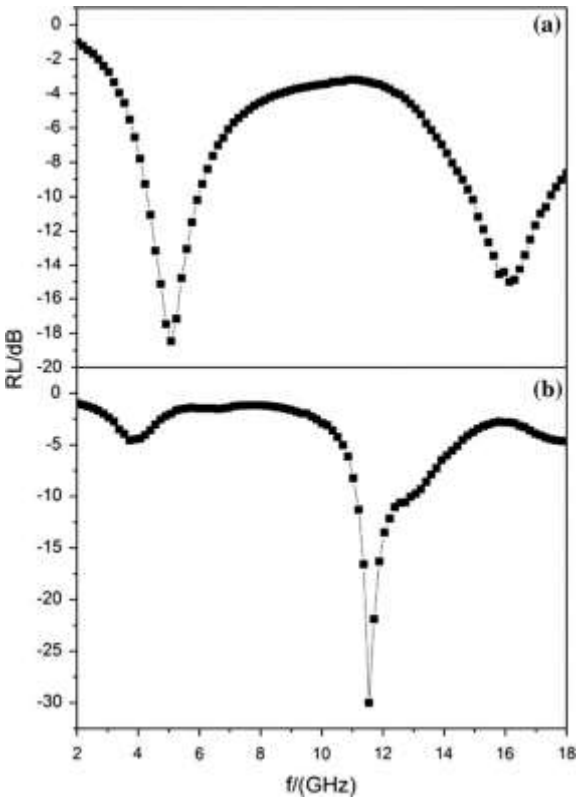

Figure 12 Frequency dependence of reflection loss (RL) for (a) $CaMnO_3$ sample and (b) $La_{0.1}Ca_{0.9}MnO_3$ sample [19].

R. I. Admi et al [23] studied the effect of two ions (Ca^{2+} and Sr^{2+}) doped on the A site of $La_{0.7}(Ca_{1-x}Sr_x)_{0.3}MnO_3$ material (x = 0; 0.1; 0.2; 0.3) with a thickness of 1.5 mm. The results show a decrease in absorption capability as the x value increases. When x = 0, $La_{0.7}(Ca_{1-x}Sr_x)_{0.3}MnO_3$ material has a maximum absorption value of -3.53 dB at a frequency of 10.44 GHz with an absorption ability of 55.64%.

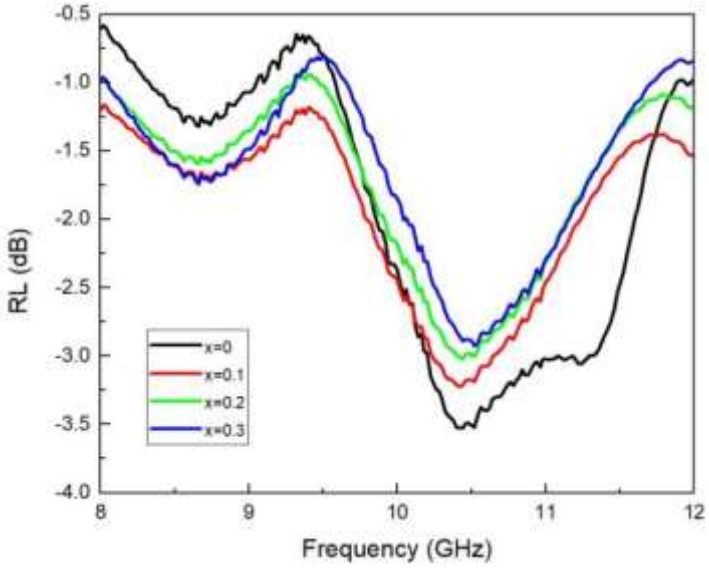

Figure 13 Microwave absorption performance of $La_{0.7}(Ca_{1-x}Sr_x)_{0.3}MnO_3$ [23].

Vol.6 No. II 2023, 61-77
P-ISSN: 2621-0215, E-ISSN: 2621-489X

F. Rizky et al [17] studied the effect of Ti^{3+} doping on the microwave absorption performance of $La_{0.7}Ca_{0.3}Mn_{1-x}Ti_xO_3$ material (x = 0; 0.1; 0.2; 0.3). The results show that the x = 0.3 value has the highest absorption value among other x values. The absorption value for x = 0.3 is -10.07202 dB at a frequency of 10.4 GHz with a material absorption capability of 90.16%.

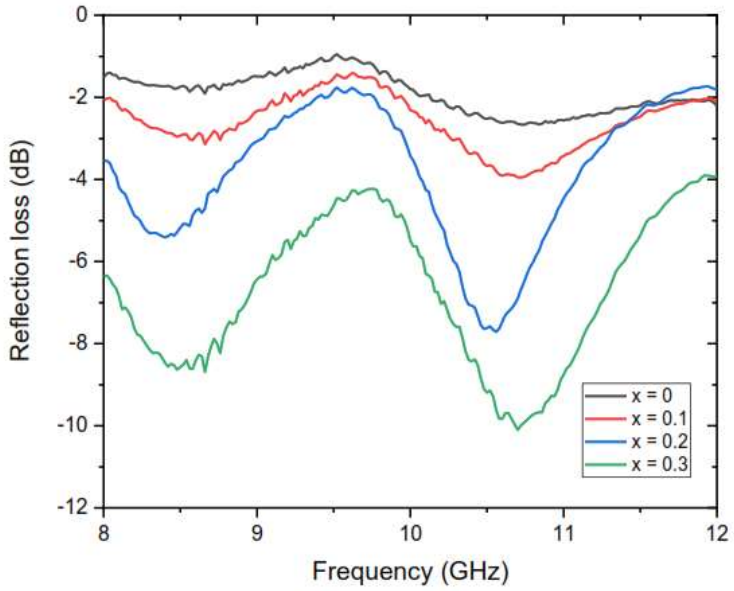

Figure 14 Microwave absorption performance of $La_{0.7}Ca_{0.3}Mn_{1-x}Ti_xO_3$ [17].

S. Saptari et al [12]–[14] studied the effect of Ni^{3+} and Ti^{3+} ion doping on the B site on the microwave absorption performance of $La_{0.67}Ba_{0.33}Mn_{1-x}Ni_xO_3$ (x = 0; 0.02; 0.04; 0.06), $La_{0.67}Ba_{0.33}Mn_{1-x}Ti_xO_3$ (x = 0; 0.02; 0.04; 0.06), and $La_{0.67}Ba_{0.33}Mn_{1-y}Ni_{y/2}Ti_{y/2}O_3$ (y = 0.02; 0.04; 0.06). The largest R_L value of the $La_{0.67}Ba_{0.33}Mn_{1-x}Ni_xO_3$ (x = 0; 0.02; 0.04; 0.06) material is when x = 0.04 at -8.85 dB at a frequency of 11.58 GHz. The largest R_L value of the material $La_{0.67}Ba_{0.33}Mn_{1-x}Ti_xO_3$ (x = 0; 0.02; 0.04; 0.06) is owned when x = 0.02 amounting to -13.26 dB at a frequency of 11.46 GHz. While the largest R_L value in $La_{0.67}Ba_{0.33}Mn_{1-y}Ni_{y/2}Ti_{y/2}O_3$ (y = 0.02; 0.04; 0.06) material is owned when the value of y = 0.06 amounting to -14.30 dB at a frequency of 11.28 GHz.

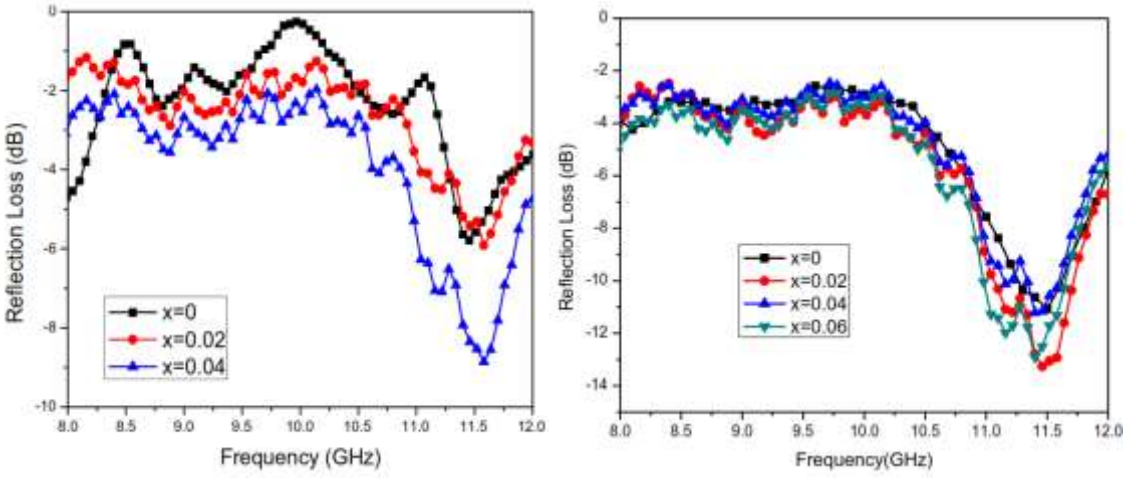

(a) (b)

Vol.6 No. II 2023, 61-77
P-ISSN: 2621-0215, E-ISSN: 2621-489X

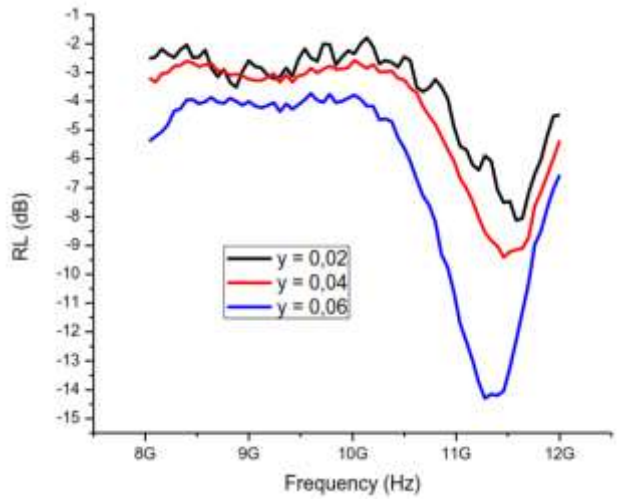

(c)

Figure 15 Reflection loss spectra of (a) $La_{0.67}Ba_{0.33}Mn_{1-x}Ni_xO_3$, (b) $La_{0.67}Ba_{0.33}Mn_{1-x}Ti_xO_3$, and (c) $La_{0.67}Ba_{0.33}Mn_{1-y}Ni_{y/2}Ti_{y/2}O_3$ sample [12]–[14].

N. H. Latifah et al [18] also studied the effect of doping Ni^{3+} and Ti^{3+} ions on the B site on the microwave absorption performance of $La_{0.7}Sr_{0.3}Mn_{1-x}(Ni,Ti)_{x/2}O_3$ material (x = 0.1; 0.3; 0.5). The results show that $La_{0.7}Sr_{0.3}Mn_{1-x}(Ni,Ti)_{x/2}O_3$ material has a maximum absorption value of -11.8 dB at a frequency of 10.58 GHz when x = 0.5, with an absorption capability of 93.39%.

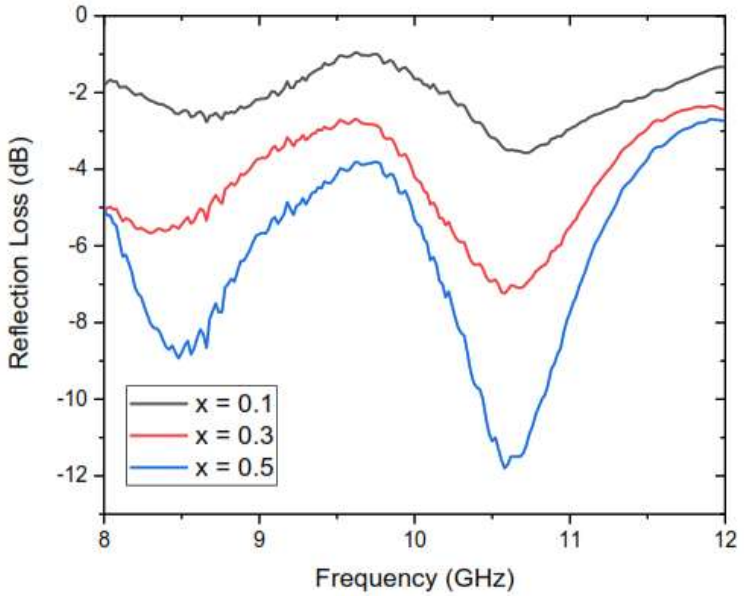

Figure 16 The absorption curve of electromagnetic waves on the material $La_{0.7}Sr_{0.3}Mn_{1-x}(Ni,Ti)_{x/2}O_3$ [18].

F. A. Kurniawan et al [24] also studied the effect of Fe and Ti ion doping on the B site on the microwave absorption performance of $Nd_{0.6}Sr_{0.4}Mn_xFe_{1/2(1-x)}Ti_{1/2(1-x)}O_3$ material (x = 0; 0.1; 0.2). The results show that when x = 0.2, the $Nd_{0.6}Sr_{0.4}Mn_xFe_{1/2(1-x)}Ti_{1/2(1-x)}O_3$

material has a maximum absorption value of -17.5 dB at a frequency of 9.5 GHz with a material absorption capability of 98.22%.

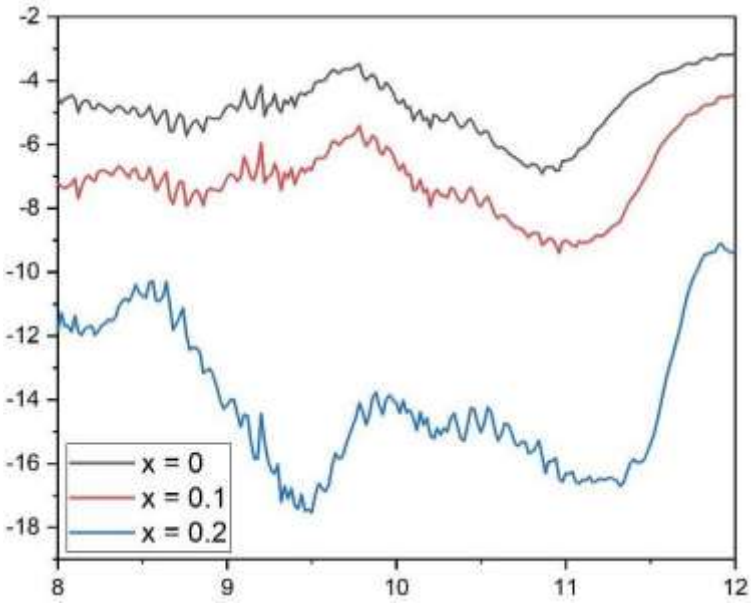

Figure 17 Electromagnetic wave absorption curve on $Nd_{0.6}Sr_{0.4}Mn_xFe_{1/2(1-x)}Ti_{1/2(1-x)}O_3$ material [24].

Through the various research results that have been presented, it can be seen that manganese perovskite-based materials doped in A site and B site have better absorption capabilities when compared to manganese perovskite-based materials doped only in A site. The ability to absorb microwaves is caused by several factors such as double exchange interaction, permeability, and permittivity of the material [16], [17]. Table 1 summarizes the maximum absorption capability of manganese perovskite-based materials.

Table 1 summarizes the maximum absorption capability of manganese perovskite-based materials.

Materials	RL max (dB)	Frequency (GHz)	References
$La_{0.7}Sr_{0.3}MnO_3$	-17.46	15.87	[15]
$La_{0.7}Ba_{0.3}MnO_3$	-21.40	7.70	[22]
$La_{0.9}Ca_{0.1}MnO_3$	-42.00	10.50	[16]
$La_{0.1}Ca_{0.9}MnO_3$	-31.00	11.50	[19]
$La_{0.7}Ca_{0.3}MnO_3$	-3.53	10.44	[23]
$La_{0.7}Ca_{0.3}Mn_{0.7}Ti_{0.3}O_3$	-10.07	10.40	[17]
$La_{0.67}Ba_{0.33}Mn_{0.96}Ni_{0.04}O_3$	-8.85	11.58	[12]
$La_{0.67}Ba_{0.33}Mn_{0.98}Ti_{0.02}O_3$	-13.26	11.46	[13]
$La_{0.67}Ba_{0.33}Mn_{0.94}Ni_{0.03}Ti_{0.03}O_3$	-14.30	11.28	[14]
$La_{0.7}Sr_{0.3}Mn_{0.5}Ni_{0.25}Ti_{0.25}O_3$	-11.80	10.58	[18]
$Nd_{0.6}Sr_{0.4}Mn_{0.2}Fe_{0.4}Ti_{0.4}O_3$	-17.50	9.50	[24]

CONCLUSIONS

Manganate perovskite-based materials have enormous potential as microwave absorbers because they have unique crystal structures and are easily engineered by doping. Based on the reviews discussed earlier, commonly used methods to synthesize manganate perovskite materials have been described. There are advantages and disadvantages to each method. The method that needs to be considered to synthesize manganate perovskite-based materials is the sol-gel method. Through this method the particle size and distribution can be controlled by selecting the calcination and sintering temperatures. There are differences in microwave absorption performance between one material and another, this is influenced by the doping carried out on each site. In this regard, it can be seen that the microwave absorption performance of manganate perovskite-based materials is not high enough. So there are still opportunities for further development of manganate perovskite-based materials as microwave absorbers.

REFERENCES

[1] M. F. Elmahaishi, R. S. Azis, I. Ismail, and F. D. Muhammad, "A review on electromagnetic microwave absorption properties: their materials and performance," Journal of Materials Research and Technology, vol. 20, pp. 2188–2220, Sep. 2022, doi: 10.1016/J.JMRT.2022.07.140.

[2] X. Zeng, X. Cheng, R. Yu, and G. D. Stucky, "Electromagnetic microwave absorption theory and recent achievements in microwave absorbers," Carbon, vol. 168. Elsevier Ltd, pp. 606–623, Oct. 30, 2020. doi: 10.1016/j.carbon.2020.07.028.

[3] S. Zhang et al., "Two-dimensional nanomaterials for high-efficiency electromagnetic wave absorption: An overview of recent advances and prospects," J Alloys Compd, vol. 893, p. 162343, Feb. 2022, doi: 10.1016/J.JALLCOM.2021.162343.

[4] S. Zhang, Z. Jia, B. Cheng, Z. Zhao, F. Lu, and G. Wu, "Recent progress of perovskite oxides and their hybrids for electromagnetic wave absorption: a mini-review," Adv Compos Hybrid Mater, vol. 5, no. 3, pp. 2440–2460, Sep. 2022, doi: 10.1007/s42114-022-00458-7.

[5] M. U. Faruqi, A. Tjahjono, and S. A. Saptari, "Analisis Struktur Kristal dan Sifat Kemagnetan Material Komposit Perovskite Manganit Nd0,6Sr0,4MnO3/ZnO," Al-Fiziya: Journal of Materials Science, Geophysics, Instrumentation and Theoretical Physics, vol. 3, no. 1, pp. 1–8, Aug. 2020, doi: 10.15408/fiziya.v3i1.16158.

[6] M. Al-Rabi, A. Tjahjono, and S. A. Saptari, "Analisis Fasa, Struktur Kristal dan Sifat Kemagnetan Material Komposit Berbasis Nd0,6Sr0,4MnO3/Fe2O3," Al-Fiziya: Journal of Materials Science, Geophysics, Instrumentation and Theoretical Physics, vol. 3, no. 2, pp. 114–122, Dec. 2020, doi: 10.15408/fiziya.v3i2.17638.

[7] S. Wardiyati, W. Ari Adi, dan Didin Sahidin Winatapura Pusat Sains dan Teknologi Bahan Maju, K. Puspiptek, and T. selatan, "Sintesis dan Karakterisasi Microwave Absorbing Material Berbasis Ni-SiO2 dengan Metode Sol-Gel," 2018.

[8] Y. E. Gunanto, E. Jobiliong, and W. A. Adi, "Microwave absorbing properties of Ba0.6Sr0.4Fe12-zMnzO19 (z = 0 - 3) materials in X-Band frequencies," Journal of Mathematical and Fundamental Sciences, vol. 48, no. 1, pp. 55–65, 2016, doi: 10.5614/j.math.fund.sci.2016.48.1.6.

[9] S. S. Pinto and M. C. Rezende, "Performance prediction of microwave absorbers based on POMA/carbon black composites in the frequency range of 8.2 to 20 GHz," Journal of Aerospace Technology and Management, vol. 10, 2018, doi: 10.5028/jatm.v10.764.

[10] S. O. Nelson, "Dielectric properties measurement techniques and applications," Transactions of the American Society of Agricultural Engineers, vol. 42, no. 2, pp. 523–529, 1999, doi: 10.13031/2013.13385.

[11] Y. Taryana, A. Manaf, N. Sudrajat, and Y. Wahyu, "Material Penyerap Gelombang Elektromagnetik Jangkauan Frekuensi Radar," Jurnal Keramik dan Gelas Indonesia, vol. 28, no. 1, pp. 1–29, 2019.

[12] S. Saptari, A. Manaf, and B. Kurniawan, "Microwave Absorbing Properties of La0.67Ba0.33Mn1-xNixO3," Jurnal Sains Materi Indonesia, vol. 15, no. 4, pp. 183–186, Jul. 2012, [Online]. Available: http://jusami.batan.go.id

[13] S. A. Saptari, A. Manaf, and B. Kurniawan, "Microwave Absorbing Properties of La0.67Ba0.33Mn1-xTixO3 in The Frequency Range 8-12 GHz," International Journal of Basic & Applied Sciences IJBAS-IJENS, vol. 14, no. 03, pp. 1410403–5959, 2014.

[14] S. Ahmiatri Saptari, A. Manaf, and B. Kurniawan, "THE MICROWAVE ABSORPTION PROPERTIES OF La0.67Ba0.33Mn1-yNiy/2Tiy/2O3 IN THE FREQUENCY RANGE 8-12 GHz," 2013.

[15] S. Zhang and Q. Cao, "Microwave absorption performance of La0.7Sr0.3MnO3 with different sintering temperatures," in Advanced Materials Research, 2012, pp. 1399–1402. doi: 10.4028/www.scientific.net/AMR.415-417.1399.

[16] J. W. Liu, J. J. Wang, and H. T. Gao, "Infrared emissivities and microwave absorption properties of perovskite La1-xCaxMnO3 (0≤x≤0.5)," Materials Science Forum, vol. 914, pp. 96–101, 2018, doi: 10.4028/www.scientific.net/MSF.914.96.

[17] F. Rizky, S. A. Saptari, A. Tjahjono, and D. S. Khaerudini, "Perovskite Manganit Analysis Based on La0.7Ca0.3Mn1-xTixO3 (x=0, 0.1, 0.2, and 0.3) as Potential Microwave Absorber Material with Sol-Gel Method," Journal of Physics: Theories and Applications, vol. 6, no. 1, p. 17, Mar. 2022, doi: 10.20961/jphystheor-appl.v6i1.59142.

[18] S. A. Saptari, N. H. Lathifah, A. Tjahjono, and D. S. Khaerudini, "Analysis of crystal structure and reflection loss of material based on La0.7Sr0.3Mn1-x(Ni, Ti)x/2O3 (x=0.1, 0.3, and 0.5) applications for microwave absorbers," Journal of Physics: Theories and Applications, vol. 6, no. 2, p. 106, Sep. 2022, doi: 10.20961/jphystheor-appl.v6i2.60178.

[19] F. Jiang, J. Zheng, L. Liang, M. Zhang, and Y. Wang, "Microwave absorbing properties of La0.1Ca0.9MnO3 porous microsphere synthesized by method of precipitation," Journal of Materials Science: Materials in Electronics, vol. 26, no. 4, pp. 2243–2247, Apr. 2015, doi: 10.1007/s10854-015-2676-1.

[20] H. A. Jahn and E. Teller, "Stability of Polyatomic Molecules in Degenerate Electronic States. I. Orbital Degeneracy," Proc R Soc Lond A Math Phys Sci, vol. 161, no. 905, pp. 220–235, 1937, [Online]. Available: http://www.jstor.org/stable/96911

[21] B. Zhao et al., "Poly(vinylidene fluoride)/Cu@Ni Anchored Reduced-Graphene Oxide Composite Films with Folding Movement to Boost Microwave Absorption Properties," ES Energy and Environment, vol. 14, pp. 79–86, Dec. 2021, doi: 10.30919/esee8c488.

[22] J. Deng, "Microwave absorbing properties of La1-xBaxMnO3 (x=0.1,0.2,0.3,0.4,0.5) nano-particles," J Phys Conf Ser, vol. 1777, no. 1, Feb. 2021, doi: 10.1088/1742-6596/1777/1/012032.

[23] R. I. Admi, S. A. Saptari, A. Tjahjono, I. N. Rahman, and W. A. Adi, "Synthesis and characterization microwave absorber properties of La0.7(Ca1-xSrx)0.3MnO3prepared by Sol-Gel method," in Journal of Physics: Conference Series, IOP Publishing Ltd, Mar. 2021. doi: 10.1088/1742-6596/1816/1/012091.

[24] F. A. Kurniawan, S. A. Saptari, A. Tjahjono, and D. S. Khaerudini, "Analysis Perovskite Material Absorber Based on Nd0.6Sr0.4MnxFe1/2(1-x)Ti1/2(1-x)O3 (x = 0, 0.1, 0.2) by Sol-Gel Method," Journal of Physics: Theories and Applications, vol. 6, no. 1, p. 55, Mar. 2022, doi: 10.20961/jphystheor-appl.v6i1.59122.

Available online at:
Al-Fiziya: Journal of Materials Science, Geophysics,
Instrumentation and Theoretical Physics
Website: http://journal.uinjkt.ac.id/index.php/al-fiziya
Vol.6 No. II 2023,80-91

Computational Model of Boride Diffusion Layer on the Low Carbon Steel

Sutrisno*

Department of Physics, State Islamic University Syarif Hidayatullah Jakarta

*sutrisno@uinjkt.ac.id

Submitted : December; Revised : February; Approved : March; Available Online: March 2024

Abastract: In this paper, a computation model was used to analysis the growth kinetic of two boride layers FeB and Fe_2B on the surface of low carbon steel. St41 one of the low carbon steel was used as the basic sample and given the treatment by adding the powder pack boriding in the temperature of 700, 800, and 900^0C for the 8 hours of treatment time. To perform the morphology and dimension of the boride layers used the optical microscope. The calculation model is based on the diffusion equation of Fick's law and is solved under certain assumptions with parabolic growth of iron boride. For this study, a numerical method was created to determine the thickness of the iron boride layer based on process parameters (temperature and time). Using the parabolic growth constant, it is possible to determine the diffusion coefficient for the FeB, Fe_2B phases and the diffusion region. Based on the diffusion coefficient it can be predicted the depth and thickness of borided layer on the surface of St41 low carbon steel. The diffusion coefficient of boron in the FeB phase is $D_{FeB} = 5{,}67x10^{-14}exp(-99{,}72kJ/RT$, while in the Fe2B phase it is $D_{Fe2B} = 1{,}03x10^{-13}exp(-58{,}17kJ/RT)$, and in the diffusion zone it is $D_Z = 1{,}14x10^{-13}exp(-1{,}7kJ/RT)$. This result indicates that the larger the diffusion coefficient, the faster the diffusion process.

Keywords **:** *powder pack boriding, Fick's Law, parabolic growth constant, diffusion coefficient, FeB/Fe_2B layer*.
DOI : 10.15408/fiziya.v6i2.36554

INTRODUCTION

Boronizing is a surface hardening process that thermo chemical lasted. In this process occurs the dynamics change of heat [1], which can produce phase transformation on the basic sample [2]. The phase change can be determined by XRD analysis method [3]. Boronizing can be applied to hard the surface of ferrous and non ferrous metals. To determine the phases in the sample, it was observed using an optical microscope metallographic [4]. In general, the process

of boronizing performed by heating treatment at a temperature between 700 ° C up to 1000^{O}C for 1 to 12 hours at a metal surface that has been cleaned [5]. In the process of boronizing occurs the contact between the metal surface as a sample base with hardener media in the form of paste, solid powder, liquid, and gas [6]. These contacts are intertition diffusion process, namely the inclusion of boron atoms (B) into the sidelines between the atoms of iron (Fe) [7]. Boronizing results obtained in the form of a layer of iron boride (FeB, Fe2B) with hardness between 1500-2000 HV and the depth of the layer can reach 300 μm from the surface of the sample base [6].

Mechanical properties of the iron boride layer can be determined through testing [8] while the growth process of the formation of iron boride layer on the surface of the sample can be computed using the numerical diffusion equation [9]. Research on the growth mechanism of thermo chemical iron borides have been conducted using a sample of 99.9% pure iron with a temperature of 850 ° C for 15 hours but the results still in qualitative form [10]. The next study for AISI 4140 steel as the samples heated at temperatures varying 1123, 1173, 1223K and treatment time 2, 4, 6 and 8 hours. This boronizing done with molten bath technique consisting of 65% borax, 15% boric acid, and 20% ferro-silicon produce boron growth constant of 3.10^{-9} to 2.10^{-8} $cm^{-2}s^{-1}$ [11]. Growth kinetic of Fe_2B layer with various thickness of boron paste on AISI 1045 steel samples have produced the activation energy from 288.62 kJ for FeB layer and 253.402 kJ for the Fe_2B layer [12]. Growth diffusion model based on Fick's second law for a two layers of iron boride FeB and Fe_2B [13] and also on AISI H13 samples with powder pack boriding technique has been reported by researcher [14].

The next developments use computer simulation through the growth phase of iron boride paste boriding process. This model can be developed for application on another iron sample, because the results of simulations match with the experimental data [15]. Study of layer formed diffusion on the iron-based boride Cr has been done. Samples H13 steel and AISI 304 heated at temperatures of 1073 and 1223 for 3, 5, and 7 hours. This boronizing used bath salt slurry technique consisting of borax, boric acid, ferrosilicon and produce the activation energy of 253.35 and 244.37 kJ mol-1 [16]. The method of fuzzy logic, dimensional analysis and artificial neural network has been applied to measure the growth of boride layers on AISI 1045 steel samples with paste boriding technique. This boriding process is performed at a temperature of 1193 - 1273K for 2, 4, 6 hours and produce a feasible method to apply in industry with automation systems [17, 18, 19]. Besides the method of growth computation on boride layers mentioned above, there are other methods that use mass balance equations assuming a linear concentration profile at the boundary between the layers. The method has been applied to samples of AISI 1045 steel, M2, class 30 gray cast iron (ASTM A48), and gray cast iron. Boronizing process was done using paste boriding technique and powder-pack heated at temperatures of 1173, 1223, and 1273K for 2, 4, 6, 8 hours [20,21,22].

RESEARCH METHODS

A computation model to determine the diffusion coefficient derived from a scenario involving a solvent saturated with solute B. The chemical potential B of surrounding conditions are such that they are capable of forming one or more phases on the surface of steel samples St41. At the stage of equilibrium components A and B form FeB phase, Fe_2B and diffusion zones.

The concentration profile exhibits the growth of two or more phases with a linear progression, and it is presumed that the boron concentration remains constant throughout the process of layer growth.. Thermodynamic equilibrium is achieved at all times during the boriding process. Therefore, according the concentration profile for the three phases below (figure 1), it can be used the following computation model [20] :

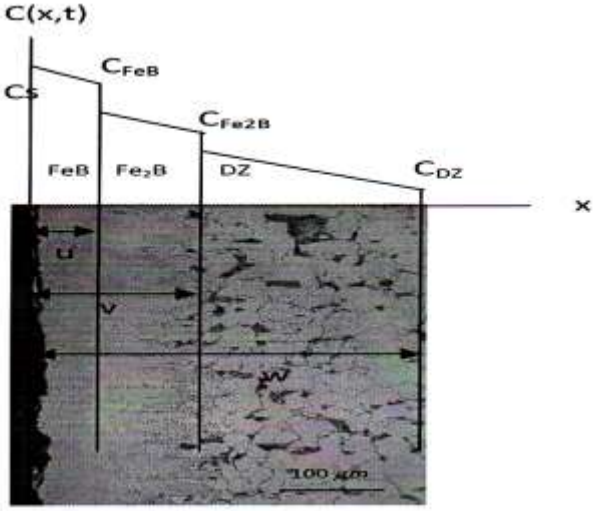

Figure 1. Boron concentration profile for three phases FeB, Fe_2B, and diffusion zone.

for :

$$0 \leq x \leq u \quad ; \qquad C_1(x,t) = \frac{C_{FeB} - C_s}{u} x + C_s \tag{1}$$

$$u \leq x \leq v \quad ; \qquad C_2(x,t) = \frac{C_{Fe_2B} - C_{Fe_B}}{v-u}(x-u) + C_{FeB} \tag{2}$$

$$v \leq x \leq w \quad ; \qquad C_3(x,t) = \frac{C_{DZ} - C_{Fe2B}}{w-v}(x-v) + C_{Fe2B} \tag{3}$$

where : $u = k_1 \sqrt{t}$; $v = k_2 \sqrt{t}$; $w = k_3 \sqrt{t}$ (4)

C(x, t) represents the concentration with respect to both x and t. C_1 (x, t) signifies the boron concentration within the range from the surface to the initial interface, while C_2 (x, t) denotes the boron concentration between the first and second interfaces. C_3 (x, t) represents the boron concentration in the diffusion region, and C_{DZ} stands for the concentration within the diffusion zone. C_{FeB} indicates the concentration at the FeB interface, C_{Fe2B} represents the concentration at the Fe_2B interface, and Cs denotes the concentration above the surface.

Furthermore, the variable t represents the duration of heating, with k1 being the parabolic growth constant for the FeB interface, k2 for the Fe_2B interface, and k3 for the

diffusion region. The parabolic growth functions u, v, and w correspond to the FeB interface, Fe_2B interface, and the diffusion region, respectively. The distance x denotes the distance to the steel surface.

$$(-C_s + C_{FeB})\frac{du}{dt} = D_{FeB}\frac{dC_1}{dx} - D_{Fe2B}\frac{dC_2}{dx} \quad (5)$$

$$(-C_{FeB} + C_{Fe2B})\frac{dv}{dt} = D_{Fe2B}\frac{dC_2}{dx} - D_{DZ}\frac{dC_3}{dx} \quad (6)$$

$$(-C_{DZ} + C_{Fe2B})\frac{dw}{dt} = D_{DZ}\frac{dC_2}{dx} \quad (7)$$

Here, D represents the diffusion coefficient of the solvent on the surface, Do is the pre-exponential factor ($m^2\ sec^{-1}$), D_{Dz} is the boron diffusion coefficient in the diffusion region, D_{FeB} is the diffusion coefficient of boron at the FeB interface, and DFe2B is the diffusion coefficient of boron at the Fe_2B interface. Assuming that the interface conditions adhere to the parabolic growth law and employing a concentration function as described in equations (5), (6), and (7), the following system of simultaneous equations can be derived:

$$\frac{1}{2}(C_{FeB} - C_S)k_1 = D_{FeB}\frac{(C_{FeB}-C_S}{k_1} - D_{Fe2B}\frac{(C_{Fe2B}-C_{FeB})}{k_2-k_1} \quad (8)$$

$$\frac{1}{2}(C_{Fe2B} - C_{FeB})k_2 = D_{Fe2B}\frac{(C_{Fe2B}-C_{FeB})}{k_2-k_1} - D_{DZ}\frac{(C_{DZ}-C_{Fe2B})}{k_3-k_2} \quad (9)$$

$$\frac{1}{2}(C_{DZ} - C_{Fe2B})k_3 = D_{DZ}\frac{(C_{DZ}-C_{Fe2B})}{k_3-k_2} \quad (10)$$

This system of equations can be solved to determine the mobility of boron in the layer FeB, Fe_2B and diffusion zones with Newton-Raphson numerical method (20). Mobility is indicated by the boron diffusion coefficient value for each layer that is D_{FeB} , D_{Fe2B} , and D_{DZ}.

Samples used in this study is cylindrical shape of St41 low carbon steel with a diameter of 3 cm and 1 cm high. The chemical composition of the sample is as shown in table 1.

Table 1. The chemical composition of sample

Element	C	Si	Mn	P	S	N	Cu	Nb	Ti	Al	Cr	Mo	Ni	Vi
Wt%	0.2	0.8-1.4	0.03	0.025	0.015	0.012	0.3	0.02	0.03	0.02	0.3	0.08	0.3	Bal

The specimens were immersed in a boriding agent powder pack comprising 5wt% B_4C, 5wt% KBF4, and 90wt% SiC. Afterwards, the samples were heated in the furnace with temperature of 700^OC, 800^OC, 900^OC and 8 hours treatment time. After heated sample was cooled to room temperature.

Vol.6 No. II 2023, 78-89
P-ISSN: 2621-0215, E-ISSN: 2621-489X

To show the morphology of iron boride, layer thickness, and diffusion zones, the sample was done a cross-sectional cutting and observed using optical microscopy. To determine the layer thickness, minimum 15 measurements were done on boride layers and diffusion zone at different points on the sample. To ensure the phases of iron borides in boride layer on the surface of samples used XRD analysis with Cu and Mo radiation and wave length between 0.6 and l.9 A°.

RESULTS AND DISCUSSION

Morphology and development of the boride layer on St41 low carbon steel with a treatment time of 8 hours and temperature of 700^{O}C, 800^{O}C, and 900^{O}C are shown in figure 2. The thickness of the layer was determined as the mean length of the elongated boride protrusions [20]. On the St41 low carbon steel for all temperature treatment was formed two boride layers FeB and Fe_2B. It can be seen on the pattern of XRD data (see figure 3). The growth change of iron boride is determined by the thickness of the boron powder package. It controls the surface concentration of the specimen and attains the crucial concentration threshold for the development of boride phases [20]. The variation in boron potential energy under constant time and temperature leads to the formation of denser and more uninterrupted layers as the thickness of the boron powder package rises [20].

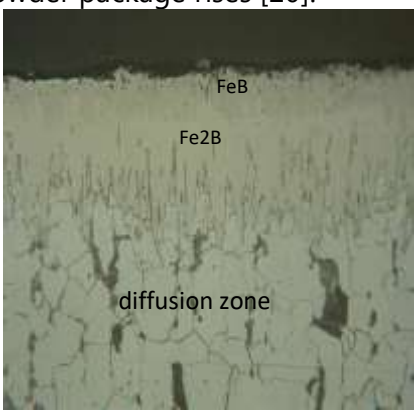

a

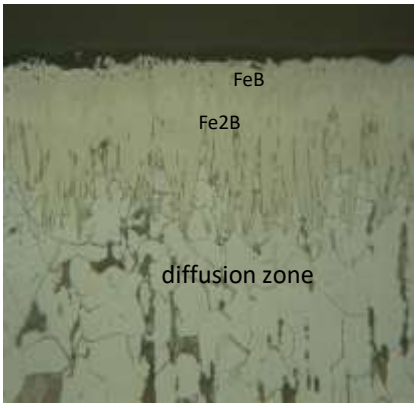

b

Vol.6 No. II 2023, 78-89
P-ISSN: 2621-0215, E-ISSN: 2621-489X

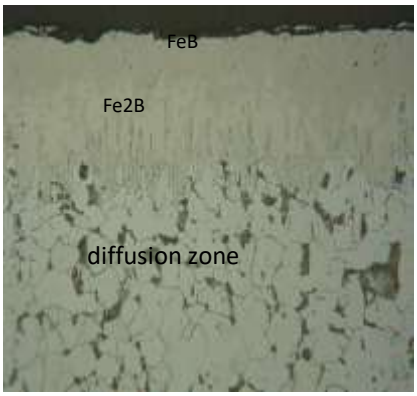

c

Figure 2. View of borided cross-sections (St41 steel) treated at (a)700^{O}C, (b) 800^{O}C, and (c) 900^{O}C for 8 hours with powder pack boriding thickness.

On the same condition, the increment of present phases growth kinetic showed the dependence of time and temperature. Elevating the duration, temperature, and boron potential results in substantial precipitation of Fe_2B iron boride beneath the layers, influenced by the chemical composition of low carbon steel St41. The figure 4 illustrates the progression of boride layers and the diffusion zone concerning the process time. Values of the slopes presented in figure 4 shows the growth of boride layers and diffusion zone. The parabolic growth constants listed in Table 1 are contingent on the equilibrium between boron concentration and the surface of the reference sample.

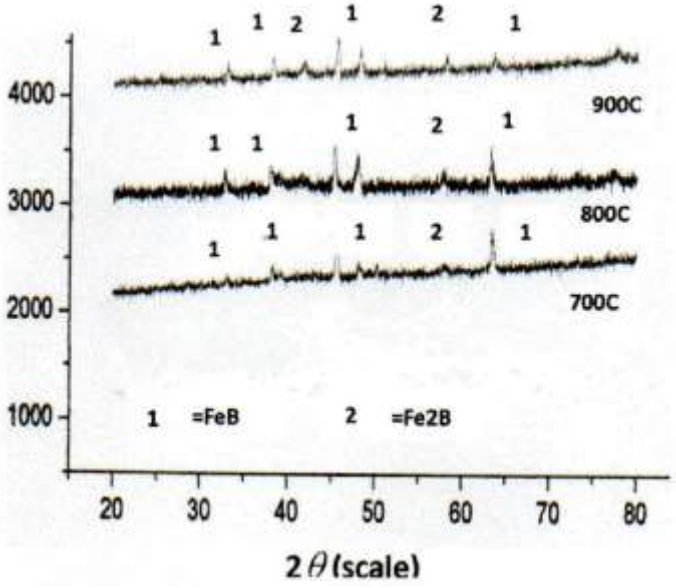

Fig. 3. Pattern of XRD data for St41steel borided at 700, 800, and 900 Celcius with 8 hours of treatment.

Vol.6 No. II 2023, 78-89
P-ISSN: 2621-0215, E-ISSN: 2621-489X

To determine the diffusion coefficients of boron on the boride layers and diffusion zone used the concentration value at interfaces and the parabolic growth constans from mass balance equation (8), (9), and (10).

The parabolic growth constants for St41 low carbon steel exhibit their peak values on the FeB, Fe_2B phases, and diffusion zone at a temperature of 900°C during an 8-hour heat treatment (Table 1).

The average diffusion coefficients are presumed to follow Arrhenius behavior. This pattern assesses these coefficients in relation to temperature, with Q/R denoting the slope depicted in Figure 5. The activation energy, Q, is construed as the boron diffusion along the favored crystallographic direction [0 0 1] [20]. Specifically, the activation energy for the FeB phase surpasses that of the Fe_2B phase, and similarly, the activation energy for Fe_2B exceeds that of the diffusion zone.

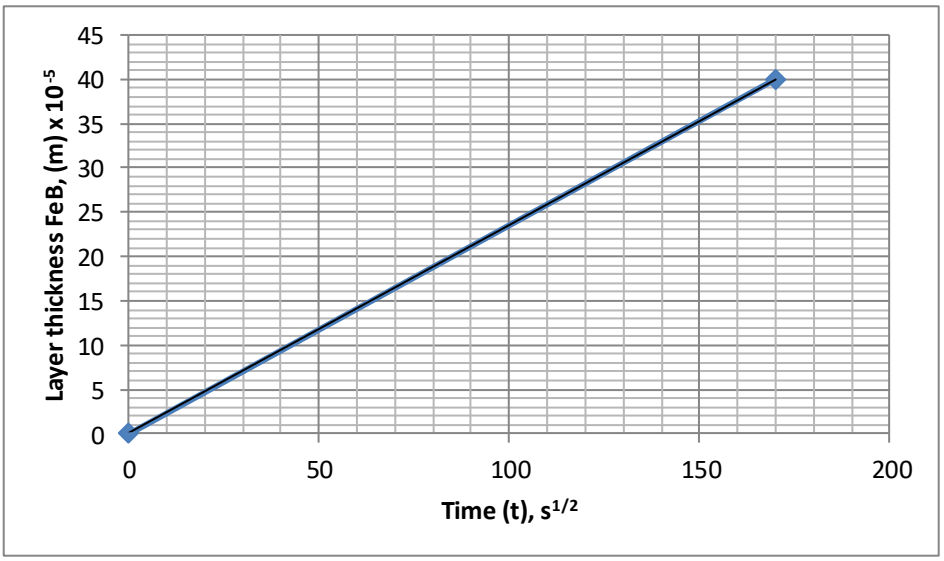

a

Vol.6 No. II 2023, 78-89
P-ISSN: 2621-0215, E-ISSN: 2621-489X

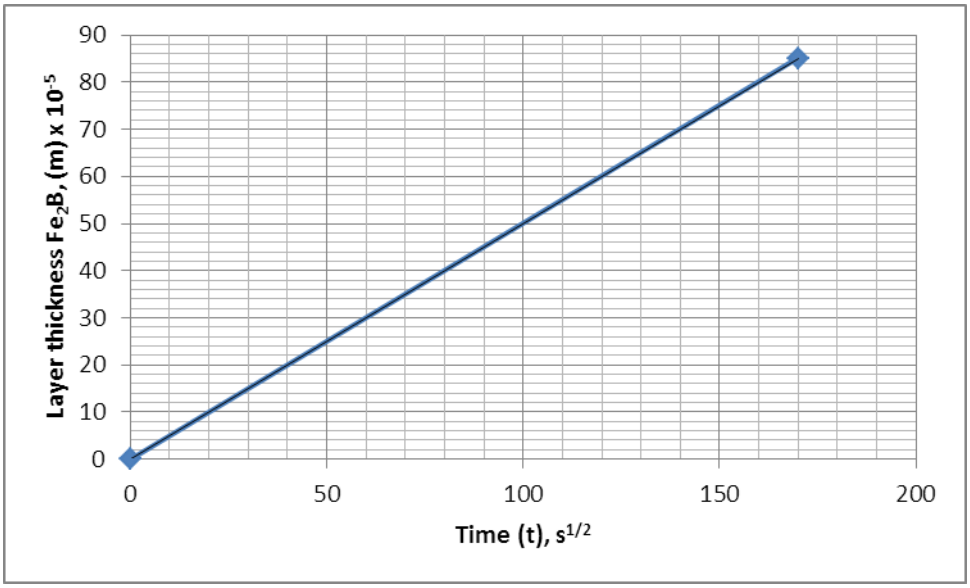

b

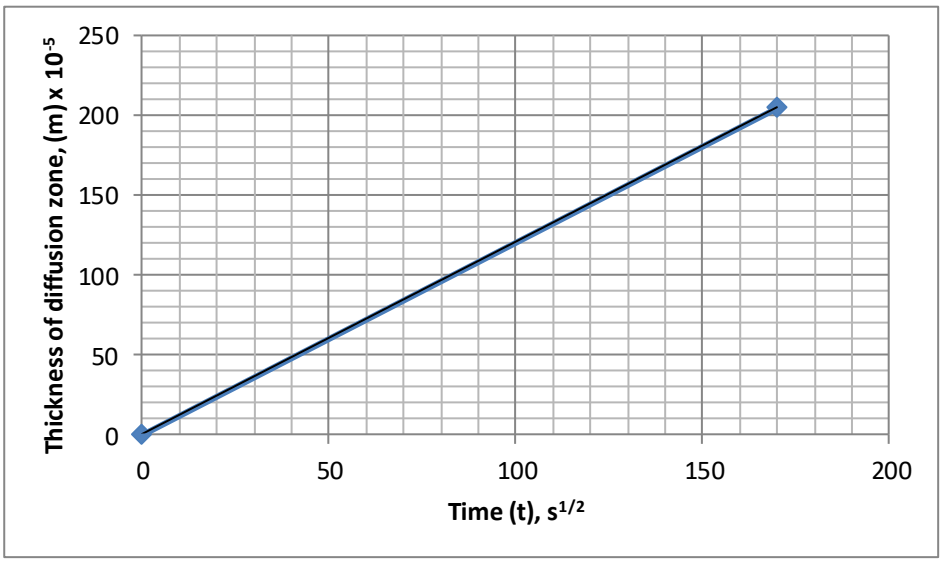

c

Figure 4. Growth kinetics of iron boride layers and diffusion zone for St41 low carbon steel: (a) FeB, (b) Fe_2B and (c) diffusion zone.

Figure 5 illustrates that the activation energy for boron within the FeB layer surpasses that of the Fe_2B layer. Furthermore, the activation energy for boron in the Fe_2B layer exceeds that of the diffusion zone for St41 low carbon steel.

Vol.6 No. II 2023, 78-89
P-ISSN: 2621-0215, E-ISSN: 2621-489X

Table 1. Parabolic growth constants for the St41 low carbon steel at temperature of 700, 800, and 900^{O} C with 8 hours of treatment time.

Layer	Parabolic growth constant (k)		
	T = 700^{0}C	T = 800^{0}C	T = 900^{0}C
Surface	0	0	0
FeB	0.147	0.166	0.220
Fe_2B	0.250	0.282	0.457
Diffusion Zone	0.590	0.610	0.610

Therefore, the Arrhenius relationship gives the diffusion coefficient of boron above FeB, Fe_2B phases, and diffusion zone on the St41 low carbon steel at the temperature range of 700^{O}C $\leq$ T $\leq$ 900^{O}C can be written as:

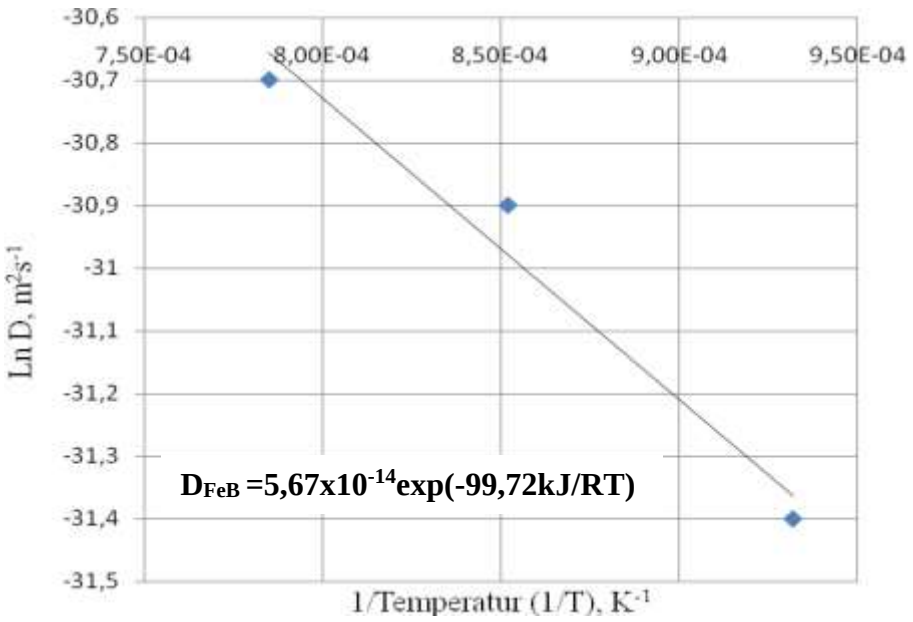

a

Vol.6 No. II 2023, 78-89
P-ISSN: 2621-0215, E-ISSN: 2621-489X

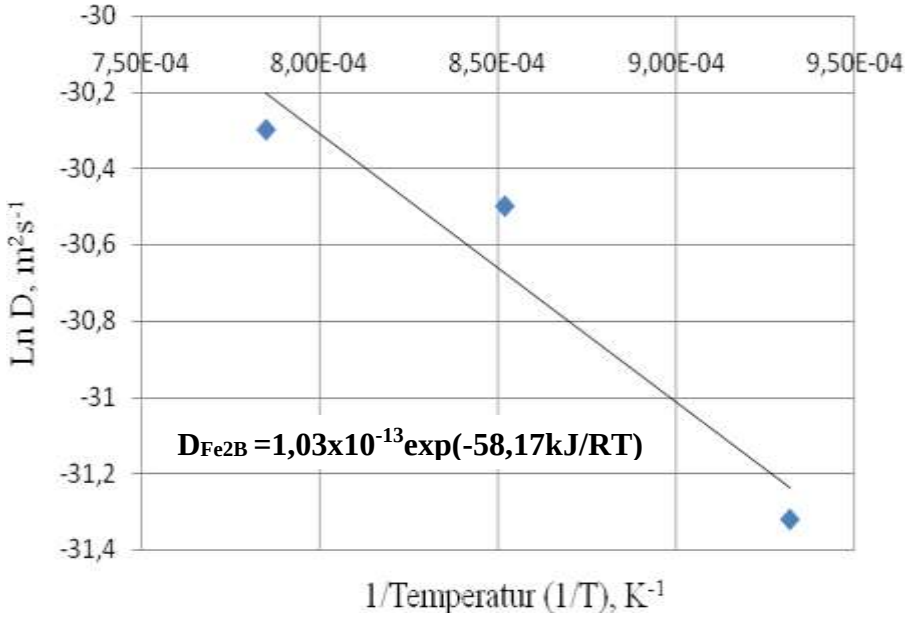

b

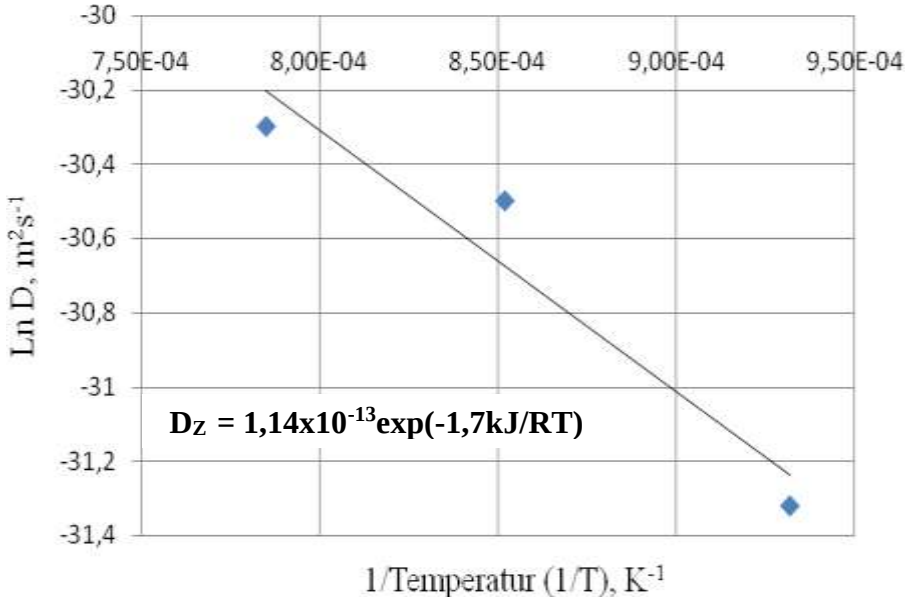

c

Figure 5. Arrhenius relationships for boron diffusion coefficients as a function of treatment temperature on the a).FeB, b).Fe_2B and diffusion zone for St41 low carbon steel.

CONCLUSIONS

In this study the growth kinetics of the boride layers and diffusion zones on St41steels has been analysed. The influence of alloy elements creates the formation of FeB/ Fe_2B on the surface of St41 steel, as shown XRD characterization results. The morphology of the iron boride layers present on the St41 steel is saw-toothed after heating at the temperature of 700, 800, and 900^{O}C. The increase in treatment time and temperature is manifested in the growth kinetics of the iron boride layers and diffusion zones. It results in the formation of denser, uninterrupted layers, and larger precipitates of Fe2B beneath those layers. The activation energy for the iron boride layers and diffusion zones is determined by utilizing the boron diffusion coefficients in the Arrhenius relationship, where temperature plays a crucial role. In the St41 steel, the The activation energy for the FeB phase exceeds that of the Fe_2B phase., and also the activation energy of the Fe_2B phase is greater than diffusion zone. The diffusion coefficient of boron in the FeB phase is $D_{FeB} = 5{,}67x10^{-14}exp(-99{,}72kJ/RT$, while in the Fe_2B phase it is $D_{Fe2B} = 1{,}03x10^{-13}exp(-58{,}17kJ/RT)$, and in the diffusion zone it is $D_Z = 1{,}14x10^{-13}exp(-1{,}7kJ/RT)$. This result indicates that the larger the diffusion coefficient, the faster the diffusion process.

REFERENCES

(References should preferably be managed using Mendeley)

[1] David V. Ragone, Thermodynamic of Materials, John Wiley & Sons, 1995.
[2] DA Porter, KE Easterling, Phase Transformations in Metals and Alloys, Second Edition, Chapman & Hall, London, 1995
[3] C Suryanarayana, M Grant Norton, X-Ray Diffraction A Practical Approach, Plenum Press, New York, London, 1998
[4] George F. Vander Voort, Metallography, Principles and Practice, McGraw-Hill Book Company, K. Genel, Boriding kinetics of H13 steel, Vacuum 80 (2006), 451-457
[5] A.K, Sinha, Boriding (Boronizing) of Steels, ASM Hanbook Vol 4: Heat Treating, USA, ASM International, 1999.
[6] Walter Fichtl, Boronizing and Its Practical Applications, Material in Engineering, Vol.2, 1981
[7] William D Calister Jr, Material Science and Engineering, An Introduction, Fourth Edition, John Willey, 1997, 89 – 101
[8] Ibrahim Ozbek, Cuma Bindal, Mechanical Properties of boronized AISI W4 steel, Surface and Coatings Technology, 154 (2002), 14 – 20
[9] J. Crank, The Mathematics of Diffusion, Clarendon, Oxford, 1975.
[10] C. Martini, G. Palombarini, Mechanism of Thermochemical Growth of Iron Borides on Iron, Journal of Material Science 39 (2004) 933-937
[11] Saduman S, Ugur S, Cuma Bindal, The growth kinetics of borides formed on boronized AISI 4140 steel, Vacuum 77 (2005) 195 – 202
[12] I. Campos, O. Bautista, G. Ramirez, M. Islas, J. De La Parra, L. Zuniga, Effect of boron paste thickness on the growth kinetics of Fe_2B boride layers during the boriding process, Applied Surface Science 243 (2005), 429-436
[13] M. Keddam, SM. Chentouf, A diffusion model for describing the bilayer growth (FeB/Fe_2B) during the iron powder-pack boriding, Applied Surface Science 252 (2005), 393-399
[14] K. Genel, Boriding kinetics of H13 steel, Vacuum 80 (2006), 451-457

[15] M. Keddam, Computer simulation of monolayer growth kinetics of Fe_2B phase during the paste-boriding process: Influence of the paste thickness, Applied Surface Science 253 (2006), 757-761
[16] Sukru T, A study on the diffusion kinetics of borides on boronized Cr-based steels, J Mater Sci (2006) 41: 7590 – 7596
[17] I Campos, M Islas, E Gonzales, P Ponce, G Ramirez, Use of fuzzy logic for modeling the growth of Fe_2B boride layers during boronizing, Surface and Coating Technology 201 (2006) 2717 - 2723
[18] I Campos, R. Torres, G. Ramı´rez a, R. Ganem c, J. Martı´nez, Growth kinetics of iron boride layers: Dimensional analysis, Applied Surface Science 252 (2006) 8662–8667
[19] I Campos, M Islas, G Ramirez, C Villa Velazquez, C Mota, Growth kinetics of borided layers: Artifcial neural network and least square approaches, Applied Surface Science 253 (2007), 6226 – 6231
[20] I Campos, G Ramirez, U Figueroa, J Martinez, O Morales, Evaluation of boron mobility on the phases FeB, Fe_2B and diffusion zone in AISI 1045 and M2 steel, Applied Surface Science, 253 (2007) 3469 – 3475 I Campos, R Torres, G Ramirez, R Ganem, J Martinez,
[21] I Campos – Silva, M Ortiz-Dominguez, M Keddam, N Lopez-Perrusquia, A Garmona-Vargaz, M Elias-Espinosa, Kinetics of formation of Fe_2B layers in gray cast iron: Effects of boron concentration and boride incubation time, Applied Surface Science 255 (2009) 9290 - 9295
[22] M. Keddam, R. Chegroune, A model for studying the kinetics of the formation of Fe2B boride layers at the surface of a gray cast iron, Appl. Surf. Sci. (2010), doi:10.1016/j.apsusc. 2010.03.048

Available online at:
Al-Fiziya: Journal of Materials Science, Geophysics,
Instrumentation and Theoretical Physics
Website: http://journal.uinjkt.ac.id/index.php/al-fiziya
Vol.6 No. II 2023, 92-103

The IoT-Based Mathematical Pendulum Real Laboratory Tool

Agus Sudarmanto[1,*], Joko Budi Poernomo[1], Andika Rifqi Maulana[1]

[1]Departement of Physics, Walisongo State University Semarang, Indonesia

*agussudarmanto@walisongo.ac.id

Submitted : January; Revised : February; Approved : March; Available Online: March 2024

Abstract. Blended learning is a learning approach that combines face-to-face instruction and online learning. In this case, blended learning will be applied to the mathematical pendulum topic through practical experimentation. The mathematical pendulum experiment is a method used to enhance students understanding of the subject matter. This study aims to develop an IoT-based design for a practical mathematical pendulum tool. The research method is based on Research and Development (R&D). The study results in the development of a practical mathematical pendulum tool and control system through the Blynk application. The data displayed on the Blynk application includes the period (t) and the number of oscillations (n). The accuracy of the infrared sensor FC-51 is tested by comparing it with a stopwatch, resulting in a period data accuracy ranging from 96% to 99%. The period data is then used to calculate the acceleration due to gravity (g) with an accuracy ranging from 93% to 97%.

Keywords: *Mathematical Pendulum Experiments, Internet of Things, Blynk*
DOI : 10.15408/fiziya.v6i2.37445

INTRODUCTION

Practical experimentation is a teaching method employed by teachers and instructors to assist students in better comprehending the principles of physics. Generally, practical experiments are conducted in laboratories to provide students and learners with a hands-on experience (Setyaningrum et al., 2013). Typically, practical activities are carried out through a series of steps. Students and learners conduct experiments themselves, accompanied by an instructor or laboratory assistant, in order to personally experience and verify what they have learned or a particular event that has occurred or is occurring. They then observe a process, examine the research object, analyze the data, prove evidence, and draw their own conclusions about the research object, situation, or process related to their subject matter (Kurniawati et al., 2015).

Blended learning is a form of education that combines face-to-face (offline) and online learning methods. It involves integrating traditional in-person instruction with virtual or internet-based learning. Blended learning allows for a flexible and

dynamic approach to education, utilizing the benefits of both physical classroom interaction and digital resources. By merging the advantages of in-person teaching and online platforms, blended learning aims to enhance the learning experience and cater to different learning styles and preferences. (Dinning et al., 2015).

Research on mathematical pendulum instruments conducted using a microcontroller as the data processing unit has been carried out by many parties, including a study conducted by Farasdaq (2020) using Arduino UNO and the Infrared Sensor FC-51 to detect of an object (Farasdaq, 2020). The data accuracy error from Farasdaq's device range from 0,2% to 1,3%. The difference between Farasdaq.s research and other researchers lies in the choice of microcontroller used. The researcher used Nodemcu ESP8266, while Farasdaq used the Arduino UNO. The development of the previous research was done by creating a mathematical pendulum laboratory device that can be accessed and controlled online via a smartphone, which was conducted offline for data collection. Simple harmonic motion is an event where a system exhibits a restoring force that is proportional and opposite in direction to its displacement. This motion is considered simple when it occurs in a sinusoidal manner with a single external force acting upon or impacting the system. As a result, simple harmonic motion occurs as long as the system's displacement is not too large (Giancoli, 2014).

The internet of things can be described as a capability an object for transmitting or transmitting data over the network without using the help of a device computer or human. The Internet of Things (IoT) is a form of recent development in internet technology experiencing very rapid developments in the IT field(Information Technology) From the background above, this research was developed, namely the implementation of a learning approach about pendulums with the internet of things

METHODS

The type of research method used is Research and Development (R&D) with the PPE (Planning, Production, Evaluation) development model which contain of three stages: planning, production, and evaluation (Rustandi et al., 2020). The research, testing, and analysis were conducted from February to June 2023. The research location was in the integrated Laboratory of The Physics Study Program, Faculty of Science and Technology, Walisongo State Islamic University. The following are the stages of conducting the research:

1. Literature Review

The stage of the research is conducted by searching for references related to this study. These references serve as a foundation for the initial groundwork in this research, ensuring that the development. Design, and implementation of the study align with the intended objectives.

Vol.6 No. II 2023, 90-101
P-ISSN: 2621-0215, E-ISSN: 2621-489X

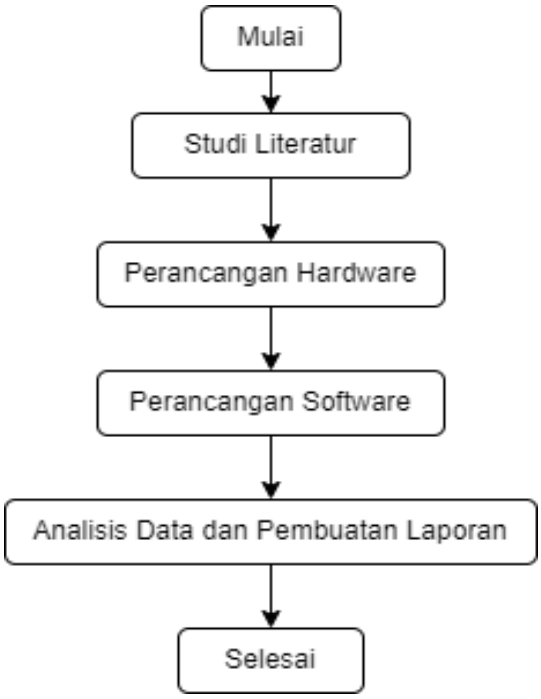

Figure 1 *The Steps of Methods Flowchart*

2. Device Design

At this stage, the hardware design is carried out, which includes the selection of devices and materials, the design of the mathematical pendulum experimental apparatus, the layout of the devices, and the operational flow of the electronic components used, as well as the electric circuitry.

3. Data Analysis and Report Preparation

The final stage involves conducting unit testing on the core components, the infrared sensor, and uploading data from the microcontroller to the application. These tests should be performed as accurately as possible since they will impact the accuracy and success of the mathematical pendulum design. After obtaining the test results, the data is processed, and conclusions are drawn based on the findings. A report summarizing the research findings is then prepared.

Application Design

Blynk is an Internet of Things service provider application that can be downloaded on Android and iOS devices. The usage of the application is relatively easy for beginners. After downloading and installing the application on a smartphone, the next step is to register a Blynk account using an email address. Once registered, the next step is to open a new project and obtain an authentication token that is sent to

Vol.6 No. II 2023, 90-101
P-ISSN: 2621-0215, E-ISSN: 2621-489X

the email used during account registration. The token is used to authenticate the smartphone with the IoT Serang kota server.

Figure 2 *The Blynk Apps Design*

Device Design

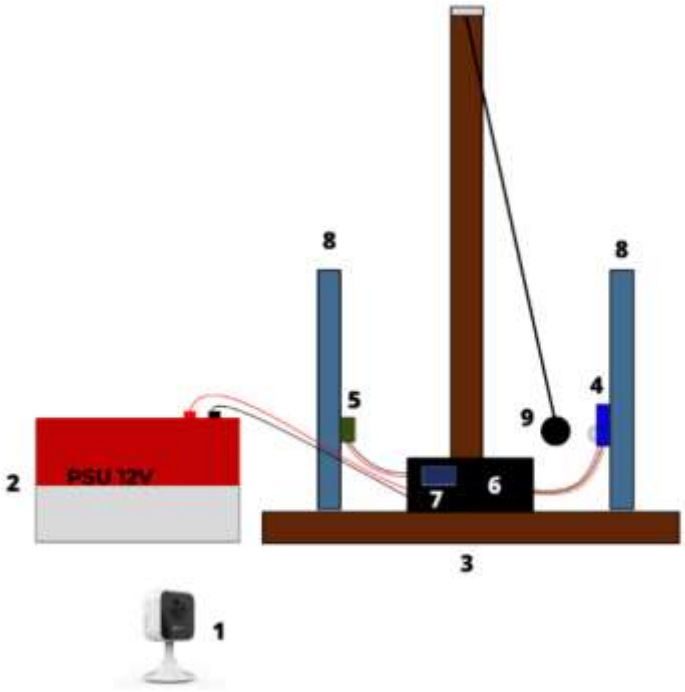

Figure 3 *The Device Design*

The design and construction of the IoT-based mathematical pendulum laboratory device can be seen in Figure 6. The detailed explanation of the tool is describe as follows:

1. The IP Camera is used to monitor the progress of the device through video live streaming.
2. The 12V Power Supply Unit (PSU) serves as the voltage supply the voltage supply for the electromagnet.
3. The static base of the device, made of wood, is used to hold the equipment box and the processing unit device itself. Wood was chosen as the material due to its affordability and ease of modification in terms of shape and dimension for the base.
4. The infrared FC-51 sensor, positioned on the stand, is utilized by the researcher to detect each oscillation of the object with a distance ranging from 1 to 2 cm.
5. Electromagnet to pull the ball object.
6. The box serves as the packaging of the processing unit of the device.
7. The 0.96 inch OLED is used to display the number of oscillations and the period per oscillation.
8. From left to the right, the stand is used to attach the electromagnet and the infrared FC- 51 sensor.

Hardware Design

The design of the IoT-based mathematical pendulum is divided into two parts. The first part is to attract and release the swinging ball made of metal using an electromagnet, and also to detect the pendulum swing using the infrared FC-51 sensor.

The second stage is the operational monitoring of the IoT-based mathematical pendulum device using an IP Camera. The IP Camera used is EZVIZ C1HC, which utilizes the RTSP method to enable the captured images and videos from the camera to be monitored through a media player and the Blynk application.

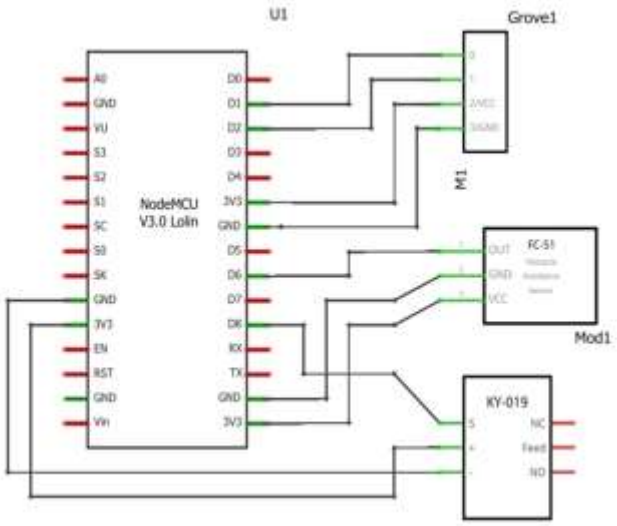

Figure 4 *The Hardware Design*

Vol.6 No. II 2023, 90-101
P-ISSN: 2621-0215, E-ISSN: 2621-489X

Software Design

The software used to program development is Arduino IDE. The choice of this software is because it utilizes the C programming language, which is relatively easy to use for beginners, and because it is open-source software. The data to be obtained in this research are the number of swings (n) data and the period (t) data.

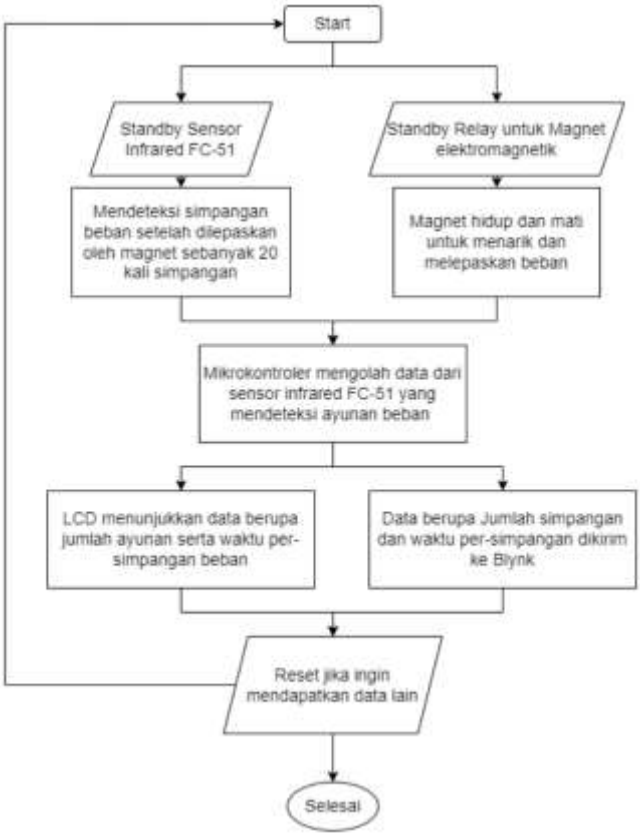

Figure 5 *Flowchart software* mathematic pendulum

Vol.6 No. II 2023, 90-101
P-ISSN: 2621-0215, E-ISSN: 2621-489X

Figure 6 *Flowchart IP Camera*

Device Testing

The obtained data is processed to determined the accuracy level of the device. The accuracy and relative errors of the period data (t) in the IoT-based mathematical pendulum laboratory device can be determined using an equation

$$KR = \frac{\sum \quad t}{\underline{t}} x100\%$$

$$Ketelitian = 100\% - KR$$

The accuracy and errors of the gravitational acceleration (g) fata in this IoT-based mathematical pendulum laboratory device can be determined using an equation

$$KR = \frac{\sum \quad g}{\underline{g}} x100\%$$

$$Ketelitian = 100\% - KR$$

Vol.6 No. II 2023, 90-101
P-ISSN: 2621-0215, E-ISSN: 2621-489X

RESULT AND DISCUSSIONS

The result of unit testing of the device involved measuring the infrared FC-51 sensor, which provided the value of *T*.

Figure 7 Streaming Video Blynk aplication

These sensor measurements resulting the gravitational acceleration values were obtained using a iron ball with a mass of 50 grams and various string length start from 103 cm, 98 cm, 93 cm, 88 cm, and 72 cm.

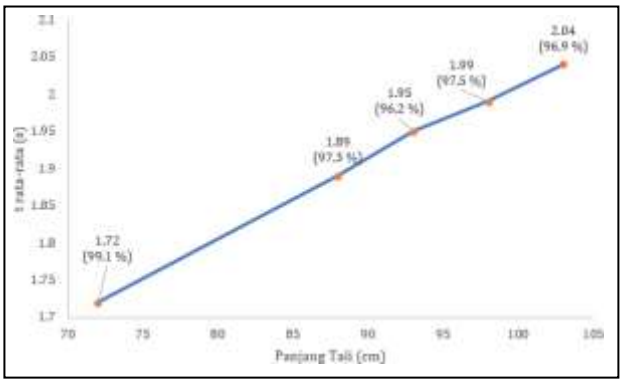

Figure 8 *The Oscillation Period and its Accuracy*

Vol.6 No. II 2023, 90-101
P-ISSN: 2621-0215, E-ISSN: 2621-489X

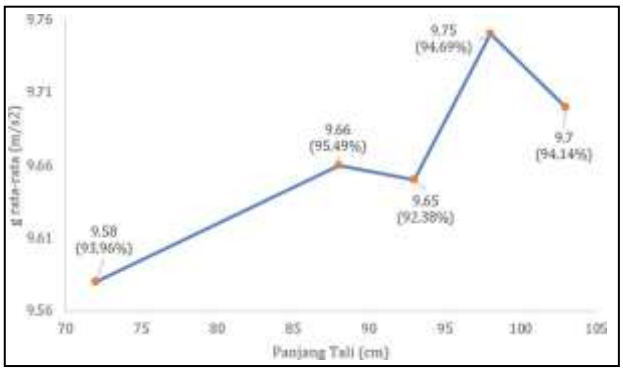

Figure 9 *The Gravity Acceleration and its Accuracy*

According to (Serway & Jewett, 2014), the period and frequency values of a mathematical (simple) pendulum are influenced by the length of the string and gravitational acceleration. The average period values obtained from the given string length and gravitational acceleration are as follows :

$$T = 2\pi\sqrt{\frac{l}{g}}$$

from the equation above, it can be observed that the period of a simple pendulum is directly proportional to the length of the string, indicating that a longer string will result in a longer period of oscillation. On the other hand, the value of gravitational acceleration is nearly constant at approximately 9.78 to 9.8 m/s^2 in most locations on Earth. Consequently, the string length becomes a variable that can be adjusted to obtain different period of oscillation for a simple pendulum.

As shown in the accuracy difference graph in Figure 9, significant variations in the calculated gravitational acceleration can be observed when measuring the oscillation period using five different string lengths. These differences deviate considerably from the universally determined gravitational acceleration value of 9.8 m/s^2. Notably, the variation in string length of 73 cm shows a gravitational acceleration of 9.58 m/s^2, indicating a noticeable from the standard value. The discrepancy is due to the fact that the period of oscillation is not dependent on the mass of the suspended object but rather on length of the string. The period is directly proportional to the string length, resulting in different values of gravitational acceleration (Yanti et al., 2020). For mathematical pendulum experiments (simple pendulum), it is recommended to use a minimum string length of 100 cm, the data results presented above can be used as a standard for mathematical pendulum experiments using string length of 103 cm and 98 cm, as the obtained value of *g* (gravitational acceleration) closely approximates the actual value of gravitational acceleration in the region around the equator, similar to the location where this research was conducted.

CONCLUSIONS

The result on the design and development of the device can be utilized and accessed through an android device using the Blynk apps, which is based on the Internet of Things (IoT). Apps and OLED which includes the number of oscillations (*n*) and the oscillation period (*t*). However, the data for gravitational acceleration (*g*) cannot be displayed in the device in this research due to unstable update rates and limitation in the calculation results, which do not reflect the desire outcomes due to coding difficulties. Based on the data obtained from the device testing, average values of gravitational acceleration were obtained from various string lengths. At a string length of 103 cm, the value of *g* was found to be 9,7 m/s^2 with an accuracy of 94.14%. At a string length of 98 cm, the value of *g* was found to be 9,75 m/s^2 with an accuracy of 94.69%. At a string length of 93 cm, the value of *g* was found to be 9.65 m/s^2 with an accuracy of 92.38%. At a string length of 88 cm, the value of *g* was found to be 9.66 m/s^2 with an accuracy of 95.49%. At a string length of 72 cm, the value of *g* was found to be 9.58 m/s^2 with an accuracy of 93.96%. The accuracy of the calculated *g* values is closely related to the measurement of the oscillation period (*t*) using the infrared FC-51 sensor, with accuracies ranging from 96.2% to 99.1%.

REFERENCES

[1] Abdullah, M. (2016). *Fisika Dasar I*. Institut Teknologi Bandung.

[2] Artiyasa, M., Himawan Kusumah, I., Suryana, A., Edwinanto, Muhammad Sidik, A. D. W., & Pradiftha Junfithrana, A. (2020). Comparative Study of Internet of Things (IoT) Platform for Smart Home Lighting Control Using NodeMCU with Thingspeak and Blynk Web Applications. *FIDELITY : Jurnal T eknik Elektro*, *2*(1), 1–6. https://doi.org/10.52005/fidelity.v2i1.10

[3] Dewi, N. H. L., Rohmah, M., & Zahara, S. (2022). Prototype Smart Home Dengan Nodemcu Esp8266 Berbasis Iot. *Jurnal Ilmiah Teknik*, *1*(2), 101–107. https://doi.org/10.56127/juit.v1i2.169

[4] Dinning, T., Magill, C., Money, J., Walsh, B., & Nixon, S. (2015). Can a Blended Learning Approach Enhance Students' Transition Into Higher Education? a Study To Explore Perceptions, Engagement and Progression. *Research Article International Journal of Advancement in Education and Social Sciences*, *3*(2), 1–7.

[5] Efendi, M. Y., & Chandra, J. E. (2019). Implementasi Internet of Things Pada Sistem Kendali Lampu Rumah Menggunakan Telegram Messenger Bot Dan Nodemcu Esp 8266. *Global Journal of Computer Science and Technology: A Hardware & Computation*, *19*(1), 16.

[6] Efendi, Y. (2018). Internet Of Things (Iot) Sistem Pengendalian Lampu Menggunakan Raspberry Pi Berbasis Mobile. *Jurnal Ilmiah Ilmu Komputer*, *4*(1), 19–26. https://doi.org/10.35329/jiik.v4i1.48

[7] Farasdaq, M. H. (2020). Pengembangan Alat Peraga Bandul Matematis Berbasis Mikrokontroler Arduino Untuk Melatih Keterampilan Proses Sains Siswa SMA. In *FITK UIN Syarif Hidayatullah Jakarta*.

[8] Giancoli, D. C. (2014). *Fisika: Prinsip dan Aplikasi Edisi ke Tujuh* (Erlangga (ed.)). Pearson Education.

[9] Hendrawan, E. D., Winarno, & Novianti, T. (2020). Rancang Bangun Sistem Penghitungan Benih Ikan Lele Otomatis Berbasis Arduino. *Jurnal Ilmiah Computing Insight*, *2*(2), 27–35.

[10] Khoerun, B., & Udhiarto, A. (2019). Pengaruh Variasi Suhu Laminating, Waktu Ultrasonic Cleaning, Kecepatan Rotasi Spin Coating Terhadap Karakterisasi Organic Light Emitting Diode (Oled). *JTT (Jurnal Teknologi Terapan)*, *5*(2), 72. https://doi.org/10.31884/jtt.v5i2.205

[11] Kurniawati, L., Akbar, R. O., & Ali misri, M. (2015). Pengaruh Penerapan Metode Pembelajaran Praktikum Terhadap Keterampilan Berpikir Kritis Matematika Siswa Kelas Viii Smp N 3 Sumber Kabupaten Cirebon. *Eduma : Mathematics Education Learning and Teaching*, *4*(2), 62–74. https://doi.org/10.24235/eduma.v4i2.30

[12] Kusumaningrum, A., Pujiastuti, A., & Zeny, M. (2017). Pemanfaatan Internet of Things Pada Kendali Lampu. *Compiler*, *6*(1), 53–59. https://doi.org/10.28989/compiler.v6i1.201

[13] Lawa, Z., & Najoan, M. (2012). Perancangan Teknologi IP Camera di Jaringan Radio Wirelless PT. PLN Wilayah Suluttenggo. *Jurnal Teknik Elektro Dan Komputer Unsrat*, *1*(3), 1–7. http://ejournal.unsrat.ac.id/index.php/elekdan kom/article/download/608/480

[14] Novelan, M. S., Syahputra, Z., & Putra, P. H. (2020). Sistem Kendali Lampu Menggunakan NodeMCU dan Mysql Berbasis IOT (Internet Of Things). *Jurnal Nasional Informatika Dan Teknologi Jaringan*, *5*(1), 117–121. https://doi.org/10.30743/infotekjar.v5i1.2976

[15] Pambudhi, A., Imansyah, F., & Trias Pontia W, F. (2017). Monitoring Dan Analisis IP Camera Pada Jaringan Internet. *Jurnal Teknik Elektro Fakultas Teknik Universitas Tanjungpura*.

[16] Al Ghifari, F., Anjalni, A., Lestari, D., & Al Faruq, U. (2022). Perancangan Dan Pengujian Sensor LDR Untuk Kendali Lampu Rumah. *Jurnal Kumparan Fisika*, *5*(2), 85-90.

[17] Rustandi, A., Asyril, & Hikma, N. (2020). Pengembangan Media Pembelajaran Berbasis Android pada Mata Pelajaran Simulasi dan Komunikasi Digital Kelas X Sekolah Menengah Kejuruan Teknologi Informasi Airlangga Tahun Ajaran 2020/2021. *Jurnal Binawakya*, *15*(2), 4085–4092. http://ejurnal.binawakya.or.id/index.php/MBI

[18] Satriadi, A., Wahyudi, & Christiyono, Y. (2019). Perangcangan Home Automation Berbasis NodeMcu. *Transient*, *8*(1), 2685–0206. https://ejournal3.undip.ac.id/index.php/transie nt

[19] Serway, R. A., & Jewett, J. W. (2014). *Serway & Jewett - Physics for Scientists and Engineers with Modern Physics 9ed*. https://drive.google.com/file/d/0B3tL3esqtqc bLVNWUFBLTnp4bTg/view

[20] Setyaningrum, R., Sriyono, & Ashari. (2013). Efektivitas Pelaksanaan Praktikum Fisika Siswa Sma Negeri Kabupaten Purworejo. *Radiasi Jurnal Berkala Pendidikan Fisika*, *3*(1), 83–86.

[21] Sulaiman, O. K., & Widarma, A. (2017). *Sistem Internet of Things (Iot) Berbasis Cloud Computing Dalam Campus Area Network*. https://doi.org/10.31227/osf.io/b6m79

[22] Walker, J., Robert, R., & David, H. (2011). *Fundamentals Of Physics 9th Edition*. Wiley.

[23] Yanti, Y., Mulyaningsih, N. N., & Saraswati, D. L. (2020). Pengaruh Panjang Tali, Massa dan Diameter Bandul Terhadap Periode dengan Variasi Sudut. *STRING (Satuan Tulisan Riset Dan Inovasi Teknologi)*, *5*(1), 6. https://doi.org/10.30998/string.v5i1.5885


9 772621 489007


9 772621 021009